Whistler Propagation and Instability Characteristics

by

Joseph C. Lee

SUIPR Report No. 312

May 1969

Prepared under
NASA Grant NGR 05-020-176

INSTITUTE FOR PLASMA RESEARCH
STANFORD UNIVERSITY, STANFORD, CALIFORNIA

WHISTLER PROPAGATION AND INSTABILITY CHARACTERISTICS

by

Joseph C. Lee

NASA Grant NGR 05-020-176

SU-IPR Report No. 312

May 1969

Institute for Plasma Research
Stanford University
Stanford, California

WHISTLER PROPAGATION AND INSTABILITY CHARACTERISTICS

by

Joseph C. Lee

Institute for Plasma Research
Stanford University
Stanford, California

ABSTRACT

This work is a theoretical and experimental study of electromagnetic wave propagation in a homogeneous magnetoplasma. The mode of interest is right-hand polarized, propagating parallel to the magnetic field, and is known in ionospheric terminology as the whistler mode. The theory of its propagation is based on self-consistent solution of the Boltzmann equation with Maxwell's equations. By considering a series of electron velocity distributions, a comprehensive description of whistler propagation, damping and instability characteristics has been obtained.

For isotropic distributions, it is shown theoretically that whistlers propagating parallel to the magnetic field are always stable, and can only suffer cyclotron (collisionless) damping. Both collisional and collisionless damping have been analyzed and computed. Previous calculations of whistler damping are discussed.

Whistler interaction with a gyrating electron beam in a cold plasma is considered first, and is shown to be nonconvectively unstable, i.e. perturbations grow with time. The nonconvective instability can be quenched by collisions or nonzero electron temperature in the background plasma, or more effectively by parallel velocity spread in the beam. After doing so, there is still a weak convective instability, i.e. perturbations grow in space. It is shown that the drift motion of the beam mainly changes the interaction frequency through Doppler shift, and that the drift energy is not used effectively in whistler amplification. Furthermore, the drift motion of the beam may interact very strongly with the plasma via electrostatic modes to give rise to the two-stream instability. The instability analysis has consequently been extended to nondrifting plasmas, for which such competing instabilities should not be so severe.

For anisotropic distributions, it is shown that when the temperature transverse to the magnetic field is greater than that along it, electromagnetic instabilities should occur in the whistler mode. The precise temporal and spatial behavior of the instability has been investigated. It is shown that, in general, whistler instability can be convective, or nonconvective, depending on the degree of temperature anisotropy and the kinetic energy of the hot electrons. In particular, an instability boundary dividing convective and nonconvective instabilities has been obtained in special cases.

For whistlers in bounded magnetoplasmas, a paradox has been pointed out by Wieder. His work shows that, below half the cyclotron frequency, wave propagation characteristics do not approach those of plane wave solutions in unbounded magnetoplasma, even when the plasma density is increased so that the wavelength is arbitrarily small compared to the plasma transverse dimensions. The problem has been resolved by considering the double reflection property of magnetoplasmas. By considering plane waves doubly reflected at the plasma boundary, propagation characteristics in bounded plasma have been related to the unbounded case. As a by-product, the limitations for the validity of the quasistatic approximation for body waves in bounded magnetoplasmas have been established.

To confirm the plane wave dispersion relation in a Maxwellian plasma, a whistler propagation experiment has been carried out in a laboratory plasma. Measurements were made by means of movable antennas immersed in the plasma. Whistler spatial interference patternswere obtained allowing both the real and imaginary parts of the whistler dispersion to be measured in a straightforward way. Good agreement was obtained with simplified collisional theory.

CONTENTS

CONTENTS (Cont'd)

ILLUSTRATIONS

ILLUSTRATIONS (Cont'd)

ILLUSTRATIONS (Cont'd)

ILLUSTRATIONS (Cont'd)

SYMBOLS

a	a constant [Eq. (3.12)]; also transverse dimension of a bounded plasma [Eq. (3.53)]
$a_0, a_1 \cdots a_5$	coefficient of Eq. (4.26)
b	a constant [Eq. (3.12)]
c	velocity of light in vacuum
e	electron charge = 1.602×10^{-19} Coulomb
f	distribution function; also complex function [Eq. (2.38), Eq. (4.31)],
g	normalized distribution function [Eq. (2.5)]; also a parameter defined by Eq. (4.32b)
g_r	a parameter defined by Eq. (B.3)
h	a parameter defined by Eq. (4.32c)
h_r	a parameter defined by Eq. (B.3)
i	$\sqrt{-1}$
k	wavenumber
k_m	marginally stable wavenumber
$\underset{\sim}{k}$	wave vector
$\bar{k}$	saddle point in the k-plane
$k_\pm$	wavenumber defined by Eq. (4.18)
m	mode number [Eq. (3.53)]
m_0	electron rest mass
n	electron number density
n_0	unperturbed electron number density
p	pressure at 0°C (Chapter III)
$\underset{\sim}{p}$	momentum vector (Chapter II)
q	$\mu(\theta) \sin \theta$ [Eq. (3.43)]

s	discontinuity factor [Eq. (3.43)]
t	time variable; also dummy variable [Eq. (3.23)]
v	electron velocity
v_g	group velocity
v_p	phase velocity
v_r	velocity spread for the resonance distribution
v_t	electron thermal speed
x	displacement along x-axis
$\underset{\sim}{x}$	space coordinate vector
y	displacement along y-axis
z	displacement along z-axis

A	voltage amplitude
$\underset{\sim}{A}$	vector potential
A_p	probe area
A_r	parameter defined by Eq. (B.3)
B	voltage amplitude
$\underset{\sim}{B}$	magnetic field vector
$\underset{\sim}{B}_0$	static magnetic field
$\underset{\sim}{B}_1$	first order magnetic field
B_{min}	magnetic field in the midplane of a magnetic mirror
B_{max}	magnetic field at the mirror point
C	Laplace integration contour
$D(\omega,k)$	dispersion function
D_r	dispersion function for right hand polarized waves
D_+	positive frequency part of dispersion function

D_-	negative frequency part of dispersion function
$\underset{\sim}{E}$	electric field vector
$\underset{\sim}{E}_1$	first order electric field vector
E_R	right-hand polarized electric field
E_L	left-hand polarized electric field
$\underset{\sim}{F}$	Lorentz force (Chapter II); also general field vector (Chapter III)
G	detector gain factor
H(x)	Heaviside unit step function
I	probe current
Im	imaginary part of a complex quantity
J	current density
J_R	right-hand polarized current density
J_p	plasma current density
J_{ext}	externally applied current density
K	kc/ω_c normalized wave number
N	a normalization factor $\alpha/(\alpha + \gamma^2)$ [Eq. (4.40)]
N_i	number density of ions
N_m	number density of neutral molecules
P	notation for Cauchy's principal value
P_{en}	probability of electron-neutral collision for momentum transfer
Q	$\alpha_r - 1$
Q_{ei}	effective cross section of ions
Q_{en}	effective cross section of neutral molecules

R	polarization ratio (Chapter JV); also mirror ratio (Chapter IV)
Re	real part of a complex quantity
S	$\mu(\theta) \cos\theta$ [Eq. (3.43)]
$S\left(\frac{\omega_p}{\omega_e}, \frac{\omega_b}{\omega_c}, \frac{T_\perp}{T_\parallel}, \frac{V_{t\parallel}}{c}\right)$	instability boundary [Eq. (4.35)]
T	electron temperature in °K
T_E	transmission coefficient of E wave
T_H	transmission coefficient of H wave
V_e	electron temperature in volts
V_p	voltage of probe signal
V_r	voltage of reference signal
V_{det}	detected voltage
W	cyclotron resonance velocity $(\omega - \omega_c - i\nu)/k$
$Z(\xi)$	Hilbert transform of the Gaussian defined by Eq. (2.23)
$Z_F(\xi)$	complex function of ξ defined by Eq. (3.24)
$Z_r(\xi_r)$	$1/(i - \xi_r)$ [Eq. (B.2)]
$\mathcal{H}$	normalized magnetic field cB
α	temperature anisotropy $\alpha = T_\perp/T_\parallel$; also coefficient of Eq. (3.44)
α_r	resonance distribution anisotropy
β	v_r/c in Eq. (4.26)
δ	phase difference in Eq. (5.1)
$\delta(x)$	Dirac delta function
ϵ	coefficient of Eq. (3.44)

ϵ_0	permittivity of free space = 8.854×10^{-12} f/m
γ	relativistic factor (Chapter II); also $(R-1)^{-1}$ in Eq. (4.38); coefficient of Eq. (3.44)
τ	proper time (Chapter II), also time in the plasma afterglow (Chapter V)
Ψ	scalar potential [Eq. (3.51)]
$\Psi(v_{\parallel})$	real function of $v_{\parallel}$ defined by Eq. (3.37)
$\Psi(1,1,x)$	the plasma wave function [72]
ν	effective electron collision frequency $\nu = \nu_{en} + \nu_{ei}$
ν_{en}	electron-neutral collision frequency
ν_{ei}	electron-ion collision frequency
μ	refractive index of plasma
μ_d	refractive index of an isotropic dielectric
λ	wavelength
λ_0	wavelength in free space
ξ	$(\omega - \omega_c - i\nu - kv_{0\parallel})/kv_t$ [Eq. (4.26)]
ξ_r	$(\omega - \omega_c)/kv_r$ [Eq. (B.2)]
κ	Boltzmann's constant = 1.38×10^{-23} J/°K
π	3.14159
σ	$(\omega_p/\omega_b)^2$
$\Phi(v_{\parallel})$	real function of $v_{\parallel}$ defined by Eq. (2.36)
θ	$\cos^{-1}(\underset{\sim}{k} \cdot \underset{\sim}{B}_0/kB_0)$
θ_R	reflection angle
θ_T	refraction angle
θ_I	incident angle

θ_{res}	resonance cone angle
ω	angular frequency
ω_b	electron plasma frequency of beam or hot electron population
ω_c	electron cyclotron frequency = eB_0/m_0
ω_{ci}	ion cyclotron-frequency
ω_H	hybrid frequency
ω_ℓ	lower cutoff frequency defined by Eq. (3.10)
ω_m	marginally stable frequency
ω_p	electron plasma frequency = $(e^2 n_0/\epsilon_0 m_0)^{1/2}$
ω_u	upper cutoff frequency defined by Eq. (3.10)
ω_+	frequency defined by Eq. (4.19)
$\bar{\omega}$	branch point in the ω-plane
Γ_1	primary reflection coefficient
Γ_2	secondary reflection coefficient
$\Gamma(x)$	Γ function
Λ	9 × (number of electrons in a Debye sphere)
Ω	ω/ω_c
Ω_b	ω_b/ω_c
ϕ	cylindrical coordinate of momentum vector, $p = (p_\perp, \phi, p_\parallel)$

Subscripts

x	x-direction component
y	y-direction component
z	z-direction component

r	real part of
i	imaginary part of
R	right hand polarized
L	left hand polarized
$\parallel$	component parallel to the external magnetic field
$\perp$	component perpendicular to the external magnetic field
0	zero order quantity
1	first order quantity
+	positive frequency part
-	negative frequency part

ACKNOWLEDGMENT

I wish to express my appreciation to my thesis supervisor, Professor F. W. Crawford, for his advice and encouragement during this research. Thanks are also due to Professors R. A. Helliwell and O. G. Villard, Jr., for reading and commenting on the manuscript.

Dr. H. Derfler deserves special thanks for his valuable criticisms and suggestions for Chapter IV. Thanks are also due to Dr. T. J. Fessenden for his part in setting up the apparatus, and to the staff of the Stanford Electronics Laboratories for their cooperation and assistance.

I. INTRODUCTION

One of the most interesting properties of matter in the plasma state is its ability to support propagation of a very wide variety of waves. These may be divided broadly into two classes according to the strength of the RF magnetic field component, $\underset{\sim}{H}$. The first of these is that of longitudinal waves ($\underset{\sim}{H} \approx 0$), e.g., Landau waves [1,2], cyclotron harmonic waves [3], and surface waves [4]. These have been studied extensively in various plasma models over a long period of time. They will not concern us here. The second important class is transverse waves ($\underset{\sim}{H} \neq 0$), e.g., ordinary waves, extraordinary waves [5], and whistlers [6]. The present work is concentrated on whistler propagation including damping, instability, and boundary effects.

A. Natural Whistlers

The closest natural plasmas to the earth's surface are the ionosphere and the magnetosphere. Whistlers were first detected on earth as a natural phenomenon propagating through the ionosphere. They were observed by Barkhausen [7] in 1919 as radio signals with a descending tone, and were subsoquently identified as transverse electromagnetic waves initiated by lightning strokes and guided by the earth's magnetic field. The plasma in which they travel is dispersive, so that the different frequency components in a wave packet spread out in time. When these signals are recorded and played back, they give the whistling sound which gave rise to their name.

When the propagation direction is along the static magnetic field, whistlers are right-hand circularly polarized, i.e., their field vectors rotate in the same sense as an electron gyrating about the magnetic field lines. The same waves are known as "helicons" [8] in solid state plasmas, where conditions are rather different and collisions play a dominant role.

It is well known that without static magnetic field, electromagnetic waves are cut off below the electron plasma frequency, ω_p. With a non-zero magnetic field, the characteristics of the plasma change drastically from the zero magnetic field case. Physically, the equivalent plasma permittivity changes from isotropic to anisotropic, and mathematically from a scalar to a tensor representation. This change opens a window

for propagation in the whistler mode in over-dense ($\omega < \omega_p$) plasmas, in the frequency range from zero to the electron cyclotron frequency, ω_c. This mode is of interest for a variety of reasons. For example it has been proposed to use the whistler mode in satellite antenna design to solve the problem of communication blackout during re-entry of space ships to the earth's atmosphere. Whistler waves have already been widely used as a diagnostic tool in magnetospheric studies [9,10]. Many laboratory plasmas, such as fusion study machines and MHD generators, have ambient magnetic fields. In principle, such plasmas can be diagnosed with relatively low microwave frequencies if the whistler mode is used. In particular, the very low propagation velocities for whistlers that are typically encountered allow conditions for the validity of plane wave theory to be approached in the laboratory. This greatly simplifies the analysis on which the diagnostic techniques are based.

B. Background of Whistler Research

In 1953, Storey [11] examined low frequency whistler propagation properties. From a theoretical study of the ray paths, and an empirical analysis of the data, Storey discovered that whistler energy should be guided by the earth's magnetic field lines. Using low frequency whistlers ($\omega < \omega_c/4$) from one location, and assuming the path of propagation to be at the latitude of the receiver, Storey estimated the minimum electron density along the propagation path in the magnetosphere.

It can be shown that the frequency of minimum group delay in the whistler mode is about $\omega_c/4$. Thus, whistlers containing higher frequency components should show a rising frequency tone contiguous with the descending tone. Whistlers showing this effect were found by Helliwell, et al. [12] and were called "nose" whistlers. With the aid of nose whistlers, Smith [9] and more recently Carpenter [10] have refined and extended estimates of the electron density in the magnetosphere. Most of the early nose whistlers were measured below 60° geomagnetic latitude, and the observed nose whistlers rarely had frequency components above half the minimum cyclotron frequency along the propagation path. On the basis of these observations, Smith arrived at an explanation of the nose whistler observations, based on trapping of whistler energy in ducts of enhanced

ionization. For the background plasma in the magnetosphere, the electron temperature is believed to be of the order of 1 eV. Consequently, most of the whistler propagation in the magnetosphere is explained in terms of classical magnetoionic theory for plane waves, expressed by the Appleton-Hartree formula [13] for cold plasmas.

The first whistler effects observed in the laboratory were reported by Gallet et al [14], in 1960, and were obtained in the large thermonuclear study machine, "Zeta." In the experiment, probe-like dipole antennas were inserted into the middle of the discharge. The maximum plasma frequency was 100 GHz. With cyclotron frequency varying from 3 to 40 GHz, a good approximation to infinite plane wave propagation was obtained. With the antennas separated by about 20 cm, a transmitted signal was observed when the cyclotron frequency was raised above the signal frequency. Since then, several whistler experiments in the laboratory have been reported [15-21]. Most of the results obtained are of a semi-quantitative nature. All have used fixed antennas, and only integrated whistler effects along the propagation path, including the complicated sheath regions close to boundaries, were observed. Wave interferograms were developed in time as the plasma density varied between pulses.

A few boundary value problems for a homogeneous cold collisionless plasma column in a uniform axial magnetic field have been solved numerically [22-24]. The presence of sharp boundaries drastically changes the wave dispersion for certain ranges of parameters. Wieder [24] found that below $\omega_c/2$, plane wave solutions cannot be approached asymptotically either by increasing the transverse dimension of a plasma column or by reducing the wavelength. Hedvall and Sjogren [25] solved a boundary problem for a plasma slab numerically, and found that collisions can remedy this deficiency.

For cold plasmas, whistler damping is due only to collisions. For a hot plasma, collisionless cyclotron damping has been discussed by a number of authors [26-35]. Cyclotron damping is a mechanism for the absorption of energy from a wave by particles through wave-particle resonance interaction. The absorption of energy from the wave is strong when a large number of particles have streaming velocities such that the Doppler-shifted frequency of the wave as seen by the particle equals the electron cyclotron frequency in both magnitude and sense, i.e., the

resonance condition is given by

$$\omega - kv_{\parallel} = \omega_c \cdot \tag{1.1}$$

Since whistlers propagate below the electron cyclotron frequency, it is necessary for the streaming electron velocity, $v_{\parallel}$, to be in the opposite direction to the wave velocity.

A number of works have appeared in the literature on the linearized theory of waves in a hot magnetoplasma. Shafranov [27] formulated a boundary value problem for the propagation of an electromagnetic wave in a semi-infinite hot magnetoplasma. Drummond [28], Willett [32], and Motz [34] gave some numerical calculations for a Maxwellian distribution. Platzman and Buchsbaum [31], and Liemohn and Scarf [33] have calculated cyclotron damping for a resonance distribution. Guthart [35] worked out the damping for a few anisotropic distributions. For an anisotropic distribution, however, energetic particles interacting with whistler waves at Doppler-shifted resonance frequencies can produce whistler instability.

Such whistler instability is of considerable interest in areas as widely separated as magnetospheric physics, thermonuclear fusion, and microwave amplification. Consequently, there are many descriptions of it to be found in the literature, written from different points of view, and covering numerous charged particle velocity distributions [36-50]. As examples relevant to space plasmas, amplified whistlers were suggested as the source of Jupiter's sporadic decameter radiation [38]. Cyclotron resonance interaction between whistlers propagating in the earth's magnetosphere, and energetic gyrating electrons present there, has been used to explain some of the phenomena of VLF emissions [39,44-46].

Anisotropic electron- and ion-velocity distributions occur naturally during the generation, confinement, and heating of plasma. It has been shown theoretically that when the temperature transverse to the magnetic field is greater than that along it, electromagnetic instabilities should occur in the whistler mode [39-42]. Thermal anisotropy due to electron los rough the loss-cone of open-ended magnetic systems has been shown to support a whistler instability [48,49]. With a few exceptions, the previous work on whistler instability is limited to determination of conditions for the onset of instability, or numerical solutions of the

dispersion relations for k real and ω complex, or vice versa. Bers et al [43] studied the precise nature of the whistler instability for the drifting beam case. Further investigations of this type, for beam/plasma interaction in the whistler mode, have been carried out by the author in collaboration with Crawford and Tataronis [50]. In a seemingly different area, Iiyoshi, et al [51] have attributed limitations on RF heating of fusion study plasmas using cyclotron resonance to the presence of a saddle point in the dispersion relation, in the wavenumber plane, at which the frequency is real.

C. Contributions of the Present Work

Theoretical studies forming part of the present work consist of whistler damping and amplification analyses for a number of combinations of velocity distributions. Particular features of the work, lacking from previous studies, are:

1. For an anisotropic velocity distribution, the transition between amplification and attenuation has been examined, and a detailed stability analysis has been made to determine whether the instabilities are such as to give wave growth in space (convective) or in time (nonconvective). Onset conditions for nonconvective instability are established.
2. For whistler propagation in a bounded plasma, the connection between plane waves and bounded waves has been established. The paradox raised by Wieder, for propagation below $\omega_c/2$, i.e., that plane wave solutions are not approached asymptotically by increasing the plasma cross-section, or by reducing the wavelength, is resolved. Limitations on the validity of the quasi-static approximation for waves in bounded magnetoplasma have been established.

The experimental part of this work consists of whistler dispersion and damping measurements in a laboratory plasma. The distinguishing feature of the present experiments is that measurements have been made by means of movable antennas immersed in the plasma. This allows both the real and imaginary parts of the whistler dispersion characteristics

to be measured readily. Measurements have been made at rather low electron temperatures, where cyclotron damping is negligible, and show good agreement with simplified collisional theory.

The plan of the work is as follows. In Chapter II, the general whistler dispersion relation is derived. In Chapter III, we describe whistler propagation, including collisional and collisionless damping. Boundary effects are also calculated and discussed. Chapter IV is devoted to the instability analysis. The dispersion relation is solved for complex frequency in terms of a real propagation wavenumber, and for complex wavenumber in terms of a real frequency. The results are displayed in both graphical and analytical forms for several important velocity distributions. The threshold conditions for instability, and the growth rate of the excited waves are thus obtained. By studying the dispersion relation in the lower half of the complex ω-plane, and the right half of the complex k-plane, the nature of the instability is established. The onset conditions for absolute instability are found for a general anisotropic Maxwellian high energy plasma interacting with a cold background plasma. In Chapter V an experiment on whistler propagation in a laboratory plasma is described. By measuring both the wavelength and damping rate, a set of complex dispersion curves are measured and compared with theoretical calculations. A general discussion of the results is given in Chapter VI.

II. GENERAL ELECTROMAGNETIC WAVE DISPERSION RELATION

A. Wave Characteristics from Dispersion Relation

In studying wave propagation and instabilities in a spatially uniform and time-invariant system, it is usual to perform a linear perturbation analysis of the governing equations. With the assumption of harmonic variations of the form $\exp[i(\omega t - \underset{\sim}{k} \cdot \underset{\sim}{x})]$ for the first order perturbed quantities, a dispersion relation,

$$D(\omega, \underset{\sim}{k}) = 0 \tag{2.1}$$

is obtained. Here D is termed the "dispersion function"; ω is the angular frequency, and $\underset{\sim}{k}$ is the vector wavenumber. In a dispersion relation, mathematically, either ω or $\underset{\sim}{k}$ can be viewed as the independent variable. The phase velocity, $\underset{\sim}{v}_p$, is given by $\omega \underset{\sim}{k}/k^2$, and the group velocity, $\underset{\sim}{v}_g$, is given by $d\omega/d\underset{\sim}{k}$. When the phase velocity of a wave depends on ω or $\underset{\sim}{k}$, the medium is said to be dispersive for that wave. The dispersion in a lossless medium is said to be "normal" when longer waves have larger phase velocities than shorter waves. Dispersion with the reverse character is called "anomalous" dispersion. When $\underset{\sim}{v}_p \cdot \underset{\sim}{v}_g > 0$, the wave is called a "forward" wave; and when $\underset{\sim}{v}_p \cdot \underset{\sim}{v}_g < 0$, the wave is called a "backward" wave. The ratio of the velocity of light in vacuum, c, to v_p is called the refractive index, which is denoted by $\mu (\equiv kc/\omega)$. For $\mu < 1$, the wave is called a fast wave; and for $\mu > 1$, the wave is called a slow wave.

When the medium is lossy, the wave will be attenuated. This is shown by complex solutions for $\underset{\sim}{k}$ for real ω. The imaginary part of $\underset{\sim}{k}$ gives the damping rate. When the medium is active, e.g., systems involving electron beams, energetic particles, or excited atomic states, the wave may grow in space or in time. The growth rate, as well as the nature of the wave growth, can be obtained through study of the dispersion relation. For whistlers, this topic will be treated in Chapter IV.

B. Plasma Model and General Assumptions

Before deriving the whistler dispersion relation, we will first list the conditions under which it will be obtained:

(1) The plasma is assumed stationary in time, uniform in space, and immersed in a constant magnetic field.

(2) The motion of the ions is neglected, due to their relatively large mass.

(3) The electron collision frequency is assumed velocity independent.

(4) There are many particles in a Debye sphere, so that collective plasma effects predominate. There are few particles in a deBroglie sphere, so that quantum effects are negligible.

(5) The steady state particle distribution functions are supposed to be known, and perturbations are assumed small so that linearized theory applies.

(6) The direction of wave propagation is assumed to be parallel to the external magnetic field.

All equations will be in MKS units, unless stated otherwise.

C. Derivation of the Electromagnetic Dispersion Relation

The relativistic equation of motion of a single electron of charge $-e$, and rest mass m_0, in electric and magnetic fields $\underset{\sim}{E}$ and $\underset{\sim}{B}$, is given by

$$\underset{\sim}{F} \equiv \frac{d\underset{\sim}{p}}{dt} = -e(\underset{\sim}{E} + \underset{\sim}{v} \times \underset{\sim}{B}) \quad , \tag{2.2}$$

where $\underset{\sim}{F}$ is the Lorentz force acting on the particle; $\underset{\sim}{p}$ is the relativistic momentum; $\underset{\sim}{v}$ is the particle velocity, and t is the time variable. The relation between $\underset{\sim}{p}$ and $\underset{\sim}{v}$ is given by

$$\underset{\sim}{p} = \gamma m_0 \underset{\sim}{v} \quad , \quad \gamma = \left(1 - \frac{v^2}{c^2}\right)^{-1/2} \quad , \tag{2.3}$$

where γ is the conventional relativistic factor, m_0 the electron rest mass, and c the velocity of light in vacuum. For a group of particles,

the distribution function, $f(\underset{\sim}{x},\underset{\sim}{p},t)$, is given by the relativistic generalization of Boltzmann's equation,

$$\frac{\partial f}{\partial t} + \underset{\sim}{v} \cdot \frac{\partial f}{\partial \underset{\sim}{x}} + \underset{\sim}{F} \cdot \frac{\partial f}{\partial \underset{\sim}{p}} = \frac{1}{\gamma} \frac{df}{d\tau} \quad , \tag{2.4}$$

where $\underset{\sim}{x}$ is the space coordinate vector, and $df/d\tau$ denotes the rate at which collisions change f along a trajectory in phase space, i.e., τ is the proper time. The exact collision integral, df/dt, can be approximated by introduction of a phenomenological relaxation term $df/d\tau = \nu(f_s - f)$, where ν is a velocity independent collision frequency and f_s a stationary state distribution function [52].

Now let $f_s = ng$, where n is the electron density, so that $\int g d\underset{\sim}{p} = 1$ and g depends only on temperatures and drift $\underset{\sim}{p}_d = \int \underset{\sim}{p} g d\underset{\sim}{p}$, i.e., $g = g(T_{\parallel}, T_{\perp}, \underset{\sim}{p}_d)$. When we linearize

$$f_s = n_0 g_0 + n_1 g_0 + n_0 \left(\frac{\partial g}{\partial T_{\parallel}} T_{\parallel 1} + \frac{\partial g}{\partial T_{\perp}} T_{\perp 1} + \frac{\partial g}{\partial \underset{\sim}{p}_d} \cdot \underset{\sim}{p}_{d1} \right) \quad , \tag{2.5}$$

and disregard the energy and momentum balance $(T_{\parallel 1} = T_{\perp 1} = \underset{\sim}{p}_{d1} = 0)$, we have

$$\frac{df}{d\tau} \approx \nu[(n_0 + n_1) f_0 - f] \quad , \tag{2.6}$$

where $f_0 = g_0$ is the normalized stationary state distribution function. For pure transverse waves propagating along the static magnetic field lines, there are no local density fluctuations $(n_1 = 0)$. Hence, Eq. (2.6) reduces to

$$\frac{df}{dt} \approx \nu[n_0 f_0 - f] \quad . \tag{2.7}$$

We further assume there is no zero-order electric field present. Accordingly, we set

$$f = n_0 f_0(\underset{\sim}{p}) + f_1(\underset{\sim}{x},\underset{\sim}{p},t) \ ,$$

$$\underset{\sim}{E} = \underset{\sim}{E}_1(\underset{\sim}{x},t) \quad , \quad \underset{\sim}{B} = \underset{\sim}{B}_0 + \underset{\sim}{B}_1(\underset{\sim}{x},t) \quad , \tag{2.8}$$

where f_1 is the perturbed (first order) distribution function, and $\underset{\sim}{B}_0$, $\underset{\sim}{E}_1$ are the perturbed magnetic and electric fields. Substituting Eq. (2.8) into Eq. (2.4) yields

$$\frac{\partial(n_0 f_0 + f_1)}{\partial t} + \underset{\sim}{v} \cdot \frac{\partial}{\partial \underset{\sim}{x}} (n_0 f_0 + f_1) + \underset{\sim}{F} \cdot \frac{\partial(n_0 f_0 + f_1)}{\partial \underset{\sim}{p}} = \frac{-\nu}{\gamma} f_1 \ . \tag{2.9}$$

For $\underset{\sim}{E} = 0$ and $\underset{\sim}{B} = \underset{\sim}{B}_0$, the zero-order equation is given by

$$\underset{\sim}{v} \times \underset{\sim}{B}_0 \cdot \frac{\partial f_0}{\partial \underset{\sim}{p}} = 0 \ . \tag{2.10}$$

It will be seen that f_0 is a solution of the form $f_0(p_{\|}, p_{\perp}^2)$, where $p_{\|}$ and $p_{\perp}$ are the momentum components parallel and perpendicular to $\underset{\sim}{B}_0$.

With the assumption that the perturbations are small, the first order distribution function is a solution of the linearized Boltzmann equation

$$\frac{\partial f_1}{\partial t} + \underset{\sim}{v} \cdot \frac{\partial f_1}{\partial \underset{\sim}{x}} - e n_0 (\underset{\sim}{E}_1 + \underset{\sim}{v} \times \underset{\sim}{B}_1) \cdot \frac{\partial f_0}{\partial \underset{\sim}{p}} - e \underset{\sim}{v} \times \underset{\sim}{B}_0 \cdot \frac{\partial f_1}{\partial \underset{\sim}{p}} = -\nu f_1 \ . \tag{2.11}$$

In the presence of collisions, the linearization procedure is valid for all electrons (including electrons in synchronism with the RF field) provided

$$\nu > \frac{eE_1}{m_0 \langle v^2 \rangle^{1/2}} \ , \tag{2.12}$$

where $\langle v^2 \rangle$ is the mean squared (thermal) velocity for the distribution [31].

The electromagnetic fields are governed by Maxwell's equations

$$\frac{\partial}{\partial \underset{\sim}{x}} \times \underset{\sim}{E} = - \frac{\partial \underset{\sim}{B}}{\partial t} \quad ,$$

$$\frac{1}{\mu_0} \frac{\partial}{\partial \underset{\sim}{x}} \times \underset{\sim}{B} = \epsilon_0 \frac{\partial \underset{\sim}{E}}{\partial t} + \underset{\sim}{J}_p + \underset{\sim}{J}_{ext} \quad , \tag{2.13}$$

where μ_0 is the free space permeability; ϵ_0 is the free space permittivity; $\underset{\sim}{J}_{ext}$ is an externally applied current density, and $\underset{\sim}{J}_p$ is the plasma current density. It is through $\underset{\sim}{J}_p$ that the electromagnetic fields and the particle distributions are related. We have the relation

$$\underset{\sim}{J}_p = -e \sum \int f \underset{\sim}{v} \, d\underset{\sim}{p} \quad , \tag{2.14}$$

where the summation runs over an arbitrary number of electron distributions, e.g., a background plasma and an energetic group. We have concentrated our interests on electrons. All other charged particle motions can be neglected if the disturbance is of high enough frequency ($\omega \gg \omega_{ci}, \omega_{pi}$). The first-order field quantities are given by

$$\frac{\partial}{\partial \underset{\sim}{x}} \times \underset{\sim}{E}_1 = - \frac{\partial \underset{\sim}{B}_1}{\partial t} \quad , \tag{2.15}$$

$$\frac{1}{\mu_0} \frac{\partial}{\partial \underset{\sim}{x}} \times \underset{\sim}{B}_1 = \epsilon_0 \frac{\partial \underset{\sim}{E}_1}{\partial t} - \sum e \int f_1 \underset{\sim}{v} \, d\underset{\sim}{p} + \underset{\sim}{J}_{ext} . \tag{2.16}$$

Now we choose cylindrical coordinates in momentum space such that

$$p_x \pm i p_y = p_\perp \exp(\pm i \phi) \quad ,$$

$$\phi = \tan^{-1} (p_y / p_x) \quad , \quad p_\perp^2 = p_x^2 + p_y^2 \quad . \tag{2.17}$$

Equation (2.11) then becomes

$$\frac{\partial f_1}{\partial t} + \underset{\sim}{v} \cdot \frac{\partial f_1}{\partial \underset{\sim}{x}} + \frac{\nu}{\gamma} f_1 + \frac{\omega_c}{\gamma} \frac{\partial f_1}{\partial \psi} = en_0(\underset{\sim}{E}_1 + \underset{\sim}{v} \times \underset{\sim}{B}_1) \cdot \frac{\partial f_0}{\partial \underset{\sim}{p}} \quad . \tag{2.18}$$

where ω_c is the cyclotron frequency $(= eB_0/m_0)$. Note that the cyclotron frequency is defined to be positive.

The spatial homogeneity and time invariance of the assumed plasma model permits us to solve Eq. (2.18) by transform techniques. Since all natural phenomena propagate with finite speed, at a given time any signal will be of finite extent, and can therefore be Fourier analyzed in space. In order to include growing, or even strictly periodic phenomena, Laplace transformation in time must be employed. Let the wave vector, $\underset{\sim}{k}$, and the static magnetic field, $\underset{\sim}{B}_0$, be along the positive z-axis. For the first-order distribution function, we then have†

$$f_1[k,\omega] = \int_{-\infty}^{\infty} dz \int_0^{\infty} dt\, f_1(z,t) \exp[-\, i(\omega t - kz)] \quad . \tag{2.19}$$

The inverse transform is given by

$$f_1(z,t) = \int_{-\infty}^{\infty} \frac{dk}{2\pi} \int_C \frac{d\omega}{2\pi} f_1[k,\omega] \exp[i(\omega t - kz)] \quad , \tag{2.20}$$

where k is real, and the contour C is a straight line parallel to the real axis in the lower-half complex ω-plane. It must lie below all singularities of the integrand to conserve causality in the system. Similar transforms apply to other first-order quantities.

Taking the transforms of Eqs. (2.15),(2.16), and (2.18) and assuming no x or y variations for the fields, we have,

$$-ik \times \underset{\sim}{E}_1[\omega,k] = -i\omega \underset{\sim}{B}_1[\omega,k] + \underset{\sim}{B}_1(0^+,k] \quad , \tag{2.21}$$

† Square brackets are used to distinguish spectral functions from functions in the space-time domain.

$$\frac{-1}{\mu_0}\, i\underset{\sim}{k} \times \underset{\sim}{B}_1 = \epsilon_0 i\omega \underset{\sim}{E}_1 - \epsilon_0 \underset{\sim}{E}_1(0^+,k] - \sum e \int f_1 \underset{\sim}{v}\, d\underset{\sim}{p} + \underset{\sim}{J}_{ext}[\omega,k] \,, \quad (2.22)$$

$$i\omega f_1 - i\underset{\sim}{v} \cdot \underset{\sim}{k} f_1 + \frac{\nu}{\gamma} f_1 + \frac{\omega_c}{\gamma} \frac{\partial f_1}{\partial \phi} = en_0 \left\{ \underset{\sim}{E}_1 + \underset{\sim}{v} \times (\underset{\sim}{k} \times \underset{\sim}{E}_1) + i\underset{\sim}{v} \times \underset{\sim}{B}_1(0^+,k] \right\}$$

$$\cdot \frac{\partial f_0}{\partial \underset{\sim}{p}} + f_1(0^+,k] \quad . \quad (2.23)$$

Using the vector triple product identity, and recalling that $\partial f_0 / \partial \phi = 0$ for an initially quiesent plasma $[f_1(0^+,k] = B_1(0^+,k] = 0]$, the right-hand side of Eq. (2.23) gives,

$$en_0 \left\{ E_{1z} \frac{\partial f_0}{\partial p_\parallel} + \left[1 - \frac{kv_\parallel}{\omega} \frac{\partial f_0}{\partial p_\perp} + \frac{kv_\perp}{\partial \omega} \frac{\partial f_0}{\partial p_\parallel} \right] \right.$$

$$\left. \cdot \left[\frac{E_{1x} - iE_{1y}}{2} \exp(i\phi) + \frac{E_{1x} + iE_{1y}}{2} \exp(-i\phi) \right] \right\} \cdot \quad (2.24)$$

We define the right-hand polarized field as $E_R \equiv E_{1x} + iE_{1y}$ and the left-hand polarized field as $E_L = E_{1x} - iE_{1y}$. Equation (2.24) suggests three distinct first-order distribution functions corresponding to the three distinct polarized electric fields, E_z, E_R, and E_L. Equations (2.21) and (2.22) further assure that the fields and the first-order perturbed distributions functions of different polarizations are not coupled together. The whistler mode is contained in the E_R electric field polarization, and the present study is concentrated on this particular polarization. With $E_z = E_L = 0$, the first-order perturbed distribution, f_1, is given by

$$f_1 = \frac{E_R}{2} en_0 \frac{\left(1 - \frac{kv_\parallel}{\omega}\right) \frac{\partial f_0}{\partial p_\perp} + \frac{kv_\perp}{\omega} \frac{\partial f_0}{\partial p_\parallel}}{i\left(\omega - kv - \frac{\omega_c}{\gamma} - i\frac{\nu}{\gamma}\right)} \exp(-i\phi) \,. \quad (2.25)$$

Here, the perturbed distribution due to a circularly polarized wave field exhibits a traveling wave character in geometrical and momentum space. In the latter, it rotates and varies sinusoidally with a period of 2π at a fixed space-time point, and on a $p_{\parallel}$ = constant, $p_{\perp}$ = constant, circle. Note that particles traveling with great speed can see the direction of rotation of the field as reversed. This happens when the sign of $\omega - kv_{\parallel}$ differs from the sign of ω. From Eqs. (2.21) and (2.22), with $\underset{\sim}{B}_1(0^+,k] = \underset{\sim}{E}_1(0^+,k] = 0$, we have

$$(k^2c^2 - \omega^2)\,\underset{\sim}{E}_1 - c^2(\underset{\sim}{k}\cdot\underset{\sim}{E}_1)\,\underset{\sim}{k} = \frac{i\omega}{\epsilon_0}\left\{\sum e\int f_1\underset{\sim}{v}\cdot d\underset{\sim}{p} - \underset{\sim}{J}_{ext}\right\}. \tag{2.26}$$

In order to excite the circularly polarized waves, we apply current sheets, e.g., dense arrays of filamentary conductors perpendicular to each other and to the magnetic field, so that

$$\underset{\sim}{J}_{ext}(t,\underset{\sim}{x}) = \{J_x(t), J_y(t), 0\}\,\delta(z). \tag{2.27}$$

By substituting Eqs. (2.25) and (2.27) into Eq. (2.26), we obtain "Ohm's law"

$$-E_R[\omega,k] = \frac{J_R[\omega,k]}{i\omega\epsilon_0 D_R(\omega,k)}\quad, \tag{2.28}$$

where

$$J_R[\omega,k] = J_x[\omega] + iJ_y[\omega]\quad, \tag{2.29}$$

and $D_R(\omega,k)$ is the right-hand polarized wave dispersion function

$$D_R(\omega,k) = 1 - \left(\frac{kc}{\omega}\right)^2 + \pi\sum\left(\frac{\omega_p}{\omega}\right)^2\int\frac{(\omega\gamma m_0 - kp_{\parallel})\dfrac{\partial f_0}{\partial p_{\perp}} + kp_{\perp}\dfrac{\partial f_0}{\partial p_{\parallel}}}{\gamma(\omega\gamma m_0 - kp_{\parallel} - \omega_c m_0 - i\nu m_0)}\,p_{\perp}^2\,dp_{\perp}\,dp_{\parallel}\,. \tag{2.30}$$

Here $\omega_p(=(e^2n_0/\epsilon_0m_0)^{1/2})$ is the plasma frequency. For $\nu = 0$, Eq. (2.30) reduces to the result given by Zheleznyaskov [53].

For nonrelativistic particles ($\gamma = 1$), it is more convenient to express the distribution function in velocity space rather than in momentum space. This is achieved by replacing f_0 in Eq. (2.29) with $f_0 m^{-3}$, so that now

$$2\pi \int f_0 v_\perp dv_\perp dv_\parallel = 1 \ , \tag{2.31}$$

and

$$D_R(\omega,k) = 1 - \left(\frac{kc}{\omega}\right)^2 + \pi \sum \left(\frac{\omega_p}{\omega}\right)^2 \int \frac{(\omega - kv_\parallel) \dfrac{\partial f_0}{\partial v_\perp} + kv_\perp \dfrac{\partial f_0}{\partial v_\parallel}}{\omega - kv_\parallel - \omega_c - i\nu} v_\perp^2 dv_\perp dv_\parallel \ . \tag{2.32}$$

By partial integration of this equation, one obtains the result

$$D_R(\omega,k) = 1 - \left(\frac{kc}{\omega}\right)^2 + 2\pi \sum \left(\frac{\omega_p}{\omega}\right)^2 \int \frac{(\omega - kv_\parallel) f_0 v_\perp}{\omega - kv_\parallel - \omega_c - i\nu} dv_\perp dv_\parallel$$

$$- \pi \sum \left(\frac{\omega_p}{\omega}\right)^2 \int \frac{(kv_\perp)^2 f_0 v_\perp}{(\omega - kv_\parallel - \omega_c - i\nu)^2} dv_\perp dv_\parallel \tag{2.33}$$

which has been given by Harris [54] for the collision free case ($\nu = 0$).

One could have arrived at the same dispersion function with the ansatz $\exp i(\omega t - kz)$ for the first order quantities, instead of using Fourier and Laplace analysis. However, in this fashion we would have lost the information on how to integrate around the pole at

$$(\omega - \omega_c - i\nu)/k \equiv W \tag{2.34}$$

in Eqs. (2.32) and (2.33). This instruction comes with the rules of Laplace analysis, which require that $D(\omega,k) \neq 0$ for real k and in the lower complex frequency plane, so that the inverse transform integrals of

$E_R[\omega,k]$ (Eq. (2.28)), exist along the contours $k_i = 0^+$ and $\omega_i = \text{const} < 0$, as indicated in Eq. (2.20). To implement this instruction, we rewrite Eq. (2.31) in the form

$$D_R(\omega,k) = 1 - \left(\frac{kc}{\omega}\right)^2 - \sum \left(\frac{\omega_p}{\omega}\right)^2 + \sum \left(\frac{\omega_p}{\omega}\right)^2 \int_{-\infty}^{\infty} \frac{-(\omega_c + i\nu)\ \Phi(v_{||}) + k\psi'(v_{||})}{\omega - kv_{||} - \omega_c - i\nu}\, dv_{||} \tag{2.35}$$

where

$$\Phi(v_{||}) = -\pi \int_0^{\infty} v_\perp^2 \frac{\partial f_0}{\partial v_\perp}\, dv_\perp = 2\pi \int_0^{\infty} v_\perp f_0 dv_\perp \ , \tag{2.36}$$

$$\Psi(v_{||}) = \pi \int_0^{\infty} v_\perp^3 f_0 dv_\perp \ , \qquad \psi' = \frac{d\Psi}{dv_{||}} \ . \tag{2.37}$$

Following Van Kampen [55] and Derfler [56], we use the fact that every square integrable function $f(t)$ has a Fourier transform

$$f[\omega] = \int_{-\infty}^{\infty} f(t)\ \exp -i\omega t\ dt \ . \tag{2.38}$$

so that the inversion integral can be split into "negative frequency" and "positive frequency" parts,

$$f(t) = \frac{1}{2\pi}\int_{-\infty}^{\infty} f[\omega]\ \exp i\omega t\ d\omega = \frac{1}{2\pi}\int_{-\infty}^{0} f[\omega]\ \exp i\omega t\ d\omega + \frac{1}{2\pi}\int_0^{\infty} f[\omega]\ \exp i\omega t\, d\omega$$

$$= f_-(t) + f_+(t) \ , \tag{2.39}$$

which are analytic in the lower and upper t-plane, respectively. This device is now applied to Φ and ψ, so that the dispersion integral, Eq. (2.35) can be performed by residue calculus, with the result

† The real and imaginary parts of a complex quantity, A, are denoted by A_r and A_i.

$$D_R(\omega,k) = 1 - \left(\frac{kc}{\omega}\right)^2 - \sum \left(\frac{\omega_p}{\omega}\right)^2$$

$$+ 2\pi i \sum \left(\frac{\omega_p}{\omega}\right)^2 \left\{\frac{\omega_c + i\nu}{k} \Phi_+(W) - \Psi_+'(W)\right\} \equiv D_{R+}(\omega,k) \quad (W_i > 0) \ ,$$

$$= 1 - \left(\frac{kc}{\omega}\right)^2 - \sum \left(\frac{\omega_p}{\omega}\right)^2$$

$$- 2\pi i \sum \left(\frac{\omega_p}{\omega}\right)^2 \left\{\frac{\omega_c + i\nu}{k} \Phi_-(W) - \Psi_-'(W)\right\} \equiv D_{R-}(\omega,k) \quad (W_i < 0) \ ,$$

(2.40)

where D_{R+} and D_{R-} are called the positive and negative frequency parts of the dispersion function. For real k and frequencies on a Laplace integral path (L.I.P.) ($\omega_i < 0$), we have sign (W_i) = - sign (k), so that D_{R+} applies when $k < 0$, and D_{R-} when $k > 0$.

Following Derfler, the Fourier inversion of Eq. (2.28) can now be performed, either by residue calculus [56] with contributions due to Landau poles ($D_R(\omega,k_n) = 0$) and a continuous spectrum of Van Kampen modes at $W_i = 0$, or by straight integration [57] in terms of the plasma wave function $\Psi(1,1, - ik_n z)$. In either case, we must find the Landau poles at $D_{R+}(\omega,k_n) = 0$ and $D_{R-}(\omega,k_n) = 0$. The job can be reduced considerably due to symmetry relations between the two parts of the dispersion function. Because $\Phi(v_\parallel)$ and $\Psi(v_\parallel)$ are real functions of a real variable, $v_\parallel$, one can prove from the definition Eq. (2.39) that $\Phi_+(W^*) = [\Phi_-(W)]^*$, and similarly for Ψ. When these relations are applied to Eqs. (2.40), one finds that

$$D_{R+}(\omega,k;\nu) = [D_{R-}(\omega^*,k^*; - \nu)]^* \ . \qquad (2.41)$$

We note here that the left-hand polarized wave dispersion function for a hot magnetoplasma, $D_L(\omega,k)$, can be obtained from $D_R(\omega,k)$ simply by replacing ω_c by $-\omega_c$. Then one can prove the following symmetry relations between the two dispersion functions,

$$D_{L\pm}(\omega,k) = \left[D_{R\mp}(-\omega^*,-k^*)\right]^* . \tag{2.42}$$

Due to these symmetry relations,we will restrict ourselves to discussions of the negative frequency part dispersion relation of the right-hand polarized waves, $D_{R-}(\omega,k)$, and remove henceforth the subscript R-.

By setting the dispersion function, $D(\omega,k)$, equal to zero, the dispersion relation is obtained.

$$D(\omega,k) = 0 . \tag{2.43}$$

Whistler propagation, damping, and instability characteristics will be studied through this equation in the following chapters.

III. THE CHARACTERISTICS OF STABLE WHISTLERS

A. Basic Dispersion Relation for Isotropic Distribution Functions

For an isotropic electron velocity distribution, we have $v_\perp (\partial f_0/\partial v_\parallel) = v_\parallel (\partial f_0/\partial v_\perp)$. After a partial integration, the nonrelativistic dispersion relation, $D(\omega,k) = 0$ [Eq. (2.32)], reduces to

$$1 - \frac{k^2c^2}{\omega^2} + \frac{2\pi\omega_p^2}{\omega}\int_{-\infty}^{\infty} dv_\parallel \int_0^{\infty} \frac{f_0 v_\perp dv_\perp}{\omega_c - \omega + kv_\parallel + i\nu} = 0 \quad . \tag{3.1}$$

In terms of Φ, the negative frequency part of the dispersion relation is given by

$$1 - \left(\frac{kc}{\omega}\right)^2 - 2\pi i \frac{\omega_p^2}{\omega k} \Phi_-\left(\frac{\omega - \omega_c - i\nu}{k}\right) = 0 \quad . \tag{3.2}$$

From the general dispersion relation, it can be shown that a plasma with an isotropic velocity distribution cannot support growing electromagnetic waves. A general proof is given in Appendix A. For purposes of illustrating the basic features of the propagation and damping mechanism, we shall begin by discussing a simple resonance distribution

$$f_0(v_\parallel, v_\perp) = \frac{v_r}{\pi^2 (v^2 + v_r^2)^2} \quad . \tag{3.3}$$

This leads to the dispersion relation

$$1 - \frac{k^2c^2}{\omega^2} + \frac{\omega_p^2}{\omega(\omega_c - \omega + i\nu + ikv_r)} = 0 \quad , \tag{3.4}$$

where v_r is a measure of the velocity spread for the resonance distribution. Although this is not a distribution which occurs in nature, it has the advantage of illustrating collisional and collisionless damping

phenomena. From Eq. (3.4), we see clearly that kv_r and ν play the same role for damping. The former represents collisionless cyclotron damping, and the latter collisional damping. The damping becomes important when $(\omega_c - \omega) \lesssim (\nu + kv_r)$. With zero velocity spread, $v_r = 0$, Eq. (3.4) can be written as

$$\frac{k^2c^2}{\omega^2} = 1 + \frac{\omega_p^2}{\omega(\omega_c - \omega + i\nu)} \cdot \tag{3.5}$$

This is the familiar basic dispersion relation for whistlers commonly obtained from the classical Appleton-Hartree formula [13]. Note that in Eq. (3.4), the collision frequency has been assumed as velocity independent.

B. Plane Whistlers in Unbounded Magnetoplasmas

1. Basic Collisionless Whistler Characteristics

When the collision frequency is negligible, Eq. (3.5) reduces to

$$\frac{k^2c^2}{\omega^2} = 1 + \frac{\omega_p^2}{\omega(\omega_c - \omega)} \cdot \tag{3.6}$$

By differentiating this expression with respect to ω, it is easily shown that the maximum phase velocity occurs at $\omega = \omega_c/2$. Under the conditions, $\omega_p \gg \omega_c > \omega$, the term equal to unity in Eq. (3.6) can be neglected. This amounts to neglecting the displacement current term in Maxwell's equations. With this simplification, the group velocity, $v_g (=d\omega/dk)$, is given by

$$v_g = \frac{2c}{\omega_p \omega_c} \omega^{1/2} (\omega_c - \omega)^{3/2} \cdot \tag{3.7}$$

The maximum group velocity occurs at $\omega = \omega_c/4$, and is given by

$$\left(\frac{v_g}{c}\right)_{max} = \frac{3}{8}^{3/2} \left(\frac{\omega_c}{\omega_p}\right) . \tag{3.8}$$

This result provides a simple explanation of the natural nose whistler phenomenon mentioned in Chapter I.

The group velocity can be shown to be greater than the phase velocity for $\omega < \omega_c/2$, and less than the phase velocity for $\omega > \omega_c/2$. At $\omega = \omega_c/2$, we have the maximum phase velocity for whistlers, also $v_g = v_p$. Thus half the cyclotron resonance frequency is a dividing point between normal and anomalous dispersion. The variations of these quantities are depicted in Fig. 3.1.

At low frequencies, $\omega_{ci} \ll \omega \ll \omega_c$, where ω_{ci} is the ion cyclotron frequency, the whistler dispersion relation can be approximated by

$$\frac{k^2c^2}{\omega^2} = \frac{\omega_p^2}{\omega\omega_c} . \tag{3.9}$$

The dispersion curve is then a parabola with vertex at the origin.

By setting $k = 0$, in Eq. (3.6), the three cutoff frequencies are found,

$$\omega_0 = 0, \quad \omega_{u,\ell} = \left[\omega_c \pm \left(\omega_c^2 + 4\omega_p^2\right)^{1/2}\right] \Big/ 2 . \tag{3.10}$$

The complete dispersion curves are shown in Fig. 3.2 The upper branch is the fast right-hand polarized wave. Except close to cutoff, the wave is electromagnetic in nature. The lower branch is the whistler branch. In general, this mode has more energy stored in the RF magnetic field than in the electric field. The remaining energy is carried by the particles. The branch with negative frequency is actually the left-hand polarized fast wave.

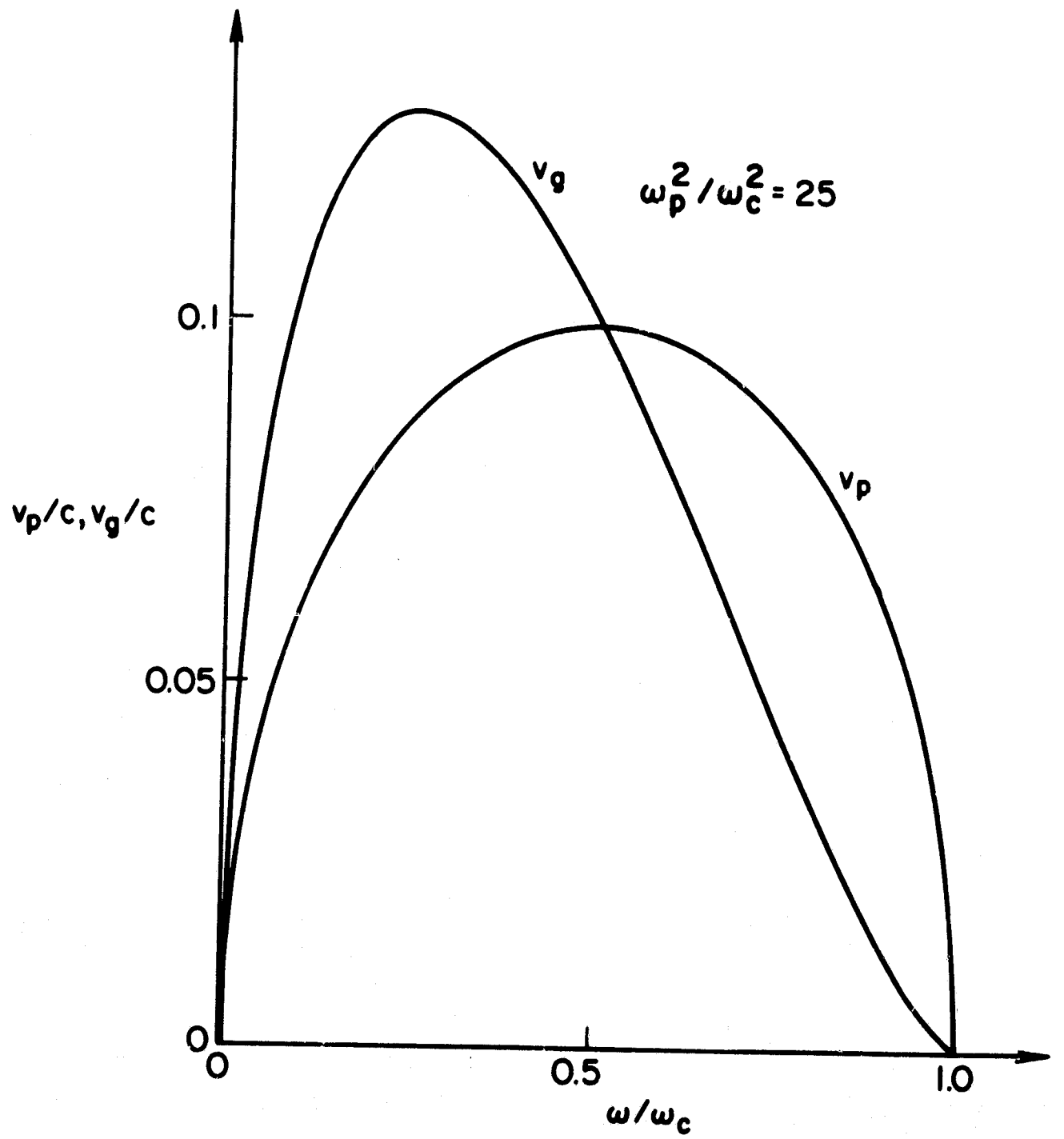

FIG. 3.1. WHISTLER PHASE AND GROUP VELOCITIES.

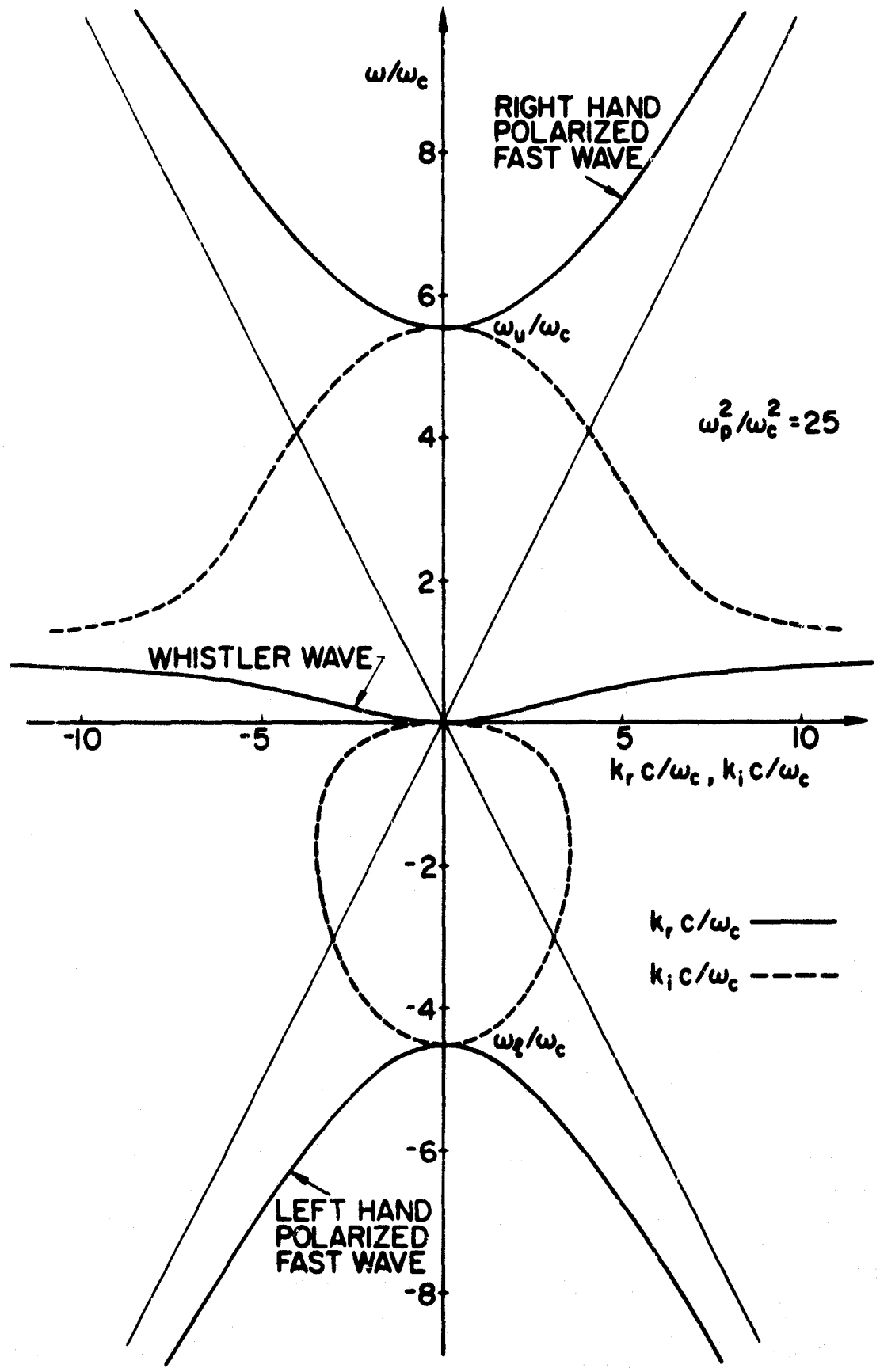

FIG. 3.2. BRILLOUIN DIAGRAM OF TRANSVERSE ELECTROMAGNETIC WAVES IN A COLD COLLISIONLESS MAGNETOPLASMA.

2. Collisional Damping

The behavior at and near the electron cyclotron frequency, ω_c, as determined by the above model, is not strictly correct. This model shows k to be purely real for $\omega < \omega_c$, and approaching infinity as $\omega \rightarrow \omega_c$. This implies an undamped wave whose wavelength approaches zero. For $\omega > \omega_c$, the behavior signifies an evanescent disturbance whose skin depth increases from zero at ω_c to infinity at $\omega = \omega_u$.

In practice, the actual behavior of k in the resonance region will differ greatly from that just described because of collisional and cyclotron damping. For low temperature, Coulomb collision effects will be important at higher densities. For any temperature, electron/neutral collisional effects will become important at high background pressures. For high temperature, collisionless damping will be important. In all these cases, the analysis shows k to be finite and complex in the resonance region, signifying a wave that is damped. We will consider the collisional damping first.

Assume that only elastic collisions of electrons with other constituents of the plasma take place. The probability of electron-neutral collision for momentum transfer, P_{en}, is related to the effective cross-section of the neutral particles, Q_{en}, and to the corresponding electron-neutral collision frequency, ν_{en}, by the equation

$$\nu_{en} = p\, P_{en} v = N_m Q_{en} v \,, \tag{3.11}$$

where N_m is number density of neutral molecules; v is the electron, velocity, p is the pressure (at 0° C). Analogous quantities for electron-ion collisions are

$$\nu_{ei} = N_i Q_{ei} v = \frac{a N_i}{T^{3/2}} \ell n \frac{b T^{\frac{3}{2}}}{N_i^{\frac{1}{2}}} \,, \tag{3.12}$$

where a, b are constants depending on various assumptions made in the derivation. The differences between the published treatments are in general within a factor of two [58-60]. For electron temperatures below about

80 eV, the effective electron-ion Coulomb collision frequency is adequately estimated [60] as

$$\nu_{ei} = 2.9 \times 10^{-6} \frac{n_0 \ell n \Lambda}{V_e^{3/2}} \quad \text{collisions/sec} \quad , \tag{3.13}$$

where n_0 is the plasma number density in electrons per cm^3; V_e $(=KT/e)$ is the electron temperature in volts, and Λ is $9 \times$ (number of electrons in a Debye sphere). The total effective collision frequency is given by

$$\nu = \nu_{en} + \nu_{ei} \quad . \tag{3.14}$$

Since both ν_{en} and ν_{ei} are averaged over the particle velocity variation, ν is considered velocity independent. For $(\omega_c - \omega) \gg \nu$, the real and imaginary parts of k of Eq. (3.5) can be separated by use of Taylor's expansion. We obtain

$$\frac{k_r^2 c^2}{\omega^2} = 1 + \frac{\omega_p^2}{\omega(\omega_c - \omega)} - \frac{\omega_p^2 \nu^2}{\omega(\omega_c - \omega)^3} \quad , \tag{3.15}$$

$$k_i c = \frac{-\omega_p \nu \omega^{\frac{1}{2}}}{2(\omega_c - \omega)^{3/2}} \quad , \tag{3.16}$$

where $k_r \gg k_i$ and $\omega_p^2/\omega_c^2 > 1$ are assumed. At cyclotron resonance, $\omega = \omega_c$, the above analysis is no longer valid. If $\omega_p^2/\omega_c^2 \gg 1$, we can neglect the unity term in Eq. (3.5) and near the cyclotron resonance we have

$$|k_r| = |k_i| = \frac{\omega_p}{(2\omega_c \nu)^{\frac{1}{2}}} \quad . \tag{3.17}$$

The above analysis shows the general behavior of the collisional effects upon whistler dispersion. A set of numerical calculations based on Eq. (3.5) is given in Fig. 3.3.

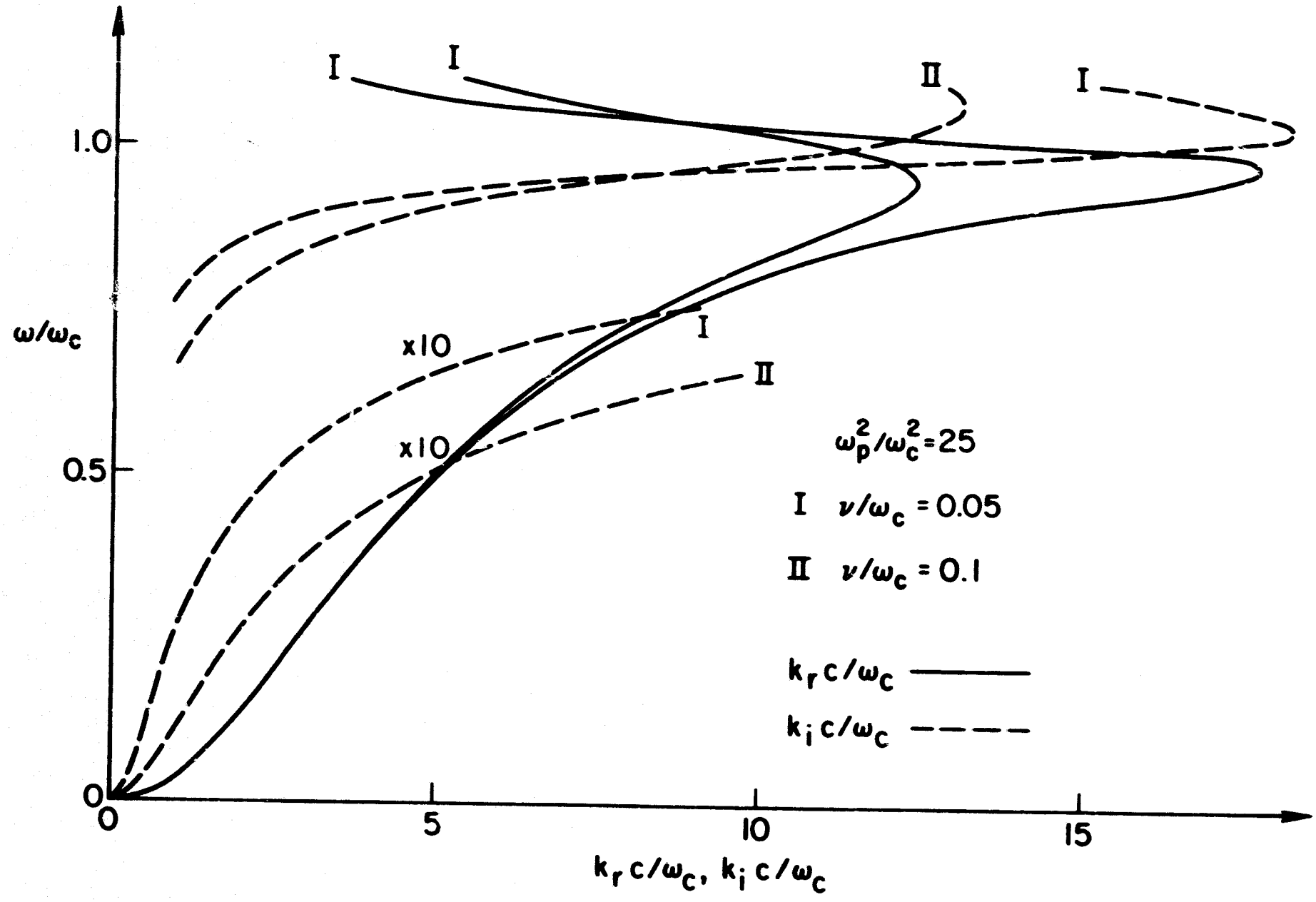

FIG. 3.3. COLLISIONAL EFFECTS ON WHISTLER DISPERSION CHARACTERISTICS IN A COLD MAGNETOPLASMA.

3. Cyclotron Damping

When the mean thermal velocity of the plasma electrons becomes comparable to $(\omega_c - \omega)/k$, a large proportion of the electrons will be in synchronism with the whistler wave. The propagation characteristics are then strongly modified. For the resonance distribution, we have Eq. (3.3) as the whistler dispersion relation. For both v_r and ν small, the influence of collisions and temperature on the dispersion is small, except near resonance frequencies. As a first order approximation, the cold plasma dispersion relation may be used to estimate k,

$$k^2c^2 = \frac{\omega_p^2 \omega}{(\omega_c - \omega)} \quad , \quad \left(\omega_p^2 \gg \omega_c^2\right) . \tag{3.18}$$

Thus we have

$$\frac{kv_r}{\nu} = \left(\frac{\omega_p}{\nu}\right)\left(\frac{\omega}{\omega_c - \omega}\right)^{1/2}\left(\frac{v_r}{c}\right) .$$

The ratio (kv_r/ν) can be used as a crude estimate of the relative importance of the collisionless and collisional damping. The above estimate is not valid near or at resonance, where the presence of temperature and collisions greatly disturb the dispersion. For $\nu = 0$, at resonance the dispersion reduces to

$$\frac{k^2c^2}{\omega_c} \approx \frac{-i\omega_p^2}{\omega_c kv_r} , \tag{3.19}$$

The three solutions to this equation are

$$\frac{k_{1,2}c}{\omega_c} \approx \left(\frac{\pm 3^{1/2}}{2} - \frac{1}{2}\right)\left(\frac{\omega_p^2 c}{\omega_c^2 v_r}\right)^{1/3} \quad , \quad \frac{k_3 c}{\omega_c} \approx i\left(\frac{\omega_p^2 c}{\omega_c^2 v_r}\right)^{1/3} . \tag{3.20}$$

Of the three solutions, only the first is valid for the $+z$ direction. That root is connected to simple cold plasma whistlers. The solution of k_3 corresponds to an evanescent mode propagating in the $-z$ direction. In cold plasmas, this mode exists between ω_u and ω_c. Finite electron temperature makes k_3 finite at cyclotron resonance. Note that k_3 remains purely imaginary if $\nu = 0$. In general, Eq. (3.4) is a cubic equation with complex coefficients for k. It can be readily solved numerically, and a set of solutions is shown in Fig. 3.4.

Although study of the resonance distribution gives valuable insight into the cyclotron damping process, the distribution to be expected most often experimentally is the Maxwellian. This may be written as

$$f_0(v_\parallel, v_\perp) = \frac{1}{v_t^3 \pi^{3/2}} \exp\left[-\frac{v_\parallel^2 + v_\perp^2}{v_t^2}\right], \tag{3.21}$$

where $v_t [= (2KT/m)^{1/2}]$ is the thermal speed, and K is Boltzmann's constant. If we define $t = v_\parallel / v_t$, $\xi = (\omega - \omega_c - i\nu)/kv_t$, and integrate Eq. (3.1) with respect to $v_\perp$, we obtain

$$1 - \frac{k^2 c^2}{\omega^2} + \frac{\omega_p^2}{\omega k v_t} Z(\xi) = 0, \tag{3.22}$$

where $Z(\xi)$ is defined by

$$Z(\xi) = \begin{cases} \dfrac{1}{\pi^{\frac{1}{2}}} \displaystyle\int_{-\infty}^{\infty} \frac{\exp(-t^2)\, dt}{t - \xi} & , \ \xi_i < 0 \\ \dfrac{1}{\pi^{\frac{1}{2}}} P \displaystyle\int_{-\infty}^{\infty} \frac{\exp(-t^2)\, dt}{t - \xi} - i\pi^{\frac{1}{2}} \exp(-\xi^2) & , \ \xi_i = 0 \\ \dfrac{1}{\pi^{\frac{1}{2}}} \displaystyle\int_{-\infty}^{\infty} \frac{\exp(-t^2)\, dt}{t - \xi} - 2i\pi^{\frac{1}{2}} \exp(-\xi^2) & , \ \xi_i > 0 \end{cases} \tag{3.23}$$

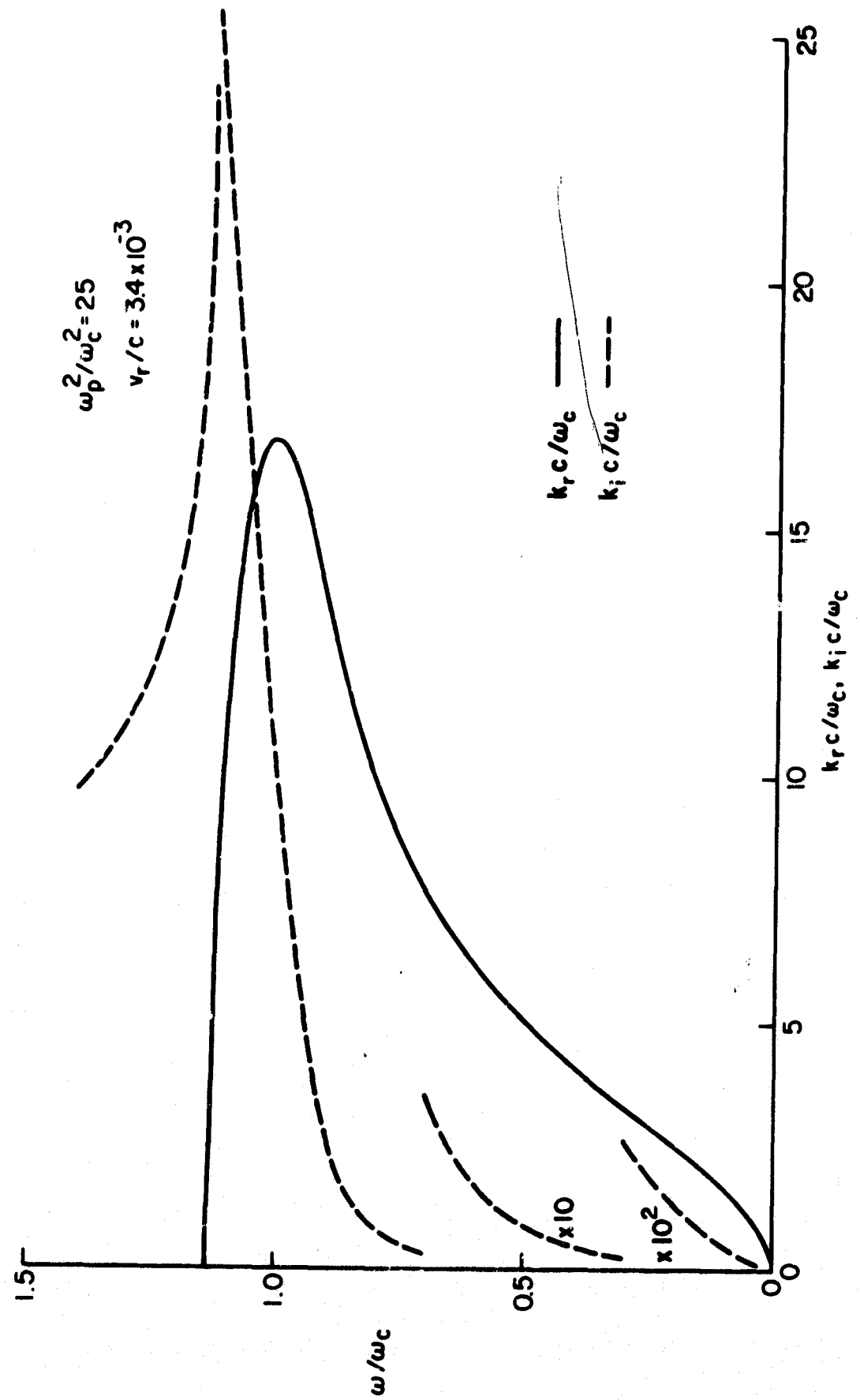

FIG. 3.4. WHISTLER DISPERSION CHARACTERISTICS FOR PLASMA WITH RESONANCE VELOCITY DISTRIBUTION

and is related to the plasma dispersion function tabulated by Fried and Conte [60], Z_F, by

$$Z(\xi) = [Z_F(\xi^*)]^* \quad . \tag{3.24}$$

For $\nu = 0$, we have $\xi = 0$ and at resonance $(\omega = \omega_c)$,

$$Z_F(0) = i\pi^{\frac{1}{2}}, \qquad Z(0) = -i\pi^{\frac{1}{2}} .$$

Hence, Eq. (3.22) reduces to

$$\frac{k^2c^2}{\omega_c^2} \approx \frac{-i\omega_p^2\pi^{\frac{1}{2}}}{\omega_c kv_t} \quad , \quad \left(\omega_p^2 >> \omega_c^2\right) . \tag{3.25}$$

The three solutions for k in Eq. (3.25) are given by

$$\frac{k_{1,2}c}{\omega_c} \approx \left(\frac{\pm 3^{1/2}}{2} - \frac{i}{2}\right)\left(\frac{\pi^{\frac{1}{2}}\omega_p^2 c}{\omega_c^2 v_t}\right)^{1/3} \quad , \quad \frac{k_3 c}{\omega_c} \approx i\left(\frac{\pi^{\frac{1}{2}}\omega_p^2 c}{\omega_c^2 v_t}\right)^{1/3} . \tag{3.26}$$

Comparing with Eq. (3.19), we see that at resonance the Maxwellian distribution and the simple resonance distribution are similar. If we set $v_t = \pi^{\frac{1}{2}} v_r$, the two distributions are indistinguishable for whistler waves at resonance. Off resonance, they are of course different. Just as for the case of a simple resonance distribution, only the first solution, which is connected to simple cold plasma whistlers, is valid for the $+z$ direction.

For frequencies far from cyclotron resonance, the function $Z(\xi)$ can be approximated by its asymptotic series for $|\xi| >> 1$

$$Z(\xi) = -i\pi^{\frac{1}{2}} \exp(-\xi^2) - \frac{1}{\xi}\left(1 + \frac{1}{2\xi^2} + \frac{3}{4\xi^4} + \ldots + \frac{\Gamma(n+\frac{1}{2})}{\pi^{\frac{1}{2}}\xi^n} + \ldots\right) \tag{3.27}$$

where

$$s = \begin{cases} 0 \\ 1 \\ 2 \end{cases} \qquad \xi_i \lesseqgtr 0 \ .$$

Note that the factor s is a consequence of Stokes' phenomenon and does not represent a true discontinuity of the function. Substituting this into Eq. (3.22), gives

$$\frac{k^2c^2}{\omega^2} = -\, i\frac{s\pi^{\frac{1}{2}}\omega_p^2 \exp(-\xi^2)}{\omega k v_t} + 1 + \frac{\omega_p^2}{\omega_c - \omega + i\nu} + \frac{\omega_p^2 k_r^2 v_t^2}{2\omega(\omega_c - \omega + i\nu)^3} \cdot \quad (3.28)$$

When $k_r \gg k_i$, and $\nu = 0$, we have

$$\frac{k_r^2c^2}{\omega^2} \approx 1 + \frac{\omega_p^2}{\omega(\omega_c - \omega)} + \frac{\omega_p^2 k_r^2 v_t^2}{2\omega(\omega_c - \omega)^3}$$

$$\approx \left(1 + \frac{\omega_p^2}{(\omega_c - \omega)}\right) \Bigg/ \left[1 - \frac{\omega_p^2 \omega\left(v_t^2/c^2\right)}{2(\omega_c - \omega)^3}\right] \ , \quad (3.29)$$

or

$$\frac{k_r c}{\omega} \approx \frac{\omega_p}{(\omega_c - \omega)^{\frac{1}{2}}}\left[1 + \frac{\omega_p^2 \omega (v_t^2/c^2)}{4(\omega_c - \omega)^3}\right] \cdot \quad (3.32)$$

The square bracket represents a correction to the cold whistler mode. This approximation breaks down near cyclotron resonance, because there ξ is no longer large. In low-frequency regions, where the approximation is good, the temperature increases k_r above the cold plasma value. This is in contrast to the qualitative dispersion diagram given by Pradhan [26] which shows the opposite temperature effect. A further discrepancy is that Pradhan's diagram shows the real part of the refractive index at resonance equal to unity, independent of plasma density. Equation (3.29)

demonstrates this conclusion to be incorrect. By comparing Eq. (3.15) with Eq. (3.30) we see that the first order effects of collisions and temperature upon k_r are in opposite directions. Indeed, within the range of validity of the asymtotic expansion, they will cancel when $\nu = kv_t/2$. It should be emphasized that the compensating effect of collisions and temperature applies only to k_r. The attenuations are not cancelled, but should be added. For the imaginary part of k, when $k_r \gg k_i$ we have

$$k_i c \approx - \frac{\pi^{\frac{1}{2}} (\omega_c - \omega)\, c}{2v_t} \exp(-\xi^2) . \qquad (3.31)$$

Here we see that, where the approximation holds, the cyclotron damping is exponentially small. To observe this effect in an experiment, at reasonable temperatures, one would consequently need to work very close to cyclotron resonance.

Near cyclotron resonance, the expansion approximation is no longer valid. A numerical solution of Eq. (3.22) is required for ω real and k complex. Various solutions have been presented previously in the literature [28,32,34]. Drummond [28] gave a set of curves for $\nu \neq 0$ and $v_t \neq 0$ for the refractive index vs ω_c/ω, with ω_p^2/ω^2 as parameter. His refractive index at cyclotron resonance checks against Eq. (3.26) when collisional effects are negligible. In Willett's [32] work, an additional assumption, $k_i v_t \ll \nu$, was made to facilitate numerical calculation. Since close to the cyclotron resonance k_i is large due to electron random motion, and at high temperature more electrons will have large $v_{\parallel}$, his calculated results will not be good at high electron temperature, or for ω_c/ω close to unity. In Motz's work [34], the problem was formulated in terms of the plasma dispersion function, Z_F, and eight curves were presented for $v_t \neq 0$, but $\nu = 0$. The curves are plotted as complex refractive index against ω_c/ω. These solutions are not in the most convenient form to us. Consequently, we have programmed Eq. (3.22), and run additional solutions. The results are plotted in the usual $\omega - k_r$ and $\omega - k_i$ planes, for $\nu = 0$ in Fig. 3.5, and $\nu \neq 0$ in Fig. 3.6. The general trend of our results

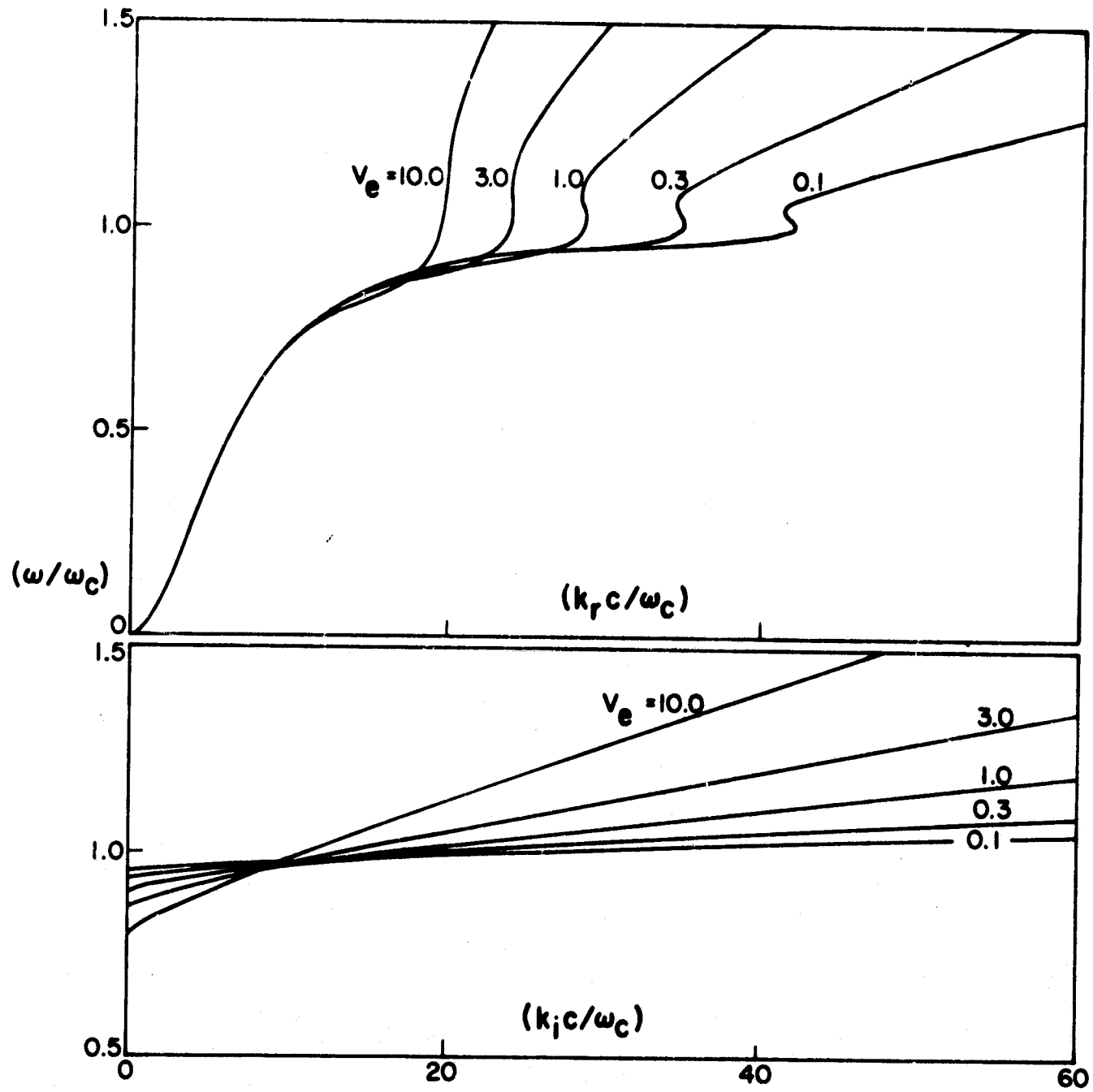

FIG. 3.5. WHISTLER DISPERSION CHARACTERISTICS FOR PLASMA WITH MAXWELLIAN VELOCITY DISTRIBUTION $[\omega_p^2/\omega_c^2 = 40,\ \nu = 0]$.

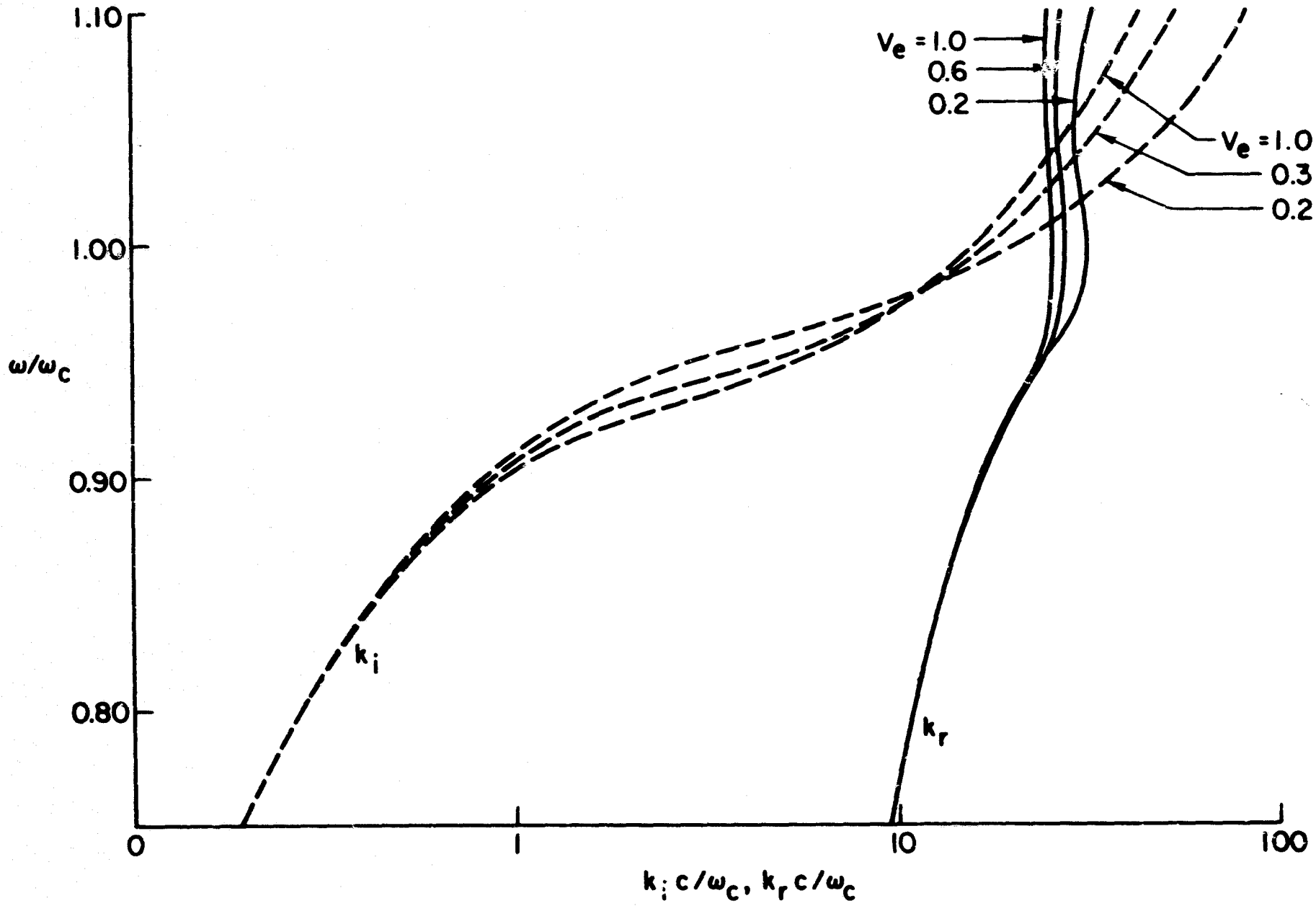

FIG. 3.6. WHISTLER DISPERSION CHARACTERISTICS FOR PLASMA WITH MAXWELLIAN VELOCITY DISTRIBUTION $[\omega_p^2/\omega_c^2 = 30,\ \nu/\omega_c = 0.01]$.

agrees with those of Motz for $\nu = 0$, and those of Drummond for $\nu \neq 0$, i.e., the resonance effect upon the whistler wave at the cyclotron frequency is broadened by electron temperature and/or collisions with strong damping.

The following point should be noted in connection with the computations in Figs. 1 and 5 of Motz's work. It seems that a lower electron temperature broadens the real part of the refractive index curve close to the cyclotron frequency more so than a higher electron temperature. To check this rather suprising feature, some of the curves were recalculated with the same parameters as were used by Motz. Our calculations check the results of Motz's Figs. 2 and 5 very well. However, his Fig. 1 differs very drastically close to resonance for the real part of the refractive index, and the imaginary part is completely different. Exactly at resonance, Eq. (3.22) can be solved as a cubic equation for the refractive index, as indicated in Eq. (3.26). When checked by this method, our calculations agree while Motz's results of Fig. 1 do not. The comparison is shown in Fig. 3.7.

With the new calculation for his Fig. 1, higher electron temperature always broadens the real part of the refractive index curve close to the cyclotron frequency, as compared with the rest of his calculated curves. The numerical results of our Fig. 3.5 also show this tendency.

4. General Conclusions on Collisional and Cyclotron Damping

From the analytical and numerical solutions of the dispersion relations, some general features of the collisional and temperature effects on whistler propagation can be summarized as follows:

(1) For $\omega/\omega_c < 1$, collisions are the dominant damping mechanism [Eqs. (3.15) and (3.34)]. For $\omega/\omega_c \approx 1$, both the electron temperature and collisions are important [Fig. 3.6].

(2) The attenuation per wavelength near the cyclotron frequency, is smaller when collisions and temperature are both present than with collisions alone. [Fig. 3.6].

(3) When $\nu = 0$, the real part of k shows a relative maximum near resonance, which increases as ω_p^2/ω_c^2 and decreases as v_t/c [Fig. 3.5].

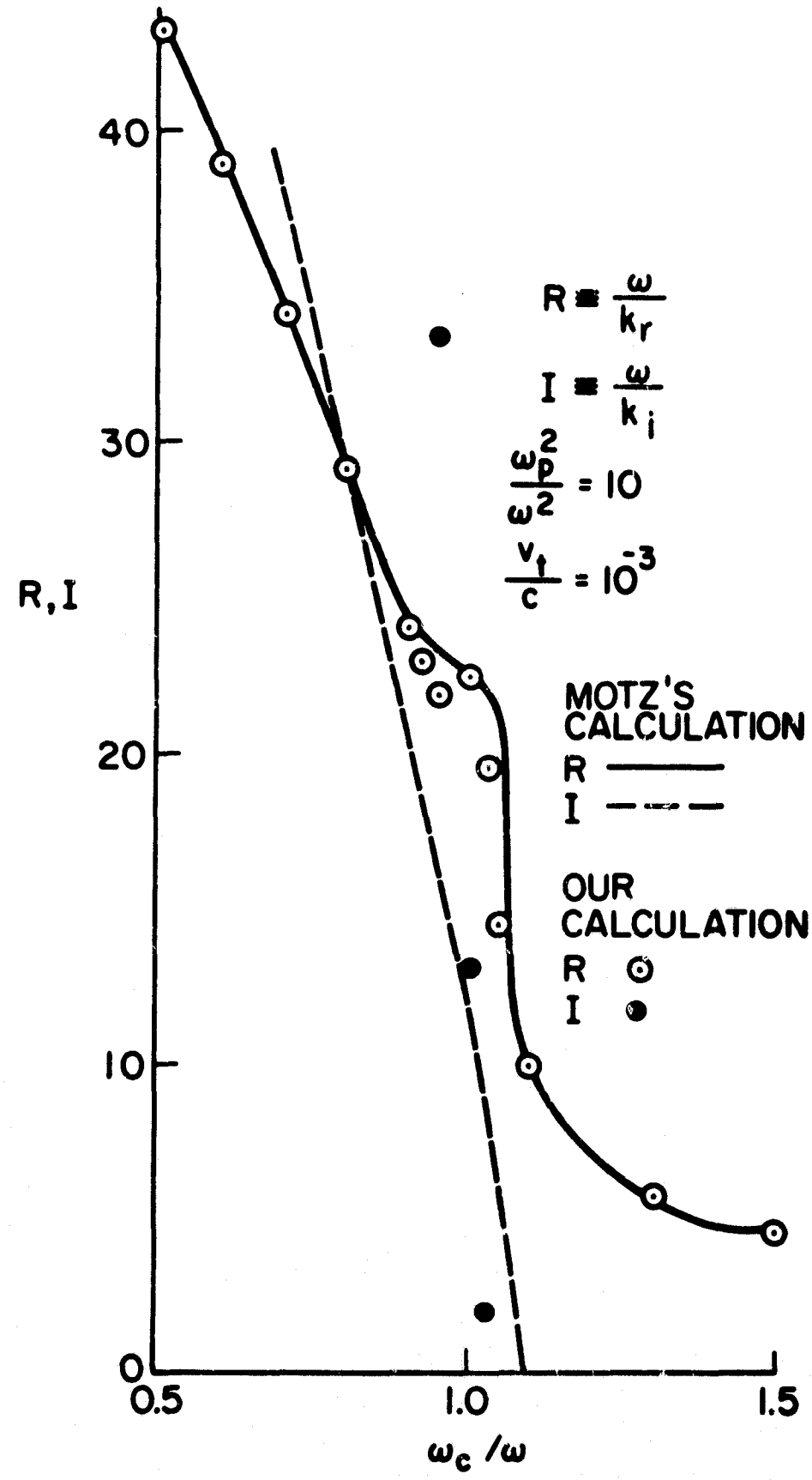

FIG. 3.7. COMPARISON OF WHISTLER COMPLEX REFRACTIVE INDEX WITH MOTZ'S RESULTS.

(4) Collisions always reduce k_r, while a Maxwellian distribution increases k_r slightly at low frequencies and then reduces k_r very close to cyclotron resonance [Eqs. (3.15) and (3.13)].

(5) Temperature alone does not make the evanescent cold plasma mode above the cyclotron frequency propagate whereas collisions do [Eqs. (3.20) and (3.26)].

C. Whistlers in Bounded Magnetoplasma

1. Statement of the problem

Whistlers are generally analyzed in terms of infinite plane wave solutions of Maxwell's equations for an infinite homogeneous magnetoplasma. In a laboratory plasma, or in a field-aligned column of enhanced ionization in the magnetosphere, the effects of the boundaries of the plasma may play an important role in determining the propagation characteristics of these waves. A few boundary value problems for homogeneous plasma columns in a uniform axial magnetic field have been solved numerically [22-24], and it has been found that the presence of sharp boundaries changes the wave dispersion drastically for certain ranges of parameters, sometimes beyond recognition from that prevailing in the unbounded medium. Since there must be a generic relationship between waves in bounded media and waves in the unbounded medium, the investigation of this is important.

Wieder [24] examined the properties of circularly symmetrical waves propagating in a dense, homogeneous, collisionless plasma, immersed in a uniform magnetic field and bounded by a conducting wall. He found that below cyclotron resonance an infinite number of propagating modes are possible. When the wavelength becomes much smaller than the transverse dimensions of the plasma the dispersion characteristics of these waves approach those of the corresponding plane whistler waves only if the frequency is above about half the cyclotron frequency. By intuition based on waveguide theory, one would expect the dispersion characteristics of the waves to approach those of the corresponding plane waves, in the limit of small wavelength, for all frequencies below the cyclotron

frequency. A way out of the difficulty was found by Hedvall and Sjögren [25], who solved a boundary value problem for an infinite plasma slab numerically, including collisions. They showed that by making the collision frequency sufficiently large, the dispersion characteristics for waves below half the cyclotron frequency would approach those of plane whistler waves in an infinite plasma, provided ω_p is adjusted so that the wavelengths are small compared to the plasma transverse dimensions. Although this avoids the paradox discovered by Wieder, it does not explain it. We shall now investigate the relationship between waves in bounded and unbounded magnetoplasma with the aim of elucidating this problem.

2. Whistler Propagating at an Angle to the Magnetic Field

In a transversely bounded plasma, plane whistlers cannot propagate exactly along the boundary because of the circularly polarized nature of the wave. The dispersion relations for the two characteristic plane waves propagating in an arbitrary direction in an infinite homogeneous plasma, in a uniform steady magnetic field, B_0, are given by the Appleton-Hartree equation [14],

$$\mu^2 \equiv \frac{c^2k^2}{\omega^2} = 1 - \frac{\omega_p^2}{\omega(\omega - i\nu) - \frac{\omega_c^2\omega^2 \sin^2\theta}{2\left(\omega^2 - i\nu\omega - \omega_p^2\right)} \pm \left[\frac{\omega_c^4\omega^4 \sin^4\theta}{4\left(\omega^2 - i\nu\omega - \omega_p^2\right)^2} + \omega^2\omega_c^2 \cos^2\theta\right]^{1/2}} \tag{3.31}$$

where θ is the angle between the direction of propagation and the static magnetic field, $\underset{\sim}{B}_0$. The polar plot of the refractive index (μ vs. θ) in Fig. 3.8 shows sections of two distinct surfaces obtained for

$$\frac{\omega}{\omega_c} \gtrless \frac{\omega_p^2 - 2\omega^2}{2\left(\omega_p^2 - \omega^2\right)} , \tag{3.32}$$

respectively [62].

The dispersion relations of the different modes can be conveniently characterized by the phase velocity surfaces. These are polar plots of the phase velocity in the plane containing $\underset{\sim}{B}_0$. At fixed values

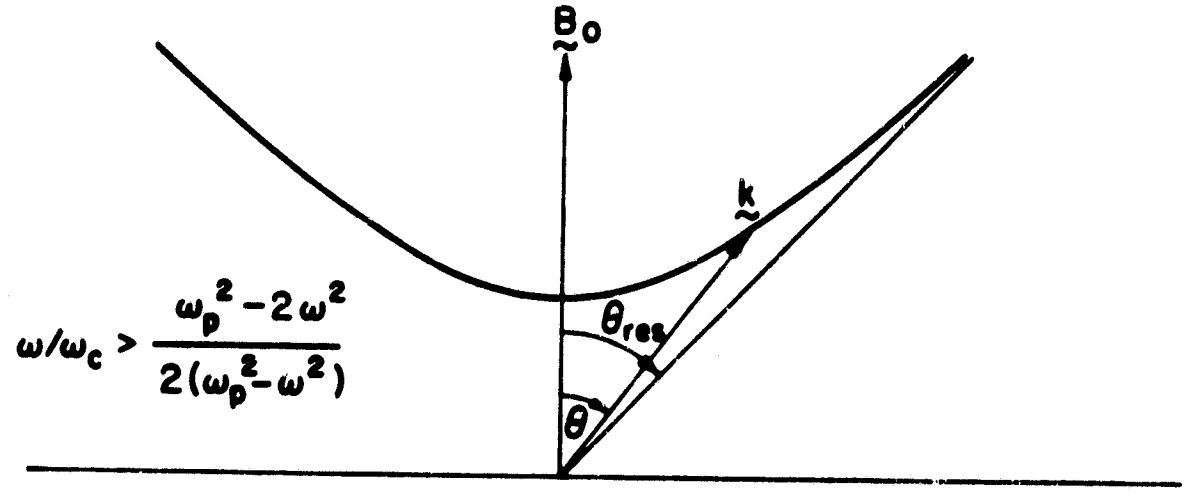

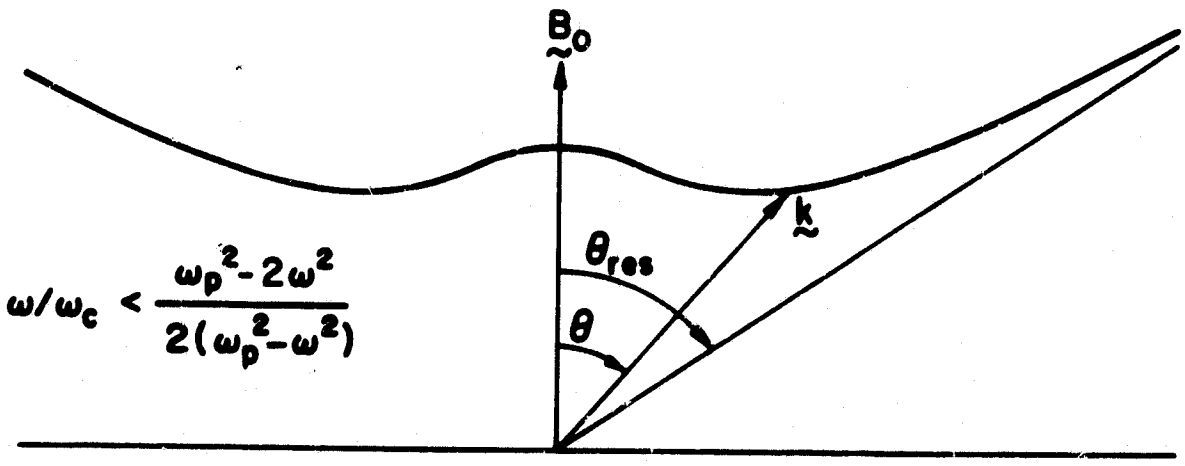

FIG. 3.8. WHISTLER REFRACTIVE INDEX SURFACES.

of the parameters ω_p, ω_c, one obtains in general two nonintersecting phase velocity surfaces. These surfaces will change continuously as the parameters ω_p, ω_c change, unless one passes through a point of resonance, $\mu \to \infty$; or point of cutoff, $\mu = 0$. The total picture is summarized in Fig. 3.9 [5]. Region 8 of Fig. 3.9 is a region where the whistler is the only propagating mode. When $\theta = 0$, Eq. (3.31) reduces to

$$\frac{c^2k^2}{\omega^2} = 1 + \frac{\omega_p^2}{\omega(\omega - i\nu \pm \omega_c)} . \tag{3.33}$$

Here the plus and minus signs before ω_c correspond to the left and right hand polarized waves. When $\theta \neq 0$, but

$$\omega_c^2\omega^2 \tan^2\theta \sin^2\theta \ll 4 \left| (\omega^2 - i\nu\omega - \omega_p^2)^2 \right| , \tag{3.34}$$

Eq. (3.31) reduces to

$$\frac{c^2k^2}{\omega^2} = 1 - \frac{\omega_p^2}{\omega(\omega - i\nu \pm \omega_c \cos\theta)} . \tag{3.35}$$

This is the well known "quasi-longitudinal" approximation [13]. For large ω_p^2/ω^2, the above approximation is good over a large range of θ. Under the condition of Eq. (3.34), the wave polarization is nearly circular, so that the approximation is sometimes called "quasi-circular" [5].

3. Resonance Cone

By rotating the curve of refractive index vs. θ about the direction of the static magnetic field, the refractive index surface is generated. By setting $k = \infty$ in Eq. (3.31), the resonance cone, θ_{res} is obtained. This yields

$$\tan^2\theta_{res} = \frac{\left(\omega^2 - \omega_p^2 - i\nu\omega\right)\left[(\omega - i\nu)^2 - \omega_c^2\right]}{\omega_c^2\omega_p^2 - \left(\omega^2 - \omega_p^2 - i\nu\omega\right)\left[(\omega - i\nu)^2 - \omega_c^2\right]} . \tag{3.36}$$

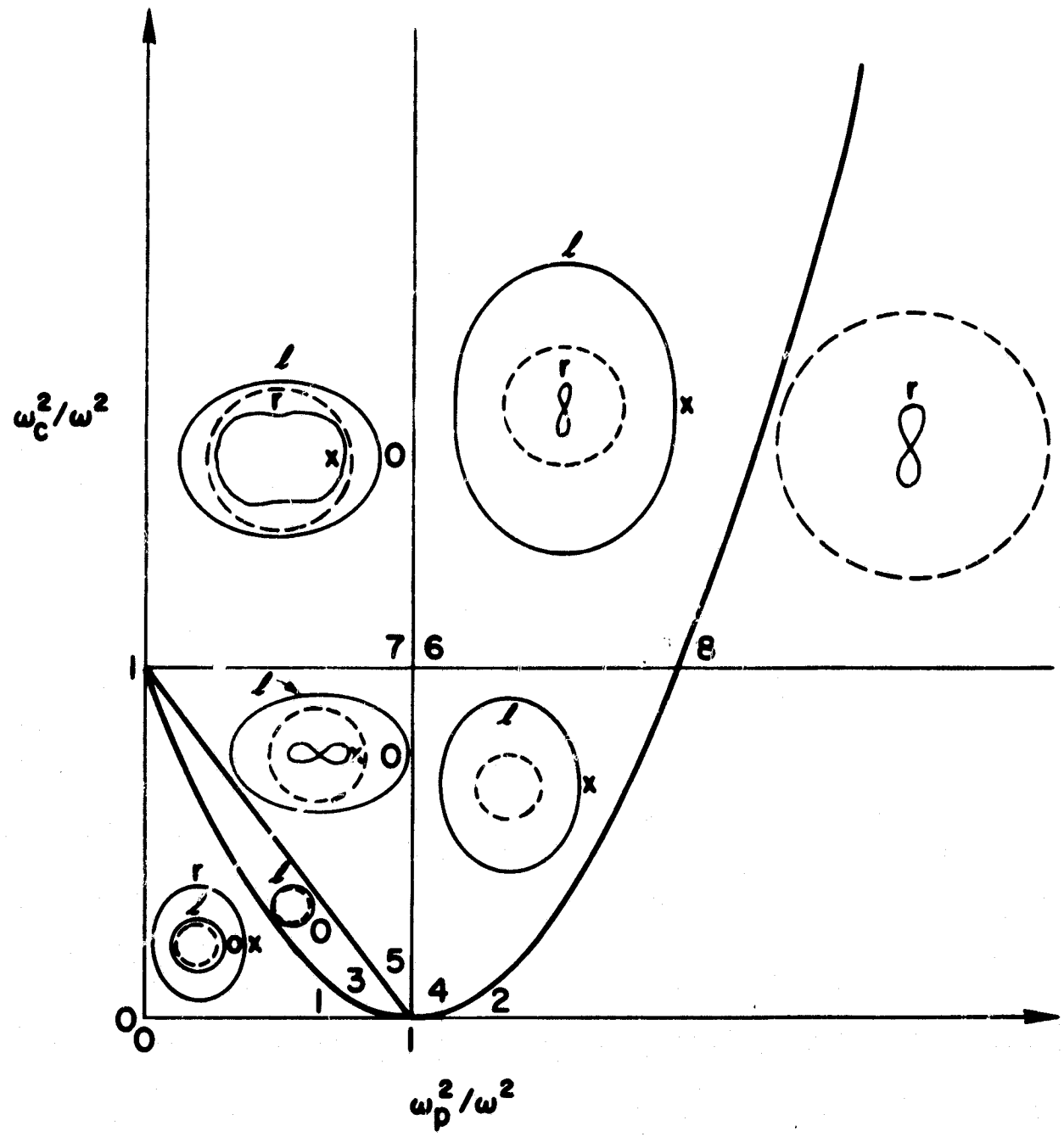

FIG. 3.9. CMA DIAGRAM AND PHASE VELOCITY SURFACES.

For $\nu = 0$, and under the usual whistler condition $\omega_p >> \omega_c > \omega$, the resonance angle, θ_{res}, is real, and is given by

$$\theta_{res} = \tan^{-1}\left[\frac{\left(\omega_p^2 - \omega^2\right)\left(\omega_c^2 - \omega^2\right)}{\omega^2\left(\omega_p^2 + \omega_c^2 - \omega^2\right)}\right]^{1/2} . \qquad (3.37)$$

Under the quasi-longitudinal condition (Eq. (3.34)), the resonance angle is given by

$$\theta_{res} = \cos^{-1}\left(\frac{\omega}{\omega_c}\right)^{1/2} . \qquad (3.38)$$

The refractive index surface in Fig. 3.9 is contained within the resonance cone. The resonance cone is very thin $(\theta_{res} \to 0)$ near cyclotron resonance, and widens as ω_c/ω increases. For $\omega_c/\omega = 4.3$, the resonance angle is about 60°. Beyond the resonance angle, the wave is essentially evanescent. Near the resonance cone the wave will be heavily damped, as can be seen from Eq. (3.34) for the whistler mode. Typical solutions of Eq. (3.36) are shown in Fig. 3.10.

4. The Generalized Snell's Law

Consider a plane horizontal boundary between a semi-infinite homogeneous plasma and a semi-infinite dielectric, and let the y- and z-axes be in the boundary plane while x is measured vertically upwards. Let a plane wave be incident obliquely on the boundary from the plasma side, with its wave-normal in the x-z plane at an angle θ_I to the z-axis. Then any field component of this wave is given by

$$\underset{\sim}{F} = \underset{\sim}{F}_I \exp\{-i \frac{\omega}{c} \mu(\theta_I)(z \cos\theta_I + x \sin\theta_I)\} . \qquad (3.39)$$

Because of the birefringent nature of the magnetoplasma, in general there will be two reflected waves in the plasma and a transmitted wave in the dielectric, with their wave-normals at angles θ_{R1}, θ_{R2}, and θ_T to

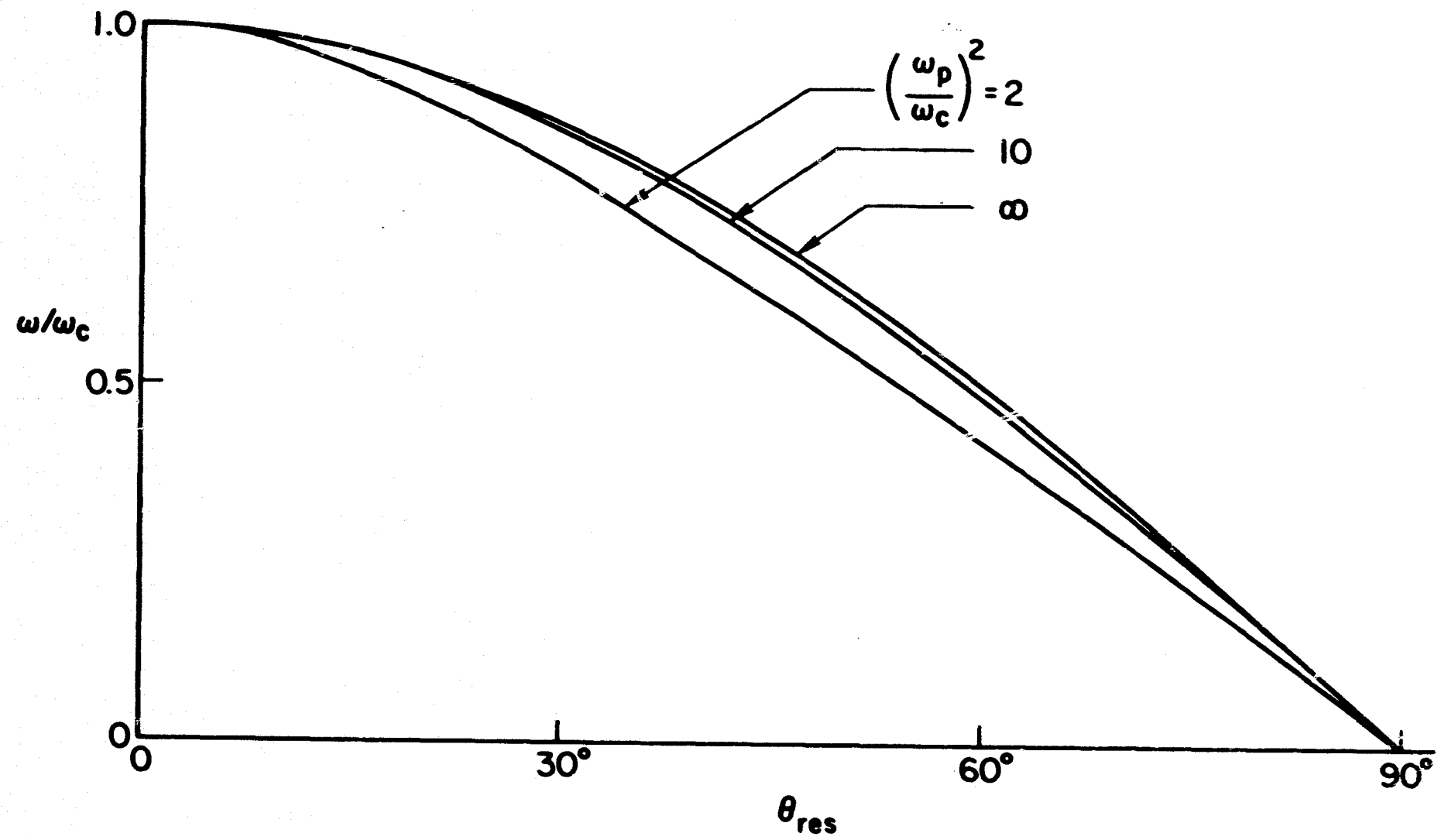

FIG. 3.10. WHISTLER RESONANCE CONE ANGLE.

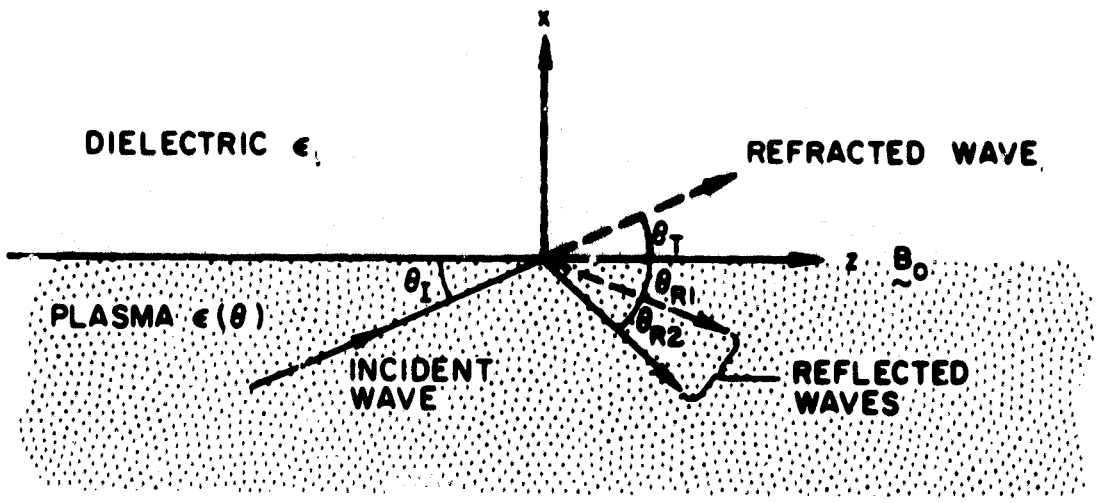

FIG. 3.11. REFLECTION AND REFRACTION OF A PLANE WAVE AT A SHARP MAGNETOPLASMA BOUNDARY.

the z-axis respectively (see Fig. 3.11). The field components, $\underset{\sim}{F}$, of these waves are given by:

Reflected waves:

$$\underset{\sim}{F}_R = \underset{\sim}{F}_{R1} \exp\{ - i \frac{\omega}{c} \mu(\theta_{R1})(z \cos \theta_{R1} - x \sin \theta_{R1})\}$$

$$+ \underset{\sim}{F}_{R2} \exp\{ - i \frac{\omega}{c} \mu(\theta_{R2})(z \cos \theta_{R2} - x \sin \theta_{R2})\} , \qquad (3.40)$$

Transmitted waves:

$$\underset{\sim}{F}_T = \underset{\sim}{F}_T \exp\{- i \frac{\omega}{c} \mu_d(z \cos \theta_T + x \sin \theta_T)\} , \qquad (3.41)$$

where μ_d is the refractive index of the dielectric.

Since the field components for both sides of the boundary must be in phase over the whole y-z plane, i.e., for $x = 0$, we must have

$$\mu(\theta_I) \cos \theta_I = \mu(\theta_{R1}) \cos \theta_{R1} = \mu(\theta_{R2}) \cos \theta_{R2} = \mu_d \cos \theta_T . \qquad (3.42)$$

Equation (3.42) is the generalized Snell's law [13]. By its application, θ_T can be found easily when θ_I is known. For $\underset{\sim}{B}_0$ parallel to the z-axis, we can let one of the two reflection angles be equal to θ_I. This reflected wave will be called the "principal" reflected wave. For the other reflected wave, which we shall term the "secondary" reflected wave, the Booker quartic is used [13] to find the angle.

5. The Booker Quartic

On the plasma side of the boundary, let

$$S = \mu(\theta) \cos \theta \quad , \quad q = \mu(\theta) \sin \theta \; . \tag{3.43}$$

The quantity q, determining the field variations in the x-direction, was first introduced into magneto-ionic theory by Booker, and it plays an important part in the theory of radio wave propagation in the ionosphere. The equation governing this quantity depends solely on the properties of the medium, and is, in general, a quartic. When the static magnetic field is parallel to the boundary plane, and in the plane of incidence, the quartic reduces to a biquadratic equation,

$$\alpha q^4 + \gamma q^2 + \epsilon = 0 \; , \tag{3.44}$$

where

$$\alpha = \omega(\omega - i\nu)\left[(\omega - i\nu)^2 - \omega_c^2\right] - \omega_p^2(\omega - i\nu)^2 \; ,$$

$$\gamma = -2(1 - i\nu/\omega)\left[\omega(\omega - i\nu) - \omega_p^2\right]\left[(1 - S^2)\,\omega(\omega - i\nu) - \omega_p^2\right]$$

$$+ 2\omega_c^2\left[(1 - S^2)\,\omega^2 - \omega_p^2\right] ,$$

$$\epsilon = \left[\omega(\omega - i\nu) - \omega_p^2\right]\left[(1 - S^2)\,\omega(\omega - i\nu) - \omega_p^2\right]$$

$$- (1 - S^2)\,\omega_c^2\left[(1 - S^2)\,\omega(\omega - i\nu) - \omega_p^2\right] - S^2\omega_p^2\omega_c^2(1 - S^2) \; .$$

In a study of waves on an electron beam, Hahn arrived at the same equation for the separation constants in cylindrical coordinates [63].

The four solutions of the quartic equation specify four waves. Two solutions represent waves travelling towards the interface; the other two represent waves travelling away from the interface into the plasma. All four waves are travelling in the positive z-direction. From Poynting vector considerations, only the latter pair of solutions are of interest.

Starting with θ_I, the incident angle, $\mu(\theta_I)$ is calculated from Eq. (3.31). Then, with $S^2 = \mu^2(\theta_I) \cos^2 \theta_I$, we determine q_1^2 and q_2^2 from Eq. (3.44). The two reflection angles are determined by trigonometrical relations in the complex domain. We may assume that the incident wave is a propagating wave, so that the incident angle is real. With this assumption, a typical set of incident and reflected angle relations were calculated for $\theta_I = 10°$, and are shown in Fig. 3.12.

6. The Reflected and Refracted Fields

To determine the amplitude and phase of the reflected waves in the plasma, and those of the refracted waves in the isotropic dielectric region, we must match the field components in the plasma side of the interface. With no surface current in the interface, the boundary conditions require the tangential electric field, the normal displacement, and the tangential and normal magnetic fields, to be continuous across the interface. For the incident wave we have:

$$E_{Ix} = \cos \theta_I + \frac{R(\theta_I)\, \omega_c \omega \sin^2 \theta_I}{\omega(\omega - i\nu) - \omega_p^2} [\mu^2(\theta_I) - 1], \quad E_{Iy} = iR(\theta_I),$$

$$E_{Iz} = \frac{R(\theta_I)\, \omega_c \omega \sin \theta_I \cos \theta_I}{\omega(\omega - i\nu) - \omega_p^2} [\mu^2(\theta_I) - 1] - \sin \theta_I,$$

$$H_{Ix} = - i\mu(\theta_I)\, R(\theta_I) \cos \theta_I, \quad H_{Iy} = \mu(\theta_I), \quad H_{Iz} = i\mu(\theta_I)\, R(\theta_I) \sin \theta_I, \tag{3.45}$$

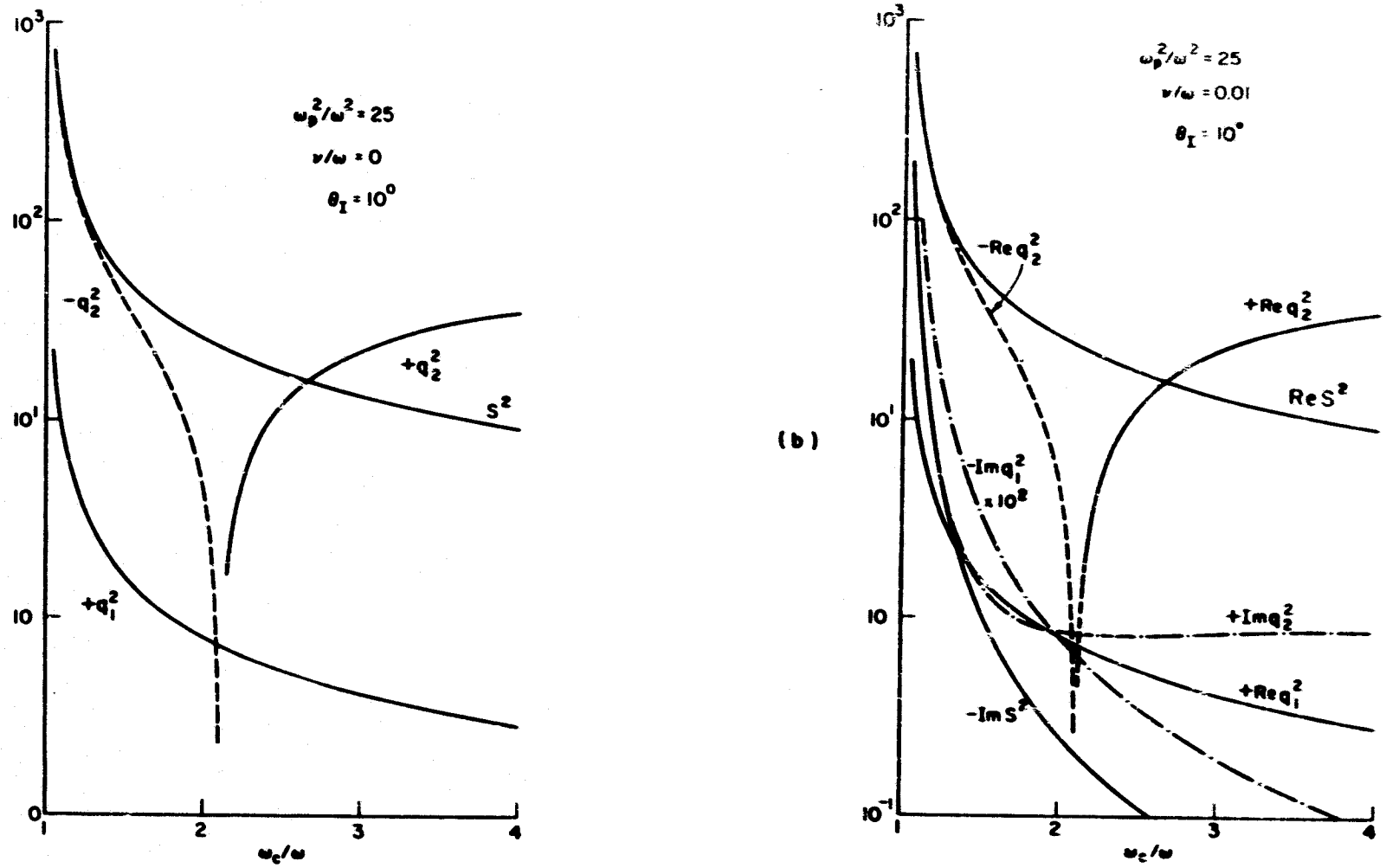

(a) $\nu/\omega = 0$ (b) $\nu/\omega = 0.01$

FIG. 3.12. PERPENDICULAR AND PARALLEL WAVENUMBERS IN A BOUNDED MAGNETOPLASMA [$\omega_p^2/\omega^2 = 25$, $\theta_I = 10^\circ$].

where

$$R(\theta) \equiv \frac{-\omega_c \omega \sin^2 \theta}{2\left[\omega(\omega - i\nu) - \omega_p^2\right] \cos \theta} + \left\{ \frac{(\omega_c \omega)^2 \sin^4 \theta}{4 \cos^2 \theta \left[\omega(\omega - i\nu) - \omega_p^2\right]^2} + 1 \right\}^{1/2} ,$$

$$\mathcal{H} \equiv \left(\frac{\mu_0}{\epsilon_0}\right)^{1/2} H ,$$

and the electric field component perpendicular to the plane wave propagation direction has been normalized to unity.

Let Γ_1 and Γ_2 be the reflection coefficients for the principal and secondary reflected waves in the plasma. The field components for the reflected waves are then given by,

$$E_{Rx} = \Gamma_1 E_{Ix} + \Gamma_2 \left[\cos \theta_{R2} + \frac{R(\theta_{R2})\, \omega_c \omega \sin^2 \theta_{R2}}{\omega(\omega - i\nu) - \omega_p^2} \left[\mu^2(\theta_{R2}) - 1\right] \right] ,$$

$$E_{Ry} = \Gamma_1 E_{Iy} + i\Gamma_2 R(\theta_{R2}) ,$$

$$E_{Rz} = \Gamma_1 E_{Iy} + \Gamma_2 \left[\frac{R(\theta_{R2})\, \omega_c \omega \sin \theta_{R2} \cos \theta_{R2}}{\omega(\omega - i\nu) - \omega_p^2} \left[\mu^2(\theta_{R2}) - 1\right] - \sin \theta_{R2} \right] ,$$

$$\mathcal{H}_{Rx} = \Gamma_1 \mathcal{H}_{Ix} - \Gamma_2 \mu(\theta_{R2})\, R(\theta_{R2}) \cos \theta_{R2}, \quad \mathcal{H}_{Ry} = \Gamma_1 \mathcal{H}_{Iy} + \Gamma_2 \mu(\theta_{R2}) ,$$

$$\mathcal{H}_{Rz} = \Gamma_1 \mathcal{H}_{Iz} + i\Gamma_2 \mu(\theta_{R2})\, R(\theta_{R2}) \sin \theta_{R2} . \qquad (3.46)$$

Because of the circularly polarized nature of the incident wave, we need both E-type (E field in the plane of the incident wave) and H-type (H field in the plane of incident wave) "refracted" waves, in the isotropic dielectric.

E-wave:

$$E_{Tz} = - T_E \sin \theta_T, \quad E_{Tx} = T_E \cos \theta_T, \quad H_{Ty} = T_E , \tag{3.47}$$

H-wave:

$$E_{Ty} = T_H, \quad H_{Tx} = - T_H \cos \theta_T, \quad H_{Tz} = T_H \sin \theta_T , \tag{3.48}$$

Here, T_E and T_H are the transmission coefficients. Because of the high refractive index for the incident wave, the waves on the dielectric side are generally evanescent (total reflection). By assuming a rigid boundary, the reflection and transmission coefficients can be determined from the following boundary conditions:

$$E_y(+0) = E_y(-0), \quad E_z(+0) = E_z(-0) ,$$

$$H_y(+0) = H_y(-0), \quad H_z(+0) = H_z(-0) , \tag{3.49}$$

where the signs "+" and "-" refer to the fields immediately adjacent to the boundary on opposite sides of it. These relations are obtained by applying Faraday's law and Ampere's law to a rectangular loop enclosing the boundary. There are two other boundary conditions, namely continuity of normal magnetic field and discontinuity of electric flux density due to surface charge. These are equivalent to Eq. (3.49) for the boundary considered here.

When these boundary conditions are applied to Eqs. (3.45) through (3.48), we obtain

$$iR(\theta_I) + \Gamma_1 iR(\theta_I) + \Gamma_2 iR(\theta_{R2}) = T_H ,$$

$$(1 - \Gamma_1)\left[\frac{R(\theta_I)\,\omega_c\omega \sin\theta_I \cos\theta_I}{\omega(\omega - i\nu) - \omega_p^2}\left[\mu^2(\theta_I) - 1\right] - \sin\theta_I\right]$$

$$- \Gamma_2\left\{\frac{R(\theta_{R2})\,\omega_c\omega \sin\theta_{R2} \cos\theta_{R2}}{\omega(\omega - i\nu) - \omega_p^2}\left[\mu^2(\theta_{R2}) - 1\right] - \sin\theta_{R2}\right\} = - T_E \sin\theta_T ,$$

$$\mu(\theta_I) + \Gamma_1\mu(\theta_I) + \Gamma_2\mu(\theta_{R2}) = T_E ,$$

$$i\mu(\theta_I)\,R(\theta_I)\sin\theta_I - i\Gamma_1\mu(\theta_I)\,R(\theta_I)\sin\theta_I$$

$$- i\Gamma_2\mu(\theta_{R2})\,R(\theta_{R2})\sin\theta_{R2} = T_H \sin\theta_T . \qquad (3.50)$$

Equation (3.50) can be solved for Γ_1, Γ_2 and T_H, T_E. For whistlers propagating at an angle to the magnetic field within the resonance cone, the refractive index, $\mu(\theta_I)$, is usually very large compared to unity. When $\mu(\theta_I) > \mu_0$, the angle of the refracted wave in the dielectric becomes complex and total reflection occurs. The two reflection coefficients are in general complex. A set of typical values for Γ is given in Fig. 3.13.

For frequencies above about $\omega_c/2$, $|\Gamma_1|$ is exactly equal to unity when collisions are neglected, and $|\Gamma_2|$ is of order of unity. Since, then, the secondary reflected wave has very large imaginary transverse propagation constants, it is localized at the boundary. The secondary reflected wave is a whistler "propagating" at an imaginary angle. Another boundary placed more than a few skin-depths away (say 10), will not change the secondary reflected fields appreciably. Thus the primary reflected wave will be reflected back and forth between the boundaries, just as in an ordinary dielectric slab waveguide. This is illustrated in Fig. 3.14(a).

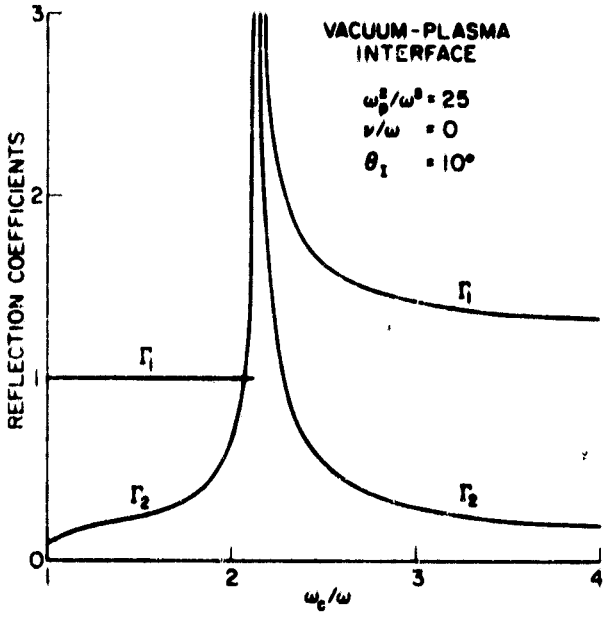

(a)

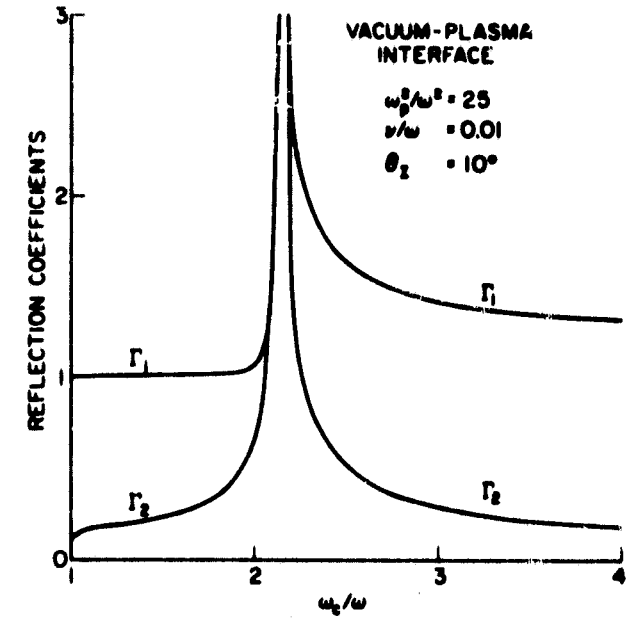

(b)

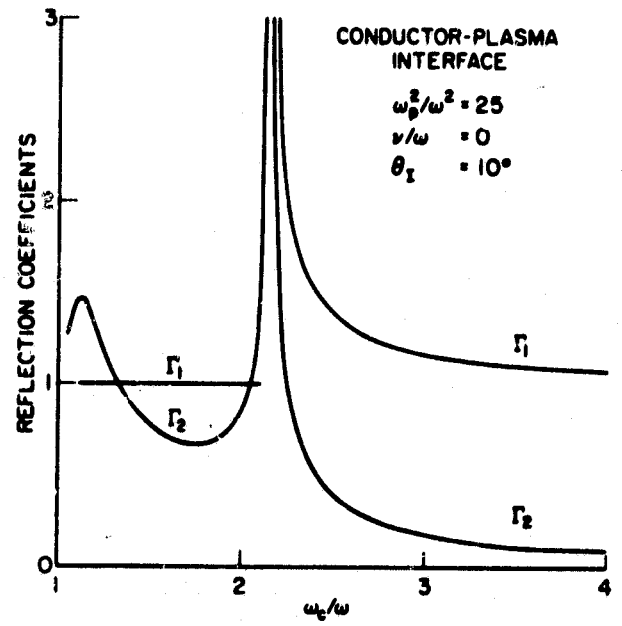

(c)

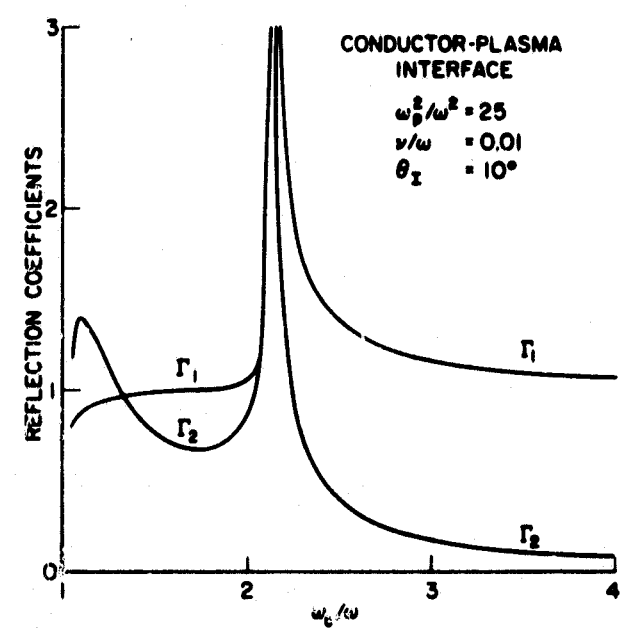

(d)

FIG. 3.13. PRINCIPAL AND SECONDARY REFLECTION COEFFICIENTS FOR WHISTLER INCIDENT AT AN ANGLE TO A SHARP MAGNETOPLASMA BOUNDARY.

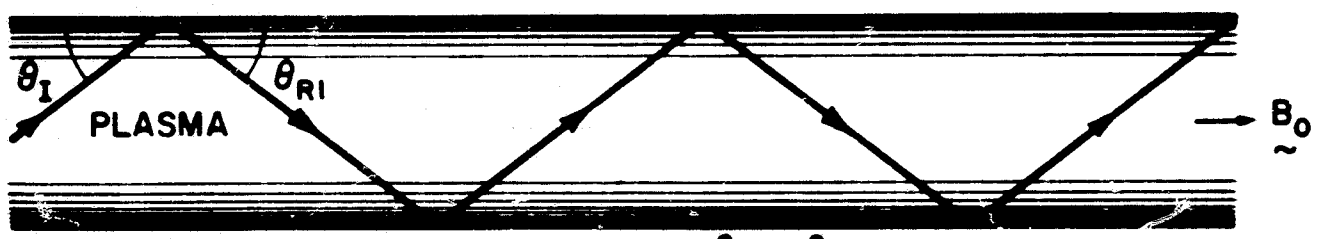

(a) $\omega / \omega_c > \dfrac{\omega_p^2 - 2\omega^2}{2(\omega_p^2 - \omega^2)}$

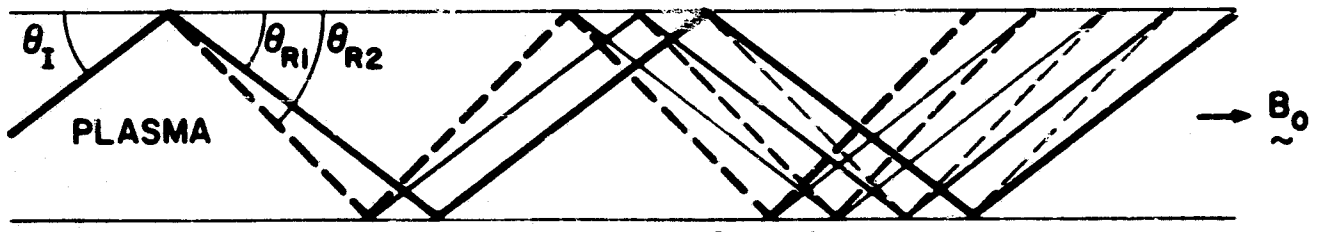

(b) $\omega / \omega_c < \dfrac{\omega_p^2 - 2\omega^2}{2(\omega_p^2 - \omega^2)}$

FIG. 3.14. COMPONENT PLANE WAVES IN A MAGNETOPLASMA SLAB.

Below half the cyclotron frequency, the secondary reflected wave also propagates as a whistler, propagating at a larger real angle than the principal reflected wave. If another boundary is present, the effect of the secondary reflected wave cannot be neglected, no matter how far away the other boundary is located.

Since in each reflection a new propagating wave is born, as shown in Fig. 3.14(b), a spectrum of waves finally results which explains, the interference pattern manifested in the calculations of μ by Wieder [24]. A few of his results are shown in Fig. 3.15(a). If collisions or electron temperature are introduced into the plasma model, we see in Fig. 3.9 that for small angles of incidence (grazing incidence), the primary reflected wave will be far away from the resonance cone, and will suffer little damping. Since the secondary reflected wave propagates at an angle much closer to the resonance cone, it will suffer much heavier damping, as seen from Eq. (3.34). Thus, with enough collisions, the interference pattern should disappear. Furthermore, as the wavelength is made small compared with the width of the plasma slab, e.g., by increasing ω_p, the plane wave solution for an unbounded plasma should be approached. This has been found by Hedvall and Sjögren. One of their results for μ is shown in Fig. 3.15(b).

In summary, we have explained Wieder's paradox as an interference pattern of plane waves which double due to birefringence in reflection. Our analysis also connects the well-studied plane wave theory in unbounded plasmas directly with the theory of waves in bounded plasmas. Since cylindrical waves and spherical waves can be synthesized in terms of plane waves [64], our result applies also to cylindrical and spherical configurations. We shall not consider the matter further, but proceed to examine the limitation of the quasistatic approximation in magnetoplasma problems.

7. Limitations of the Quasistatic Approximation

Of the numerous papers concerned with waves propagating through waveguides filled with cold collisionless magnetoplasma, the majority employ the quasistatic approximation [65,65]. In this approximation, the RF magnetic field is neglected ($\nabla \times \underset{\sim}{E} \approx 0$), so that the RF electric field can be simply derived from a scalar potential. The approximation

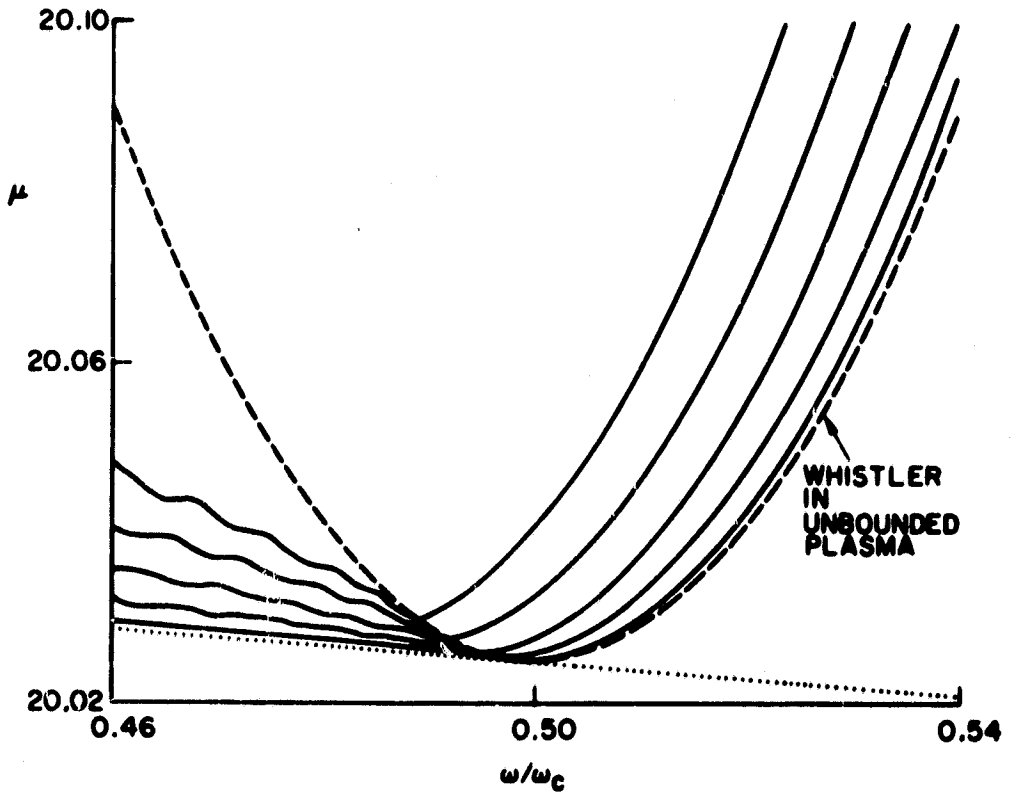

(a) Wieder's results [circular waveguide filled with magnetoplasma, $\omega_p^2/\omega_c^2 = 100$, $a\omega_c/c = \pi$, a is plasma radius].

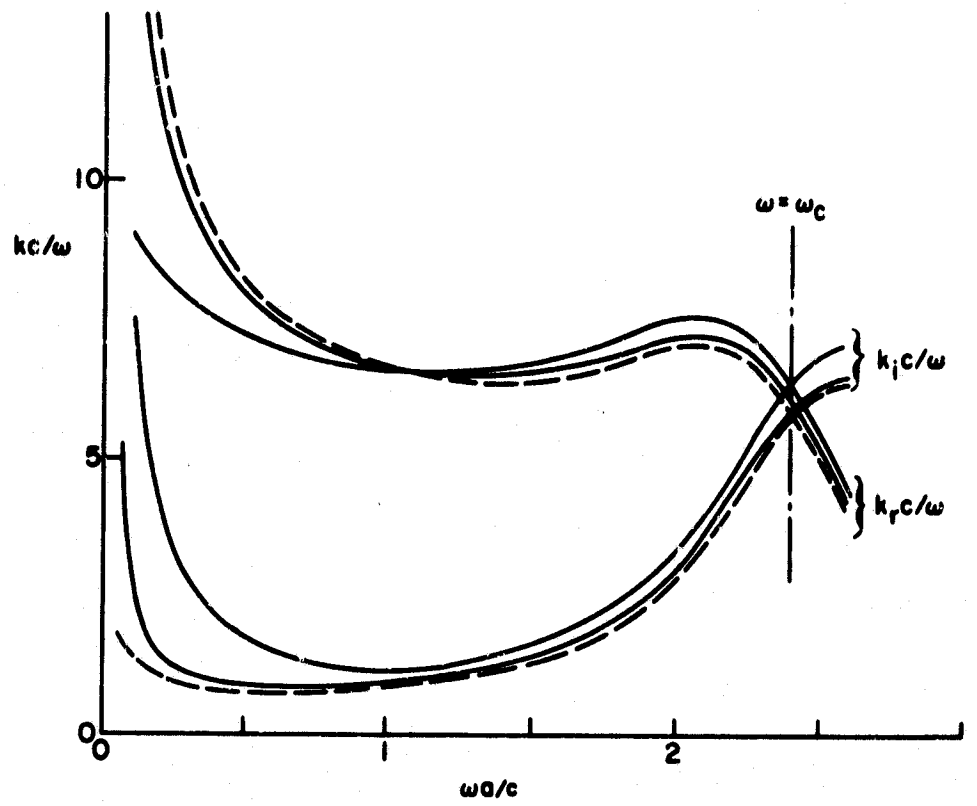

(b) Hedvall and Sjögren's results [plasma slab in vacuum, $\omega_p^2/\omega_c^2 = 11$, $a\omega_c/c = 2.4$, a is plasma width].

FIG. 3.15. WHISTLER DISPERSION CHARACTERISTICS IN BOUNDED MAGNETOPLASMA.

greatly simplifies the numerical solution of the corresponding dispersion relations. The original justification for the quasistatic approximation, as described by Trivelpiece and Gould [65], was the slowness of the phase velocity, so that retardation effects can be neglected. This justification is not always satisfactory since plane wave whistlers in unbounded plasmas are slow waves, yet they cannot be derived from quasistatic theory. On the other hand, phase velocities comparable to, or even greater than the velocity of light have been predicted by the quasistatic theory, which turned out to be very good approximations. [68].

A number of authors [66-68] have attempted to establish a general criterion for validity of the quasistatic approximation. By comparing a limited set of numerical calculations with the full Maxwell equations, and with the quasistatic approximation, it seemed that $\omega_p a/c \ll 1$ could be used as the criterion to justify the quasistatic approximation [22], where a is the plasma column radius. Based on a quasistatic analysis of power flow, additional criteria for the extension of the quasistatic approximation were derived [66]. Bevc [67-68] claims that quasistatic calculations of power flow are unsatisfactory and proposes to compare the laminar and solenoidal parts of the RF electric field as a criterion. It is true that in general

$$\underset{\sim}{E} = - \nabla\psi - i\omega\underset{\sim}{A} \quad , \tag{3.51}$$

and that when $|\nabla\psi| / |\omega A| \gg 1$, the quasistatic approximation is justified. However, $\underset{\sim}{A}$ and ψ are coupled, and the comparison can only be made after the full Maxwell's equations are solved. This is not satisfactory because the advantage of the quasistatic approximation has been to avoid using the full Maxwell equations.

For a waveguide completely filled with plasma in a uniform magnetic field, and $\omega_p > \omega_c$, the quasistatic approximation predicts two groups of waves with strong fields inside the plasma. The waves are called "body" waves. One group of backward waves propagate in the band between the hybrid frequency, $\omega_H [= (\omega_p^2 + \omega_c^2)^{1/2}]$, and the plasma frequency, ω_p. Another group of slow forward waves propagate between zero frequency and the cyclotron frequency.

For $\omega_p > \omega_c$, the forward slow wave of the quasistatic approximation can be viewed as a whistler propagating very close to the resonance cone and reflected at the boundary. Whistlers propagating at an angle to the external magnetic field, $\underset{\sim}{B}_0$, are physically coupled to plasma oscillations. Close to the resonance cone, the axial electric field dominates over the RF magnetic field. Therefore, the RF magnetic field can be neglected. From Eq. (3.45), the ratio of RF electric field, E, to RF magnetic field, $\mathcal{H}$, in a collisionless magnetoplasma, close to the resonance cone, is given by

$$\frac{|E|}{|\mathcal{H}|} = \frac{\omega_c \omega \sin\theta}{|\omega^2 - \omega_p^2|}\,\mu(\theta) = \frac{\omega_c \omega \sin\theta\,\lambda_0}{|\omega^2 - \omega_p^2|\,\lambda(\theta)} \quad , \tag{3.52}$$

where λ_0 is the signal wavelength in vacuum, and λ is the signal wavelength in the plasma. The width of the plasma slab, a, can be expressed in terms of the angle of propagation by the familiar waveguide relation

$$a = \frac{m\lambda(\theta)}{2\sin\theta} = \frac{m\,\lambda_0}{2\sin\theta\mu(\theta)} \quad , \tag{3.53}$$

where m is the transverse mode number. For bounded magnetoplasma, due to the secondary reflected wave, m is in general a fractional number. When θ is exactly equal to θ_{res}, the refractive index, μ, is infinite, and the size of the waveguide would have to be zero unless θ is also zero. But, in general, $\theta_{res} \neq 0$. Thus, in order to obtain a predominantly electrostatic solution, we must make θ close to θ_{res} so that the refractive index becomes very large but remains finite. Combining Eqs. (3.52) and (3.53), for $|E| \gg |\mathcal{H}|$ we have

$$\frac{m\pi\omega_c\omega c}{|\omega^2 - \omega_p^2|\,a} \gg 1 \quad . \tag{3.54}$$

This is the condition for the validity of the quasistatic approximation. The condition given by Eq. (3.54) can be applied to both the forward and

backward body wave modes. For the forward wave modes under the usual whistler conditions, $\omega_p >> \omega_c > \omega$, Eq. (3.54) reduces to

$$\frac{m\pi\omega_c c}{\omega_p^2 a} >> 1 \quad . \tag{3.55}$$

For the quasistatic approximation to be valid, we need strong magnetic fields, and/or low plasma densities and small plasma column cross-sections. The approximation is also improved by increasing the mode number. All these features agree with the result of numerical calculations [21] shown in Fig. 3.16.

For a waveguide partially filled with plasma, surface wave modes may propagate. Since the energy in surface waves is concentrated near the plasma boundary, the above conditions for the validity of the quasi-static approximation can not be applied to them. For surface waves the usual slow wave criterion is generally adequate.

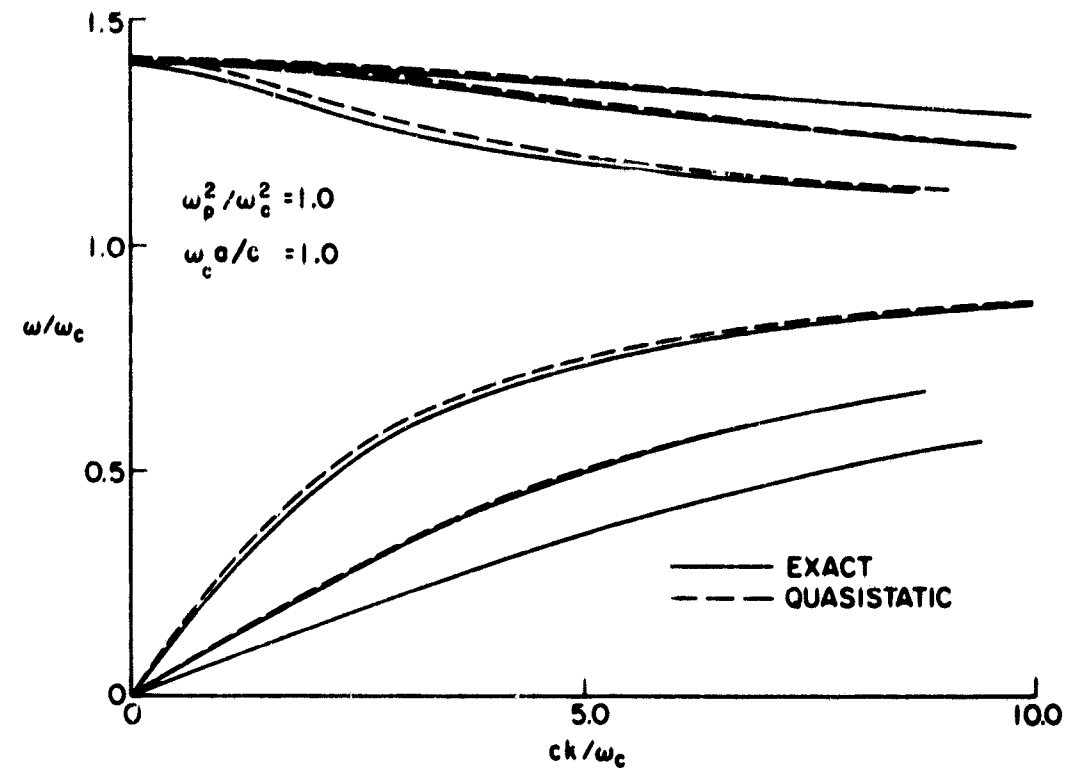

(a)

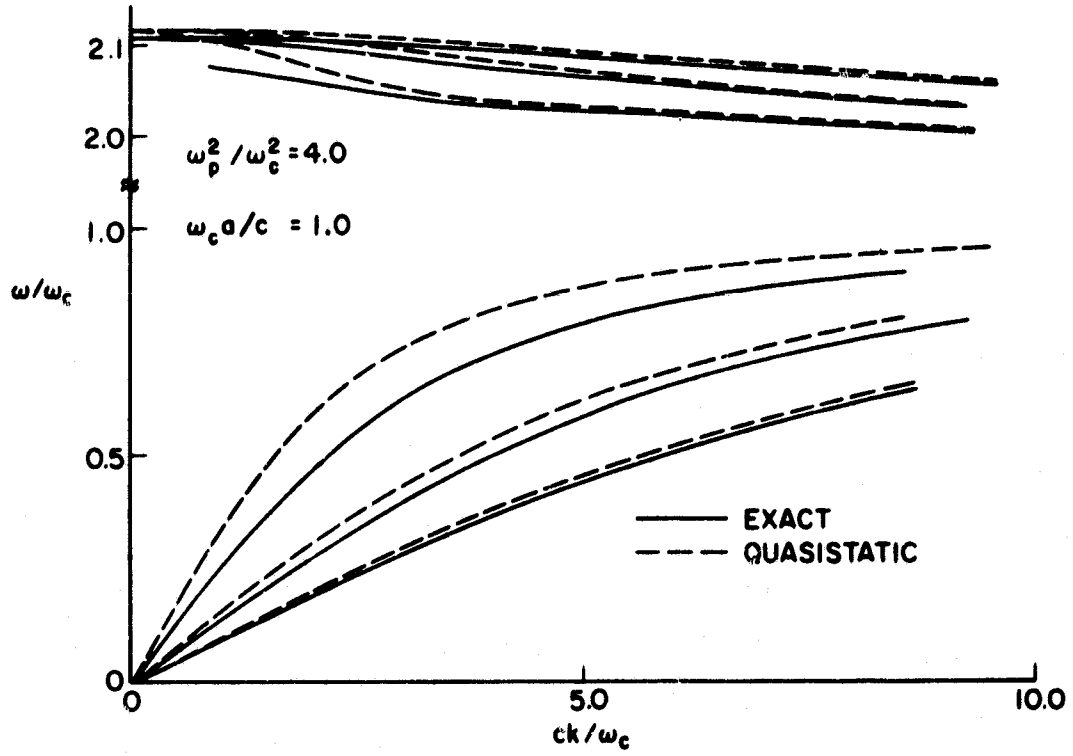

(b)

FIG. 3.16. COMPARISON OF BODY WAVE DISPERSION CURVES IN MAGNETOPLASMA FILLED WAVEGUIDE CALCULATED FROM FULL MAXWELL EQUATIONS, AND WITH QUASISTATIC APPROXIMATION [REF. 22].

IV. THE CHARACTERISTICS OF UNSTABLE WHISTLERS

Whistlers propagating in a plasma at thermal equilibrium, or which has any isotropic velocity distribution, will show cyclotron damping, and no instability, as proved in Appendix A. For anisotropic electron velocity distributions with greater transverse than parallel energy, electromagnetic instabilities may occur [40]. Such conditions may be found, for example, in plasmas confined by magnetic mirrors.

It is through the cyclotron resonance interaction that charged particles exchange kinetic energy with the electromagnetic energy of the wave. The direction of the energy exchange depends on the relative rotation phase of the particle with respect to the wave field. For a simple beam/plasma system, consisting of a monoenergetic beam interacting with a cold magnetoplasma, it can be shown that the $\underset{\sim}{v}_1 \times \underset{\sim}{B}_1$ force has a phase focusing effect allowing electrons to give up their transverse energy to amplify the wave [43]. Thus an electron beam without initial transverse energy cannot cause instability of whistlers propagating parallel to the magnetic field. Longitudinal velocity spread of the beam has a phase mixing effect tending to reduce the growth rate. The outcome of the competition between the wave damping and instability will depend on the details of the distribution function involved.

In a plasma with an anisotropic velocity distribution, the group of particles which support the wave, and the group of particles which drive the wave unstable are mixed together. The physical mechanism behind the instability is not easy to grasp. In a beam/plasma system, however, where the wave may be thought of as supported by the plasma and interacted with by the beam, the physical mechanism behind the instability can be seen clearly. To elucidate the physical mechanism, and characteristics of the whistler instability, a series of electron velocity distributions of increasing complexity will be considered in this chapter.

Following Penrose's [69] stability criterion, the customary procedure to examine an instability is to find the range of real wavenumbers for which the dispersion relation allows growing waves ($\omega_i < 0$). For whistlers, this has been studied by a number of authors [39-42, 47-49]. However, the precise temporal and spatial behavior of the instability

is not clear from these results. To settle the point, we will investigate the dispersion relation in detail, and will apply refined stability criteria developed by Derfler. Before we apply these criteria to whistlers, let us briefly review this subject.

A. Classification of Instabilities

In general, a dispersion relation, $D(\omega,k) = 0$, may be regarded as an equation for $\omega(k)$, or as an equation for $k(\omega)$. Which of the two cases is appropriate depends on the details of the physical system to which the theoretical model is applied. To determine whether the system described by a given dispersion relation is unstable in some sense, it is customary to solve the dispersion relation for real k. If solutions $\omega(k \text{ real})$ are found, for which $\omega_i < 0$ the system is said to be unstable. In the literature, it has often been suggested that the existence of such a solution is a proof that perturbations of the system grow in time. This is misleading in general, and only true if the finite length of a practical system imposes the condition that k is real within the unstable range.

Sturrock [71] has shown that it is meaningful to treat an infinitely long system by considering its response to a perturbation localized both in time and space, i.e., $\underset{\sim}{J}_{ext} = \underset{\sim}{J}_{\perp}\, \delta(t)\, \delta(z)$. For an unstable system, there are then two distinct types of instability. This distinction becomes apparent only after inversion of their Fourier and Laplace transforms. The inversion can be written in the form

$$E_R(z,t) = \int_C \frac{d\omega}{2\pi} \int \frac{dk}{2\pi} E_R[\omega,k] \exp i(\omega t - kz) \ , \qquad (4.1)$$

where $E_R[\omega,k]$ is the spectral amplitude of the corresponding wave [see Eq. (2.28)] and C is the Laplace contour in the lower half complex ω-plane, parallel to the real axis and below all singularities of the integrand. As $t \to \infty$, Eq. (4.1) may describe one of the two forms shown in Fig. 4.1. The pulse disturbance may grow in time at every point in space, or it may propagate away while growing in time, eventually leaving the plasma at any given point quiescent. The former instability is termed "nonconvective", while the latter is termed "convective". The importance

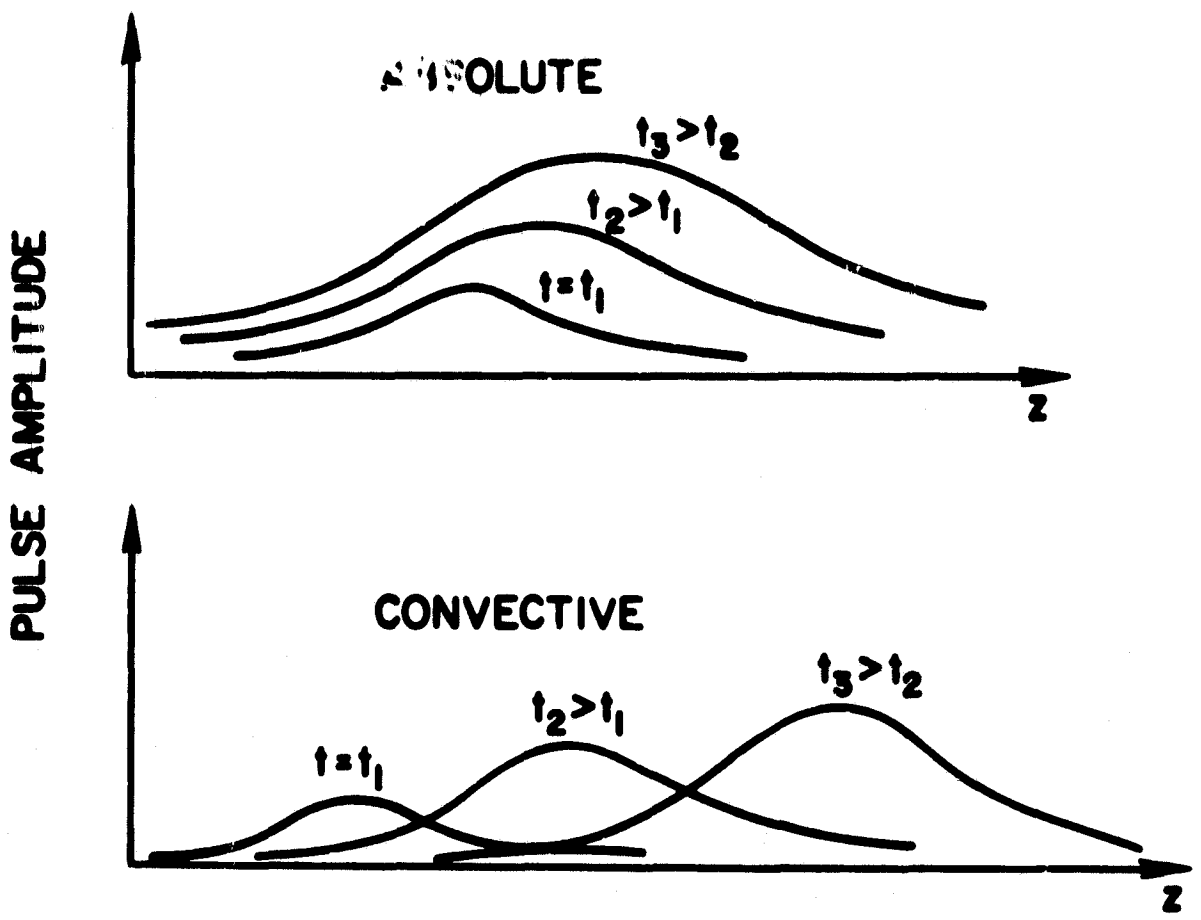

FIG. 4.1. ABSOLUTE AND CONVECTIVE INSTABILITIES.

of making the distinction now becomes clear. If the instability is convective, it should be possible to excite propagating waves having real ω and complex k, i.e., growing in space away from the source. If the instability is nonconvective, there will be growth from noise until the wave amplitude reaches a saturation level, for which the small-signal theory breaks down. We may conclude, then, that the existence of ω(k real) solutions with $\omega_i < 0$ is a necessary and sufficient condition that the system be unstable, but further examination is necessary to determine whether the instability is convective or nonconvective.

Criteria for determing the instability type, for ω real, and k real solutions were given by Sturrock for a rather restricted class of dispersion relations. Derfler derived more general criteria for electrostatic waves in his comprehensive treatment of the rf gap impedence in a hot plasma [56,57]. The approach used there is quite general and can be readily extended to other wave dispersion relations. Briggs [70] applied this method to various cold plasma waves.

For hot plasmas, the dispersion function $D(\omega,k)$ has two branches, the positive and negative frequency parts, which we have defined for the right hand polarized waves in Eq. (2.35). Because the two branches are connected by symmetry relations, such as Eq. (2.41), one of the two contains all the information. We can therefore determine the instability character from, say, the negative frequency part of the dispersion relation $D_-(\omega,k)$. Following Derfler, this can be done in two different ways: by conformally mapping $D_-(\omega,k) = 0$ either from the frequency plane into the wavenumber plane, or vice versa. His criteria for these cases are stated as follows:

1. The Colliding Pole Criterion [72]

Select a Laplace integral path $\omega_i = \text{const} < 0$ so that $D_-(\omega,k) \neq 0$ for all positive real k; start a process of analytic continuation towards real ω and observe the coalescence of Landau poles, $D_-(\omega,k_m) = 0$ and $D_-(\omega,k_n) = 0$, at saddle points $k = \bar{k}$. Nonconvective instability arises if, and only if, two poles collide across the positive real k axis and the corresponding branch point $\bar{\omega}$ is in the lower frequency plane, $\bar{\omega}_i < 0$. Otherwise, the system

supports convective instabilities when $\omega_i < 0$ for some positive real k, and evanescent waves when $\omega_i > 0$ for all positive real k.

2. The Frequency Cusp Criterion [73]

Map the positive real k-axis into the frequency plane. The system is stable and supports evanescent waves only if $\omega_i > 0$. When $\omega_i > 0$, map ordinates $k_r = \text{const}$ through corresponding abscissas $k > 0$ into the frequency plane, and observe the resulting loops. Nonconvective instability arises if, and only if, a contour can be found which "intersects" the map of the positive real k-axis twice and possesses a cusp, i.e., traces through a branch point $\bar{\omega}$, in the lower frequency plane $\omega_i < 0$. Otherwise, the system is convectively unstable.

When a part of the positive real k-axis maps into a closed loop within the lower frequency plane this criterion concludes, without further mapping, that the enclosed branch point, $\bar{\omega}$, represents a nonconvective instability.

In the following work we will apply the colliding pole criterion, except in one case where it is more convenient to use the frequency cusp criterion.

B. Whistler Interaction with Gyrating Electron Beams in Cold Plasmas

1. Dispersion Relation

The electrons of a gyrating electron beam populate a shifted ring in velocity space, and the electrons of a cold plasma just a point. These distribution functions are described by Dirac Delta functions in the form

$$f_p(v_\parallel, v_\perp) = \frac{1}{\pi}\,\delta(v_\parallel)\,\delta(v_\perp^2), \quad f_b(v_\parallel, v_\perp) = \frac{1}{\pi}\,\delta(v_\parallel - v_{0\parallel})\,\delta(v_\perp^2 - v_{0\perp}^2) \tag{4.2}$$

where $v_{0\parallel}$ is the beam velocity parallel to the magnetic field, and $v_{0\perp}$ the transverse speed. By substituting these distributions into Eq. (2.32) and integrating, the dispersion relation becomes

$$1 - \left(\frac{kc}{\omega}\right)^2 - \frac{\omega_p^2}{\omega(\omega - \omega_c)} - \left(\frac{\omega_b}{\omega}\right)^2 \left[\frac{\omega - kv_{0\parallel}}{\omega - kv_{0\parallel} - \omega_c} + \frac{v_{0\perp}^2 k^2}{2(\omega - kv_{0\parallel} - \omega_c)^2}\right] = 0 , \tag{4.3}$$

where ω_p and ω_b are the plasma frequencies of the plasma and of the beam, respectively. The terms inside the brackets are due to the beam, the first is a Doppler shifted beam term analogous to the term in ω_p^2, and the second is due to the initial transverse energy of the beam. It is the last term which introduces instability into the system. Bell and Buneman [41] analyzed Eq. (4.3) in the weak beam limit $[(\omega_b/\omega_c) \to 0]$, and found instabilities when the beam electrons oscillate with nearly the cyclotron frequency, i.e., when $\omega - kv_{0\parallel} \approx \omega_c$.

When the beam density is low, it is instructive to put Eq. (4.3) in the following form,

$$\left[1 - \left(\frac{kc}{\omega}\right)^2 - \frac{\omega_p^2}{\omega(\omega - \omega_c)}\right](\omega - kv_{0\parallel} - \omega_c)^2 = \frac{\omega_b^2}{\omega^2}\left[(\omega - kv_{0\parallel})(\omega - \omega_c - kv_{0\parallel}) + \frac{k^2 v_{0\perp}^2}{2}\right]. \tag{4.4}$$

When the right-hand side of Eq. (4.4) is small, the roots of this equation can be obtained approximately as

$$1 - \left(\frac{kc}{\omega}\right)^2 - \frac{\omega_p^2}{\omega(\omega - \omega_c)} = 0 , \tag{4.5}$$

$$(\omega - kv_{0\parallel} - \omega_c)^2 = 0 . \tag{4.6}$$

Equations (4.5) and (4.6) represent the whistler mode and beam waves, respectively. The way in which the beam/plasma interaction occurs for real wavenumbers, k, is illustrated in Fig. 4.2. Figure 4.2(a) shows the uncoupled whistler $(\omega_b = 0)$ and the uncoupled weak-beam waves $(\omega_p = 0)$, i.e., $\omega - kv_{0\parallel} = \omega_c$. Since $\omega < \omega_c$, it should be noted that $v_{0\parallel} < 0$, i.e., the beam wave and group velocity point in opposite directions.

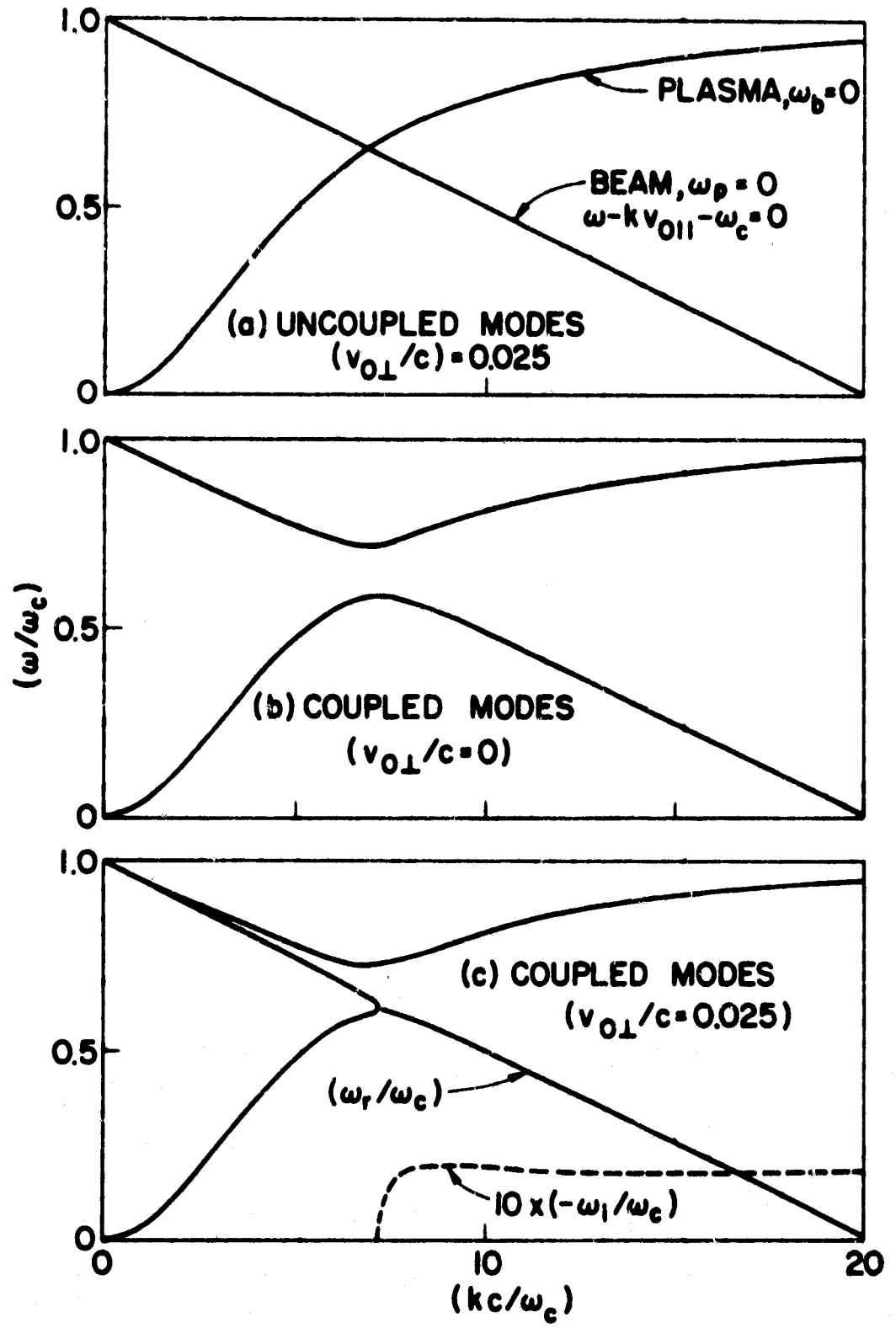

FIG. 4.2. BEAM/PLASMA INTERACTION FOR REAL k, ZERO PLASMA AND BEAM TEMPERATURES [$\omega_p^2/\omega_c^2 = 25$, $\omega_b^2/\omega_c^2 = 1$, $v_{0\parallel}/c = -0.05$].

Figure 4.2(b) illustrates the coupled modes in the absence of transverse beam energy. As $k \to \infty$ the upper branch approaches ω_c, while the lower approaches the uncoupled beam wave. In particular, ω is real for all k real. This implies that no instability is excited, which agrees with the conclusion of Neufeld and Wright [36] for these conditions. Figure 4.2(c) finally illustrates the effect of the transverse beam energy. There exists a value of k below which ω is real and above which ω is complex. As $k \to \infty$, we have

$$\omega \to \omega_c + kv_{0\parallel} \mp i \frac{\omega_b v_{0\perp}}{2^{1/2} c} , \qquad (4.7)$$

where the upper sign represents temporal growth, and the lower sign decay. For the parameters of Fig. 4.2, the maximum growth rate is $(-\omega_i/\omega_c) \approx 0.019$, i.e., 1.1 dB/cyclotron period. The corresponding ω_r and k are in the vicinity of the intersection of the uncoupled modes shown in Fig. 4.2(a). Physically, it might be expected that the most unstable waves would occur near that intersection. However, the gain is only slightly lower away from the coupling region, where the plasma should be unimportant. In fact, the instability there is due to the beam alone. This has been studied in detail by Bers, et al [43].

From the discussion, it follows that a real wave experiment would work when the beam has no transverse energy. In that case, we can solve the dispersion relation [Eq. (4.3)] for ω real, and obtain complex values of k in a narrow band of frequencies, as shown in Fig. 4.3. These, however, do not represent spatial growth but a damped wave. This follows from Sturrock's stability criteria for cold plasma [71]. This collisionless damping is closely related to the cyclotron damping discussed in Section B of Chapter III. When the beam has transverse energy, it does not make sense to solve the dispersion relation Eq. (4.3) for real ω, unless we can show that nonconvective instabilities are absent. This investigation will be carried out in the following sections.

2. Stability Analysis

To determine the instability character, we apply the colliding pole criterion described in Section A to the dispersion relation Eq. (4.3).

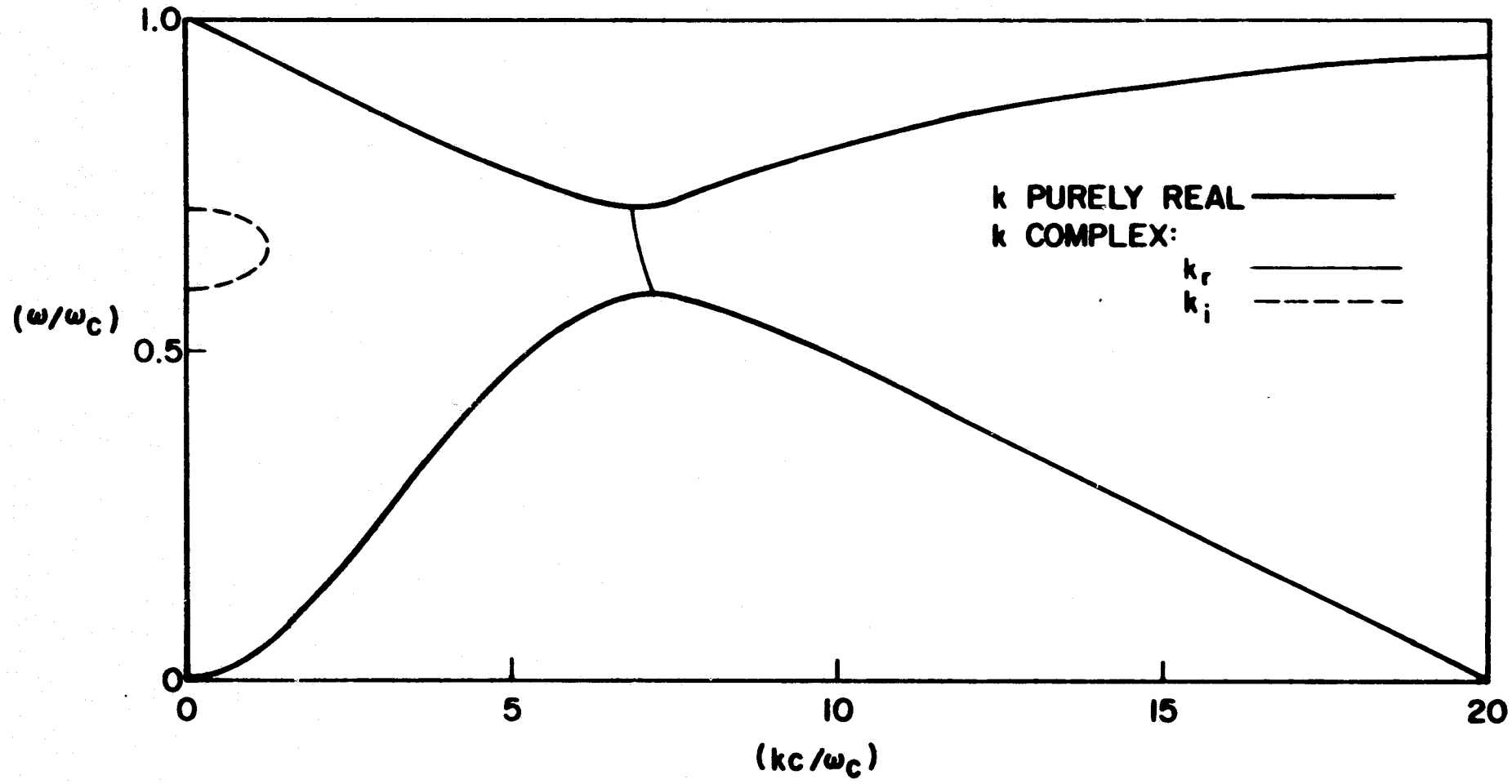

FIG. 4.3. BRILLOUIN DIAGRAM OF REAL ω vs. COMPLEX k ILLUSTRATING AN EVANESCENT WAVE DUE TO THE INTERACTION OF A COLD BEAM AND A COLD PLASMA $[\omega_p^2/\omega_c^2 = 25,\ \omega_b^2/\omega_c^2 = 1,\ v_{0\parallel}/c = -0.05,\ v_{0\perp}/c = 0]$.

By mapping lines $\omega_r = \text{const}$ and $\omega_i = \text{const} < 0$ into the wavenumber plane, we locate the saddle point $\bar{k}c/\omega_c = 7.29\text{-}i0.31$ shown in Fig. 4.4(a). Since this saddle point arises from a collision of two "Landau" poles k_1 and k_2, across the positive real k-axis, and the corresponding branch point, $\bar{\omega}/\omega_c = 0.598\text{-}i0.062$, is in the lower half plane, the system is nonconvectively unstable. The precise location of this frequency is a solution of the simultaneous equations

$$D(\omega,k) = 0 \quad , \quad \frac{\partial D(\omega,k)}{\partial \omega} = 0 \quad , \tag{4.8}$$

which say that the complex "group velocity", $\frac{d\omega}{dk}$ $[= -(\partial D/\partial k)/(\partial D/\partial \omega)]$, vanishes at that point. The "local" growth rate of the instability for $t \gg 0$ is therefore given by $(-\bar{\omega}_i/\omega_c) = 0.062$. Figure 4.5 shows the variation of this "resonance" frequency, $\bar{\omega}$, and wavenumber, $\bar{k}$, with the density $(\omega_b/\omega_c)^2$ of the beam, while Fig. 4.6 shows the location of $\bar{\omega}$ as a function of the drift velocity and the transverse energy of the beam. Clearly, $\bar{\omega}$ is restricted to the lower frequency plane in all these cases, and we must look for means to quench the nonconvective instability, so that a wave experiment with real frequency can be performed. As such, we shall now discuss the effects of collisions and temperature in the plasma, and the effect of a longitudinal velocity spread in the beam.

3. Effect of Collisions and Temperature in the Plasma

The only modification due to collisions in the plasma is that the term $\omega_p^2/\omega(\omega - \omega_c)$ in Eq. (4.3) is changed to $\omega_p^2/\omega(\omega - i\nu - \omega_c)$. The locus of the branch point, $\bar{\omega}$, is then modified as shown in Fig. 4.7 for several transverse beam velocities. For $v_{0\perp}/c = 0.025$, it is seen that a modest amount of collisions, $\nu/\omega_c = 0.033$, is sufficient to move $\bar{\omega}$ into the upper frequency plane, and thereby quench the nonconvective instability. This manifests itself in Fig. 4.4(b) by the fact that the collision between the "Landau" poles, k_1 and k_2, does not occur for frequencies $\omega_i \leq 0$. Yet, for strictly real ω, we find that $k_i < 0$, which is the characteristic of convective backward wave amplification. In this case, it makes sense to draw a Brillouin diagram for real ω vs. complex k, as shown in Fig. 4.8. Note that this convective

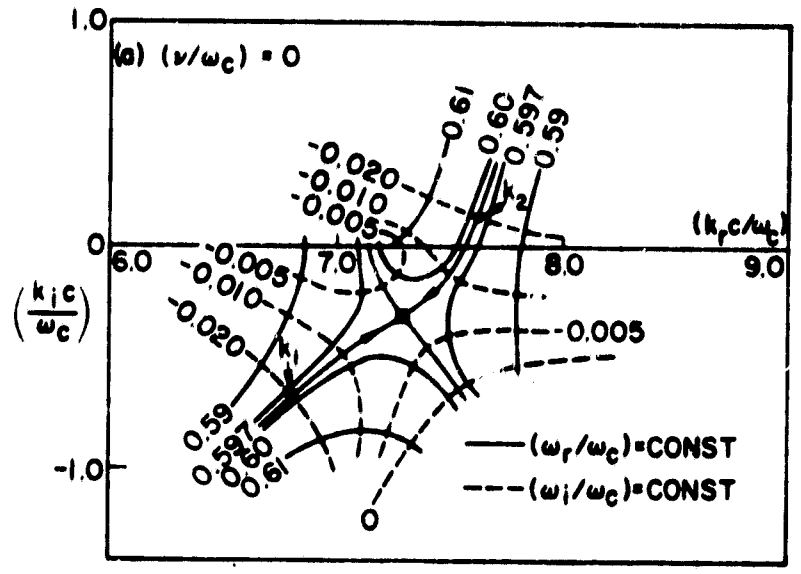

(a) $\nu/\omega_c = 0$

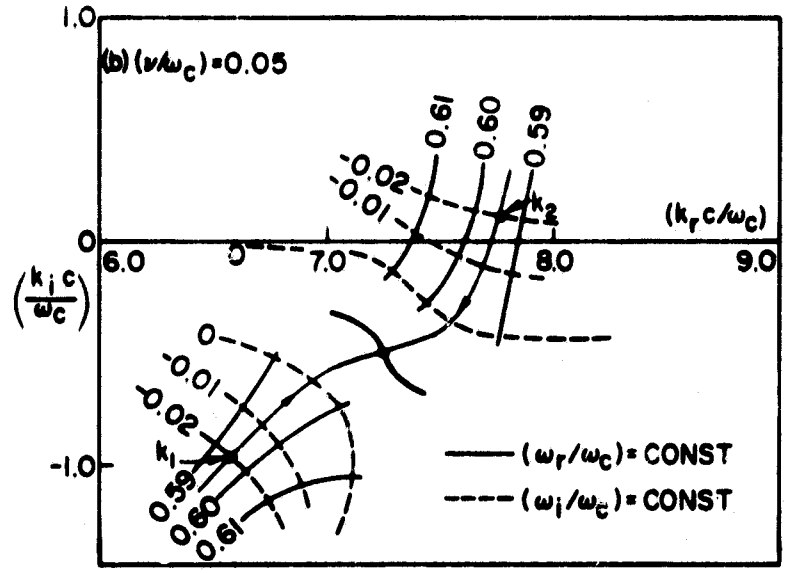

(b) $\nu/\omega_c = 0.05$

FIG. 4.4. CONTOUR MAP OF ORDINATES ω_r = const MAPPED FROM THE ω-PLANE INTO THE k-PLANE VIA EQ. (4.3) [$\omega_p^2/\omega_c^2 = 25$, $\omega_b^2/\omega_c^2 = 1$, $v_{01}/c = -0.05$, $v_{0\perp}/c = 0.025$].

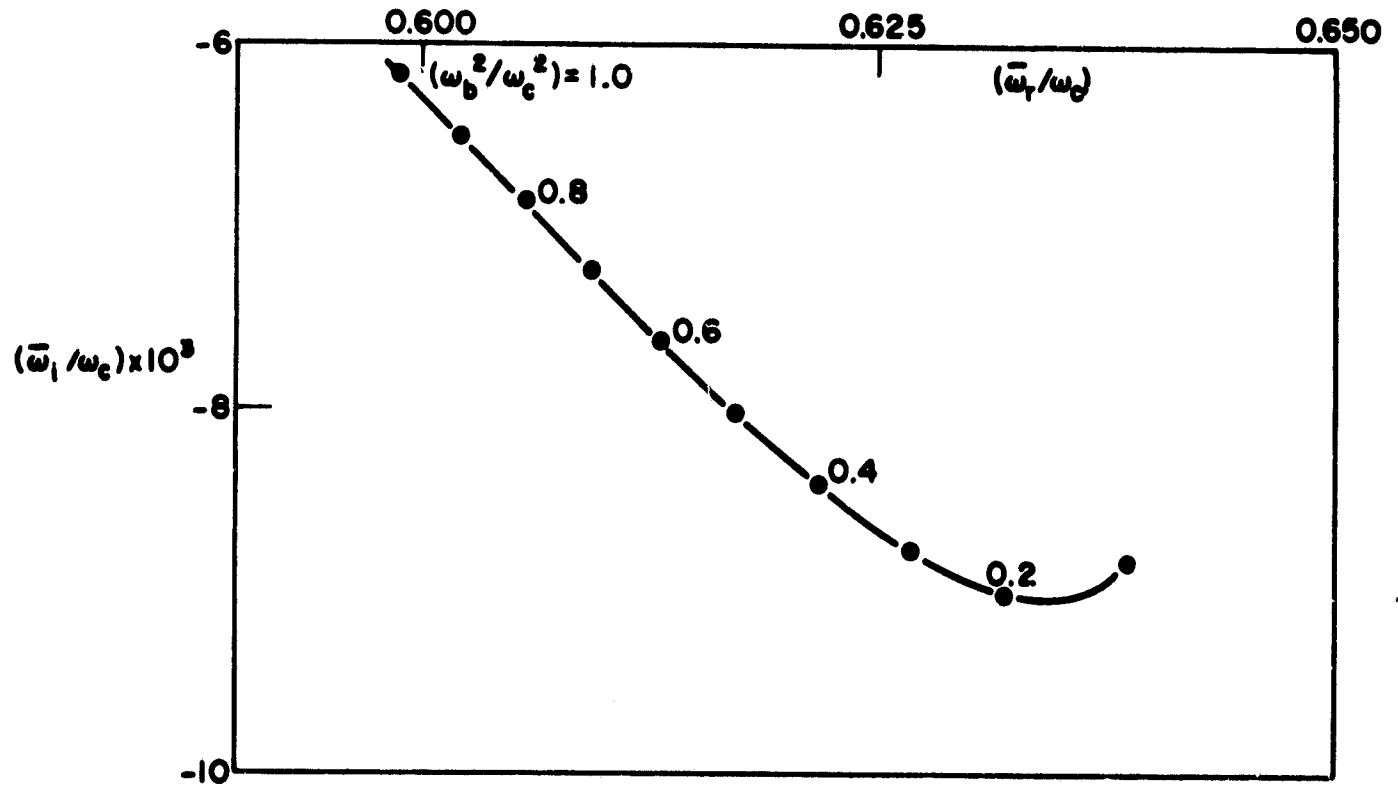

FIG. 4.5. LOCI OF BRANCH POINTS IN THE ω-PLANE AND SADDLE POINTS IN THE k-PLANE AS A FUNCTION OF ω_p^2/ω_c^2 $[\omega_p^2/\omega_c^2 = 25,\ v_{0\parallel}/c = -0.05,\ v_{0\perp}/c = 0.025]$.

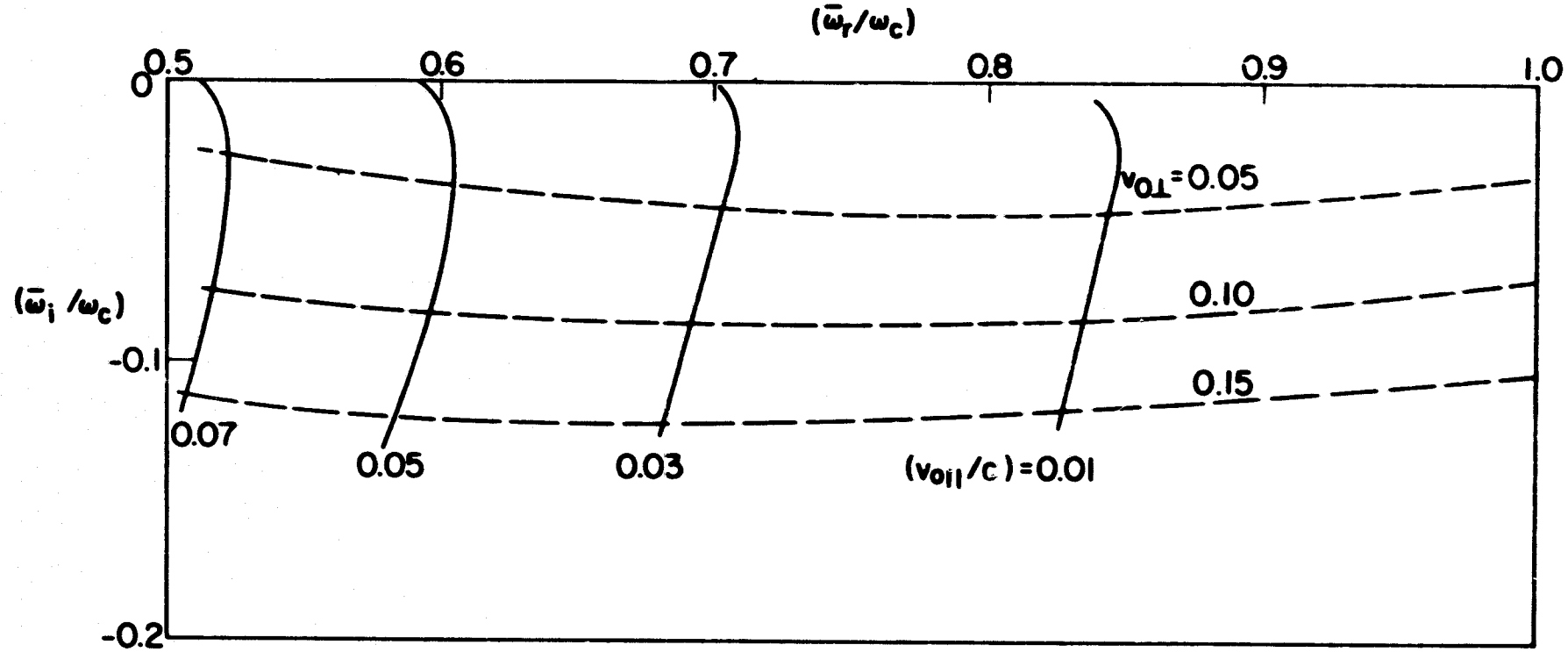

FIG. 4.6. LOCI OF BRANCH POINTS IN THE ω-PLANE AS A FUNCTION OF $v_{0\parallel}$ AND $v_{0\perp}$ $[\omega_p^2/\omega_c^2 = 25,\ \omega_b^2/\omega_c^2 = 1]$.

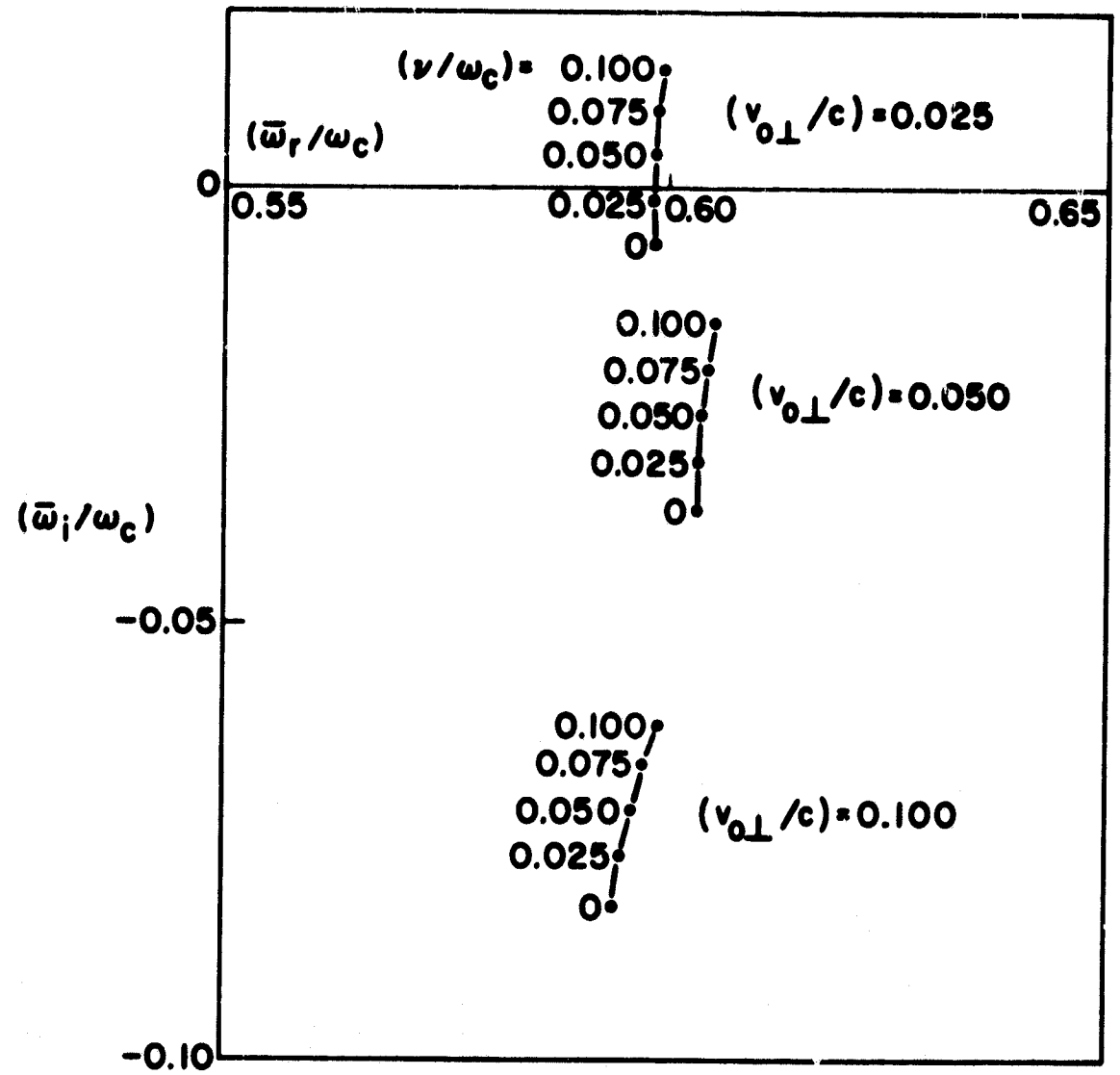

FIG. 4.7. LOCI OF BRANCH POINTS IN THE ω-PLANE AS A FUNCTION OF ν AND $v_{0\perp}$ $[\omega_p^2/\omega_c^2 = 25,\ \omega_b^2/\omega_c^2 = 1]$.

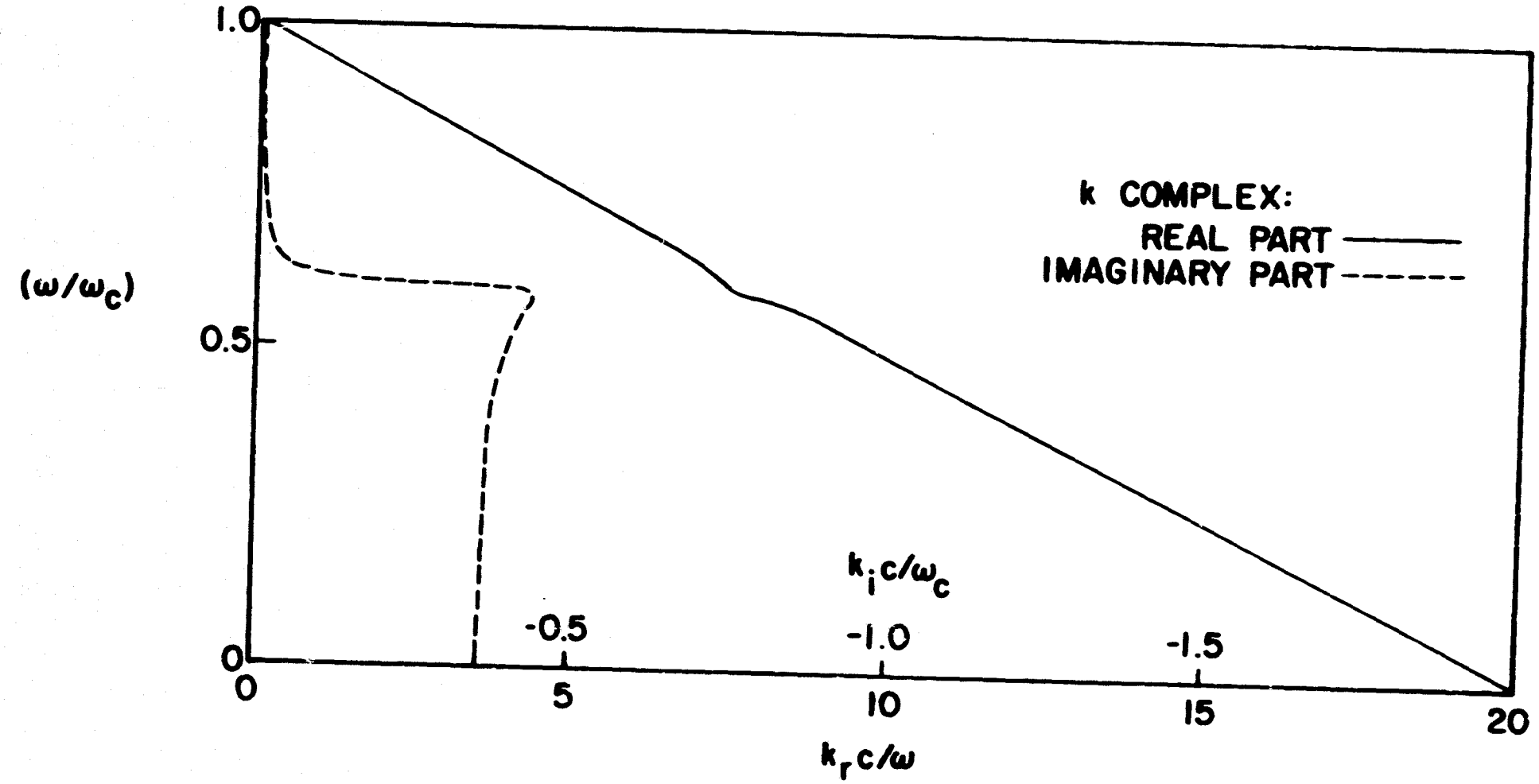

FIG. 4.8. BRILLOUIN DIAGRAM OF REAL ω vs. COMPLEX k [$\omega_p^2/\omega_c^2 = 25$, $\omega_b^2/\omega_c^2 = 1$, $v_{01}/c = -0.05$, $\nu/\omega_c = 0.05$].

instability is associated mainly with the beam. Another inspection of Fig. 4.7 shows, however, that this method of quenching the nonconvective instability is not so succesful when the transverse energy of the beam is large, and we must look for other means to do so.

The effect of plasma temperature may be understood most simply by choosing for the plasma electrons the resonance velocity distribution [Eq. (3.3)]. This has the effect of replacing $\omega_p^2/\omega(\omega - \omega_c)$ in Eq. (4.3) by $\omega_p^2/\omega(\omega - ikv_r - \omega_c)$. The treatment is then similar to that for collisions in that ν has been replaced by kv_r. From that, one would conclude that the velocity spread, v_r, of the plasma electrons is most effective in quenching short wave instabilities (k large). However, the fast electron content of the simple resonance distribution is unreasonably large, and therefore greatly overestimates the effect of damping. If we use a Maxwellian distribution instead, the plasma contribution in Eq. (4.3) is replaced by the "Fried" function, $Z(\xi)$, used in Eq. (3.22). Branch points, $\bar{\omega}$, computed for this case are shown in Fig. 4.9. They illustrate that temperatures above 100 eV are necessary to quench the nonconvective instability for $(v_{0\perp}/c) = 0.025$. However, as in the case of collisions, a convective backward wave amplification still remains. At moderate temperatures, the cyclotron damping becomes important only near cyclotron resonance, as shown in Chapter III. With finite beam velocity, the beam/plasma interaction point is generally far below the cyclotron frequency. This is the physical reason why the plasma temperature effect in quenching nonconvective instability is weak.

From the foregoing, we conclude that either a large amount of collisions, or a high electron temperature for the plasma are generally needed to quench the nonconvective whistler instability, and more effective means of stabilization must be sought.

4. Effect of Parallel Velocity Spread in the Beam

Let us superimpose a Maxwellian distribution of parallel velocities on the electron beam, whose transverse velocities are left arbitrary. Then we have

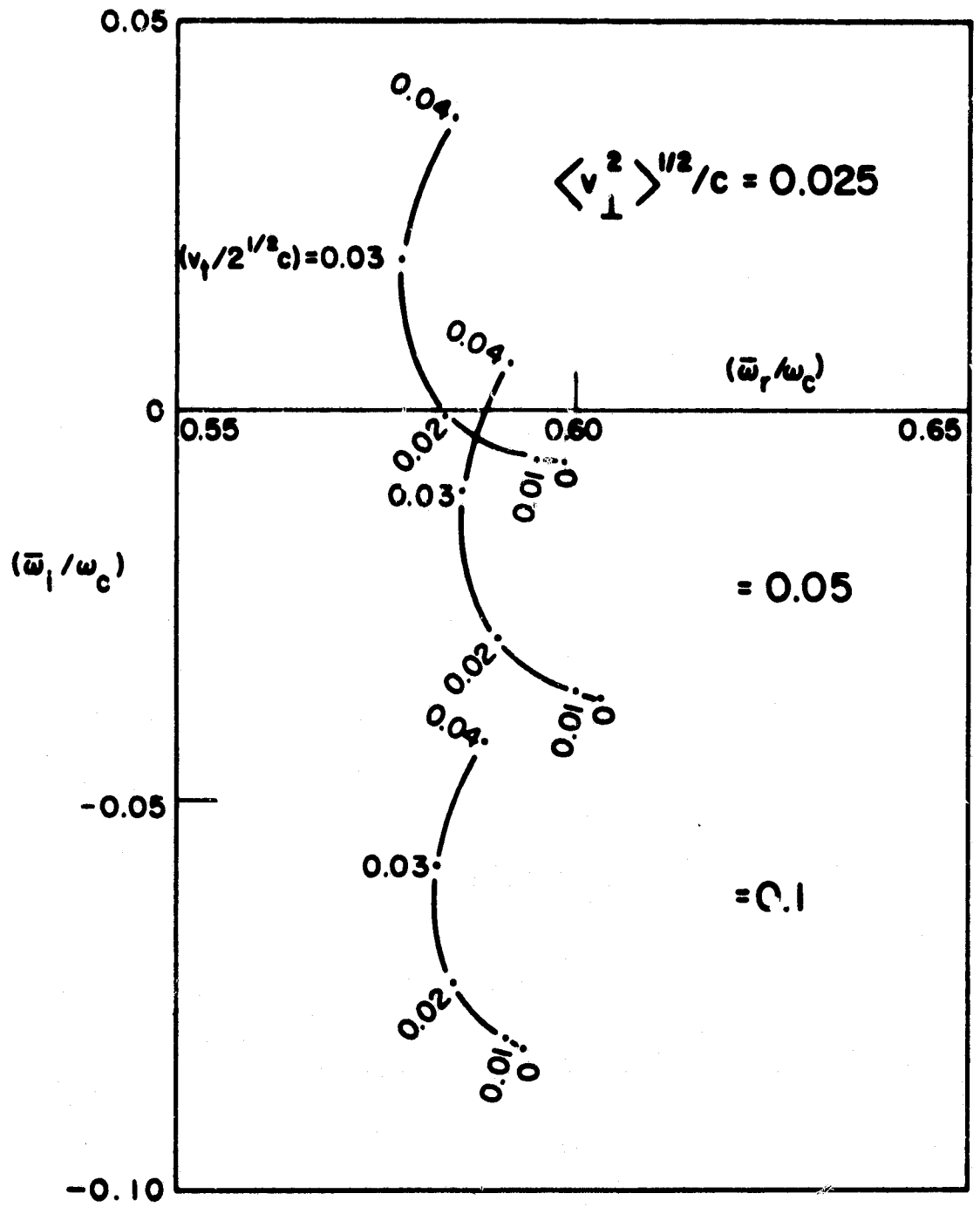

FIG. 4.9. LOCI OF BRANCH POINTS IN THE ω-PLANE AS A FUNCTION OF THE MAXWELLIAN PLASMA TEMPERATURE $[\omega_p^2/\omega_c^2 = 25, \omega_b^2/\omega_c^2 = 1, v_{0\parallel}/c = -0.05]$.

$$f_b(v_{\parallel}, v_{\perp}) = \left(\frac{1}{\pi v_{t\parallel}^2}\right)^{1/2} f_{\perp}(v_{\perp}) \exp -\left[\frac{(v_{\parallel} - v_{0\parallel})^2}{v_{t\parallel}^2}\right] \tag{4.9}$$

where $v_{0\parallel}$ is the drift velocity of the beam; $v_{t\parallel}$ the thermal speed parallel to the static magnetic field, and

$$\langle v_{\perp}^2 \rangle = 2\pi \int_0^{\infty} v_{\perp}^2 f_{\perp}(v_{\perp})\, v_{\perp} dv_{\perp} , \tag{4.10}$$

the mean squared velocity in the perpendicular direction. When this distribution is introduced into Eq. (2.40), and substituted in Eq. (4.3) for the beam, we obtain

$$D(\omega,k) \equiv 1 - \left(\frac{kc}{\omega}\right)^2 - \frac{\omega_p^2}{\omega(\omega - \omega_c)} - \left(\frac{\omega_b}{\omega}\right)^2 \left[1 - \frac{\omega_c}{kv_{t\parallel}} Z(\xi) + \frac{\langle v_{\perp}^2 \rangle}{2v_{t\parallel}^2} Z'(\xi)\right] = 0 , \tag{4.11}$$

where

$$\xi = \frac{(\omega - kv_{0\parallel} - \omega_c)}{kv_{t\parallel}} ,$$

It is clear that the details of the transverse distribution, $f_{\perp}$, in the beam are not important, since only the mean squared velocity, $\langle v_{\perp}^2 \rangle$, enters into the dispersion relation. Physically, this is simply a statement that all of the beam electrons with the same parallel velocity see the same Doppler-shifted frequency $(\omega - kv_{\parallel})$, and can give up their transverse energy in synchronism with the cyclotron frequency. A spread in $v_{\parallel}$ will influence the Doppler-shifted frequency, however, and will produce a drastic effect upon the dispersion characteristics. Figure 4.10 shows indeed that the growth rates of the whistlers, obtained for real k, vary drastically with the parallel velocity spread, $v_{t\parallel}$. For example, a parallel temperature of only 5.2 eV ($v_{t\parallel}/c = 0.0064$) is enough to quench the nonconvective instability due to a beam with a transverse temperature of 64 eV.

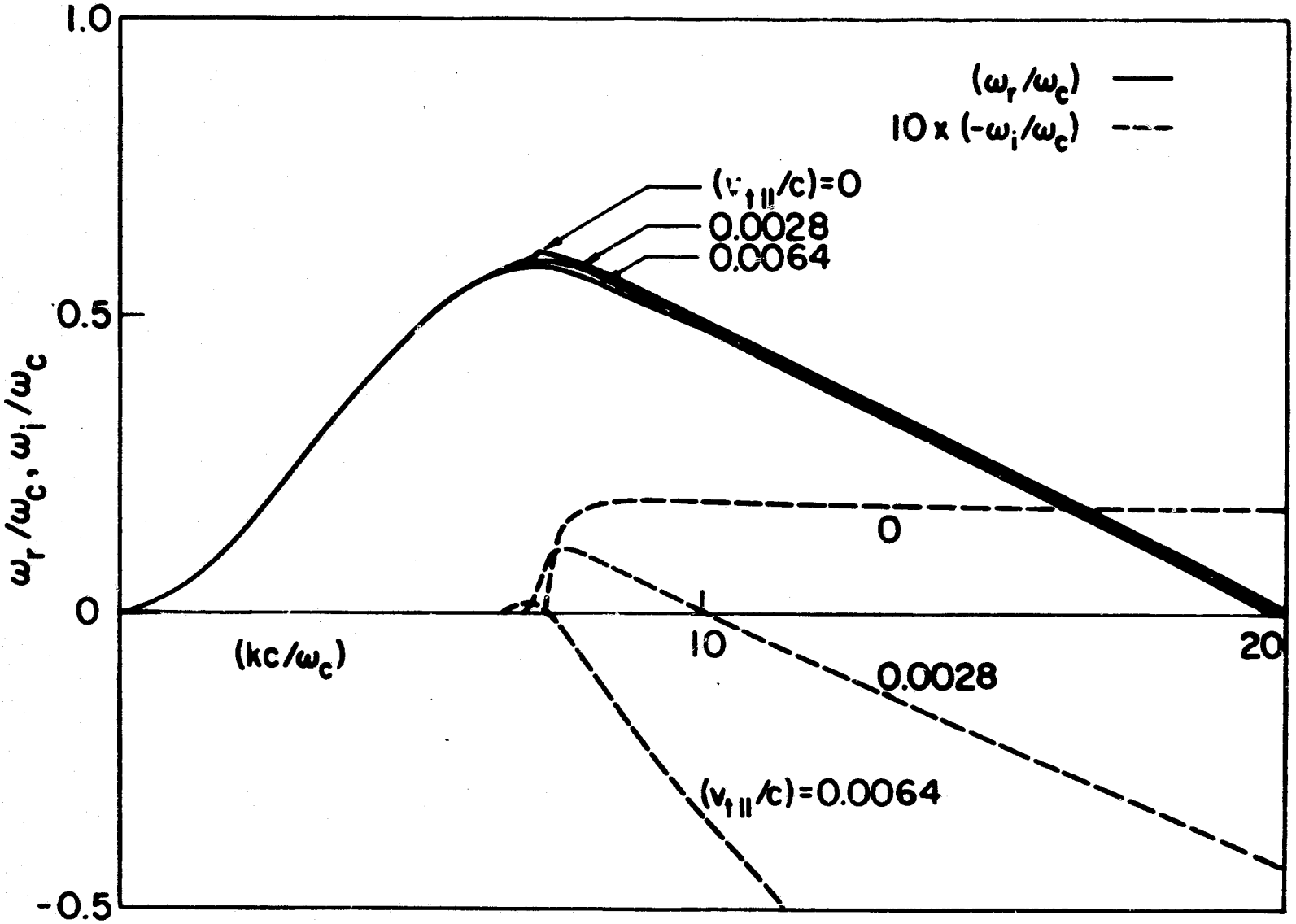

FIG. 4.10. BRILLOUIN DIAGRAM OF COMPLEX ω vs REAL k SHOWING THE EFFECT OF A PARALLEL VELOCITY SPREAD, $v_{t\parallel}$, OF THE BEAM ON WHISTLER INSTABILITY IN A COLD PLASMA $[\omega_p^2/\omega_c^2 = 25, \omega_b^2/\omega_c^2 = 1, v_{0\parallel}/c = -0.05, \langle v_\perp^2\rangle^{1/2}/c = 0.025]$.

It will be observed from Fig. 4.10 that there is a value of k, for any given $(v_{t_\parallel}/c)$, above which the wave is damped and below which the wave is growing. The critical point, $\omega_i = 0$, is the condition for marginal stability. Assume ω and k both real in Eq. (4.11), and separate the real and imaginary parts. This yields

$$\omega - kv_{0\parallel} = \omega_c\left(1 - v_{t_\parallel}^2/\langle v_\perp^2\rangle\right) ,$$

$$1 - \left(\frac{kc}{\omega}\right)^2 - \frac{\omega_p^2}{\omega(\omega_c - \omega)} = \left(\frac{\omega_b}{\omega}\right)^2 \left(1 - \langle v_\perp^2\rangle/v_{t_\parallel}^2\right) . \qquad (4.12)$$

In previous work, Sudan [40] used a normal-mode approach, and obtained relations equivalent to Eq. (4.12). The equation is only cubic in k, and can be solved to determine the critical value at which $\omega_i = 0$.

Finally we show in Fig. 4.11 the locus of branch-points $\bar{\omega}$ for three transverse beam energies. The ratio of $(v_{t_\parallel}^2/\langle v_\perp^2\rangle)$ required for stabilization is approximately 0.04 in all three cases. For thermal energies in excess of this, there is a weak convective instability, which disappears only when $v_\parallel^2/\langle v_\perp^2\rangle \geq 1$.

C. WHISTLER INSTABILITY IN NON-DRIFTING ANISOTROPIC PLASMA

The analysis of the previous section shows that the drift motion of the beam mainly changes the interaction frequency through Doppler shift, and that the drift energy is not used effectively in whistler amplification. Furthermore, the drift motion of the beam may interact very strongly with the plasma via electrostatic modes, such as the well known two-stream instability [50]. If there is no drift motion in the gyrating "beam", there will be no instability of the two-stream type. For this reason, the remaining studies of this chapter will cover non-drifting plasmas. We will consider first the simple ring and pancake distributions, next the anisotropic resonance distribution, then an anisotropic Maxwellian distribution, and finally a loss-cone distribution.

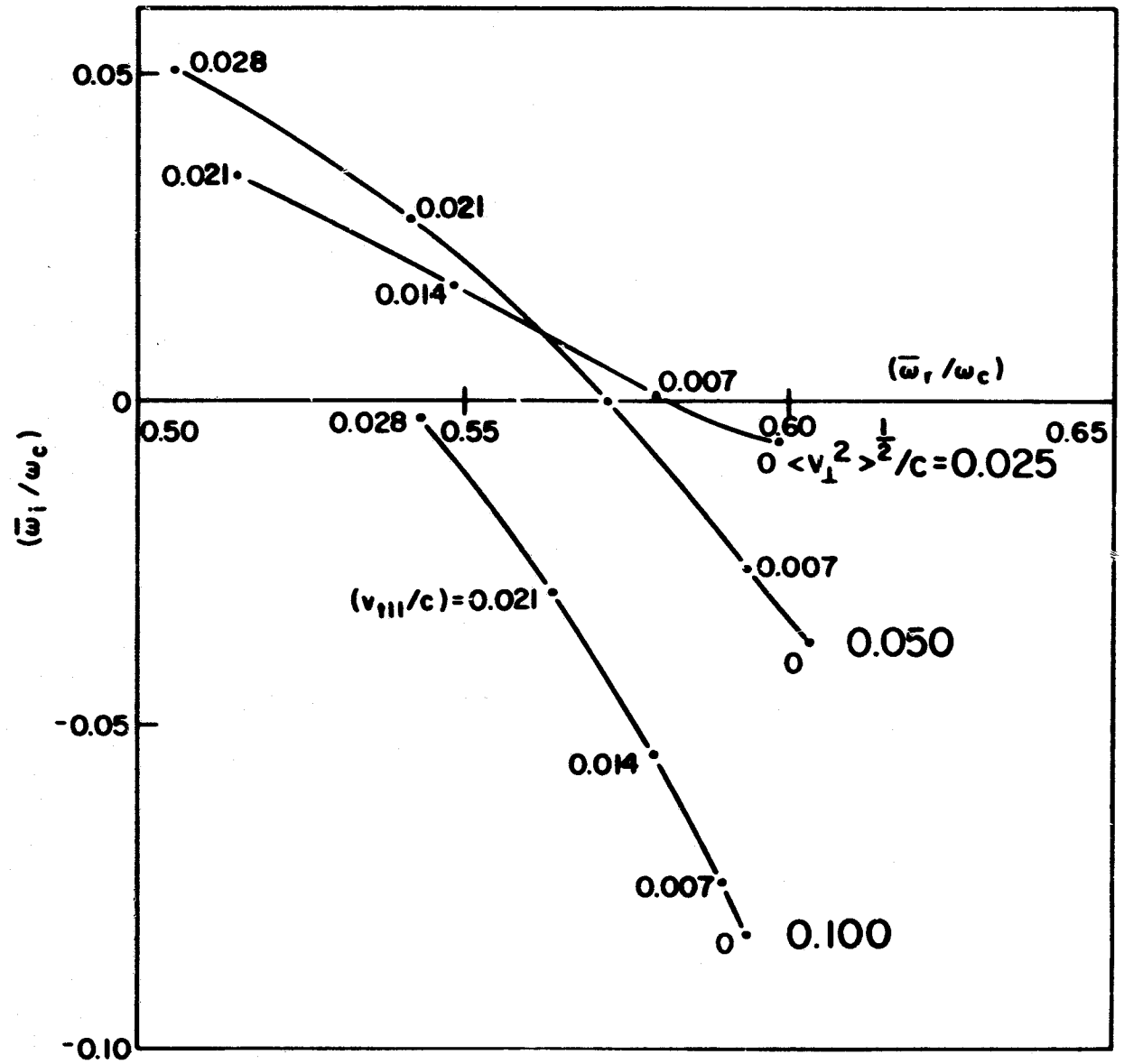

FIG. 4.11. LOCI OF BRANCH POINTS AS A FUNCTION OF PARALLEL BEAM VELOCITY SPREAD, $v_{t\parallel}$ $[\omega_p^2/\omega_c^2 = 25,\ \omega_b^2/\omega_c^2 = 1,\ v_{0\parallel}/c = -0.05]$.

1. Ring or Pancake Distribution

The simplest anisotropic distribution is the ring distribution, in which all particles have the same transverse energy. If the energetic electron group, of plasma frequency ω_b, is assumed to have a ring distribution, and the background plasma, of plasma frequency ω_p, is assumed cold, the dispersion relation can be obtained from Eq. (4.3) simply by putting $v_{0\parallel} = 0$. We obtain

$$1 - \left(\frac{kc}{\omega}\right)^2 - \frac{\omega_p^2 + \omega_b^2}{\omega(\omega - \omega_c)} - \frac{\omega_b^2}{\omega^2} \frac{v_{0\perp}^2 k^2}{2(\omega - \omega_c)^2} = 0 \ . \tag{4.13}$$

This dispersion relation is also valid for a pancake distribution of the type

$$f_b = f_\perp(v_\perp)\ \delta(v_\parallel) \ , \tag{4.14}$$

where $f_\perp$ is arbitrary, provided we replace $v_{0\perp}^2$ in Eq. (4.13) by

$$\langle v_\perp^2 \rangle = 2\pi \int_0^\infty v_\perp^2 f_\perp(v_\perp)\ v_\perp dv_\perp \ . \tag{4.15}$$

Equation (4.13) is quadratic in k, quartic in ω, and can be solved in the form

$$k^2 c^2 = \frac{\omega(\omega - \omega_c)(\omega^2 - \omega\omega_c - \omega_p^2 - \omega_b^2)}{(\omega - \omega_c)^2 + \frac{1}{2}(\omega_b v_{0\perp}/c)^2} \ . \tag{4.16}$$

Note that the transverse energy, $v_{0\perp} \neq 0$, introduces one more mode, but does not change the cutoff frequencies of the fast wave modes. Under the condition $\omega_p \gg \omega_c > \omega$, which is typical for experiments in the magnetosphere and in laboratory plasmas, one can neglect the unit term in Eq. (4.13) and solve for the whistler frequency

$$\frac{\omega}{\omega_c} = \frac{\left(\omega_p^2 + \omega_b^2 + 2\,k^2c^2\right) \pm cv_{0\perp}(\omega_b/\omega_c)\left[2\left(k_+^2 - k^2\right)\left(k^2 - k_-^2\right)\right]^{1/2}}{2\left(\omega_p^2 + \omega_p^2 + k^2c^2\right)} \quad , \tag{4.17}$$

where

$$k_\pm^2 = \left[(\omega_p/c)^2 + (\omega_b/c)^2\right]\left\{1 \pm \left[1 + 2(c\omega_c/v_{0\perp}\omega_b)^2\right]^{1/2}\right\} \cdot \tag{4.18}$$

Clearly this wave is unstable when $|k| > k_+$, i.e., when

$$|\omega| > \omega_+ = \omega_c - \omega_c\left[1 + 2^{1/2}(c\omega_c/v_{0\perp})\right]^{-1} \cdot \tag{4.19}$$

Note that ω_+ is independent of the plasma density, ω_p^2, and approaches ω_c or $\omega_c/2$ as $(v_{0\perp}\omega_b/c\omega_c)$ tends to zero or infinity, respectively. These characteristics are shown in Fig. 4.12.

To determine the instability character, we first locate the saddle points $(d\omega/dk) = 0$ of Eq. (4.13) at

$$\bar{\omega} = \omega_c \pm i\omega_b(v_{0\perp}/c)\,2^{-1/2} \quad , \quad \bar{k} = \infty \quad . \tag{4.20}$$

When we map the real k-axis into the frequency plane via Eq. (4.13), we find that it traces through cusps centered at the frequencies $\bar{\omega}$, as shown in Fig. 4.13. Since one of these branch points is in the lower half frequency plane $(\bar{\omega}_i < 0)$, it follows from the frequency cusp criterion (Section A2) that this system is nonconvectively unstable. The presence of the ring distribution would therefore drive the plasma into strong oscillation at $\bar{\omega}$, near the cyclotron frequency. This can be prevented by a small parallel velocity spread superimposed on the ring distribution. This can be seen readily by introducing for the "beam" a resonance shaped parallel velocity spread of the form

$$f_b(v_\parallel, v_\perp) = f_\perp(v_\perp)\,\frac{v_{r\parallel}}{\pi\left(v_\parallel^2 + v_{r\parallel}^2\right)} \cdot \tag{4.21}$$

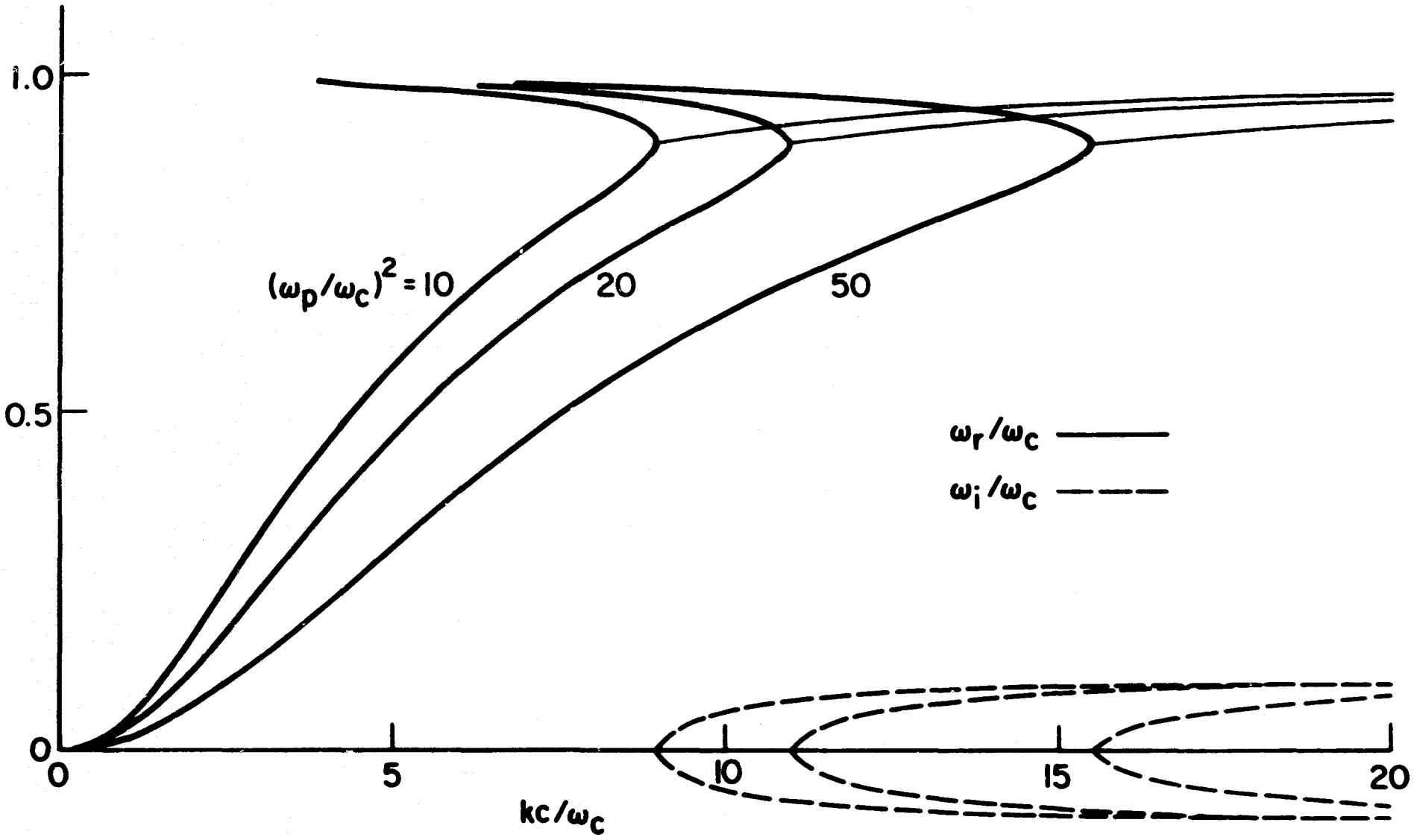

FIG. 4.12. BRILLOUIN DIAGRAM OF COMPLEX ω VS. REAL k, ILLUSTRATING THE INTERACTION OF A RING DISTRIBUTION OF ENERGETIC ELECTRONS WITH A COLD PLASMA $[\omega_b^2/\omega_c^2 = 10,\ v_{0\perp}/c = 0.05]$.

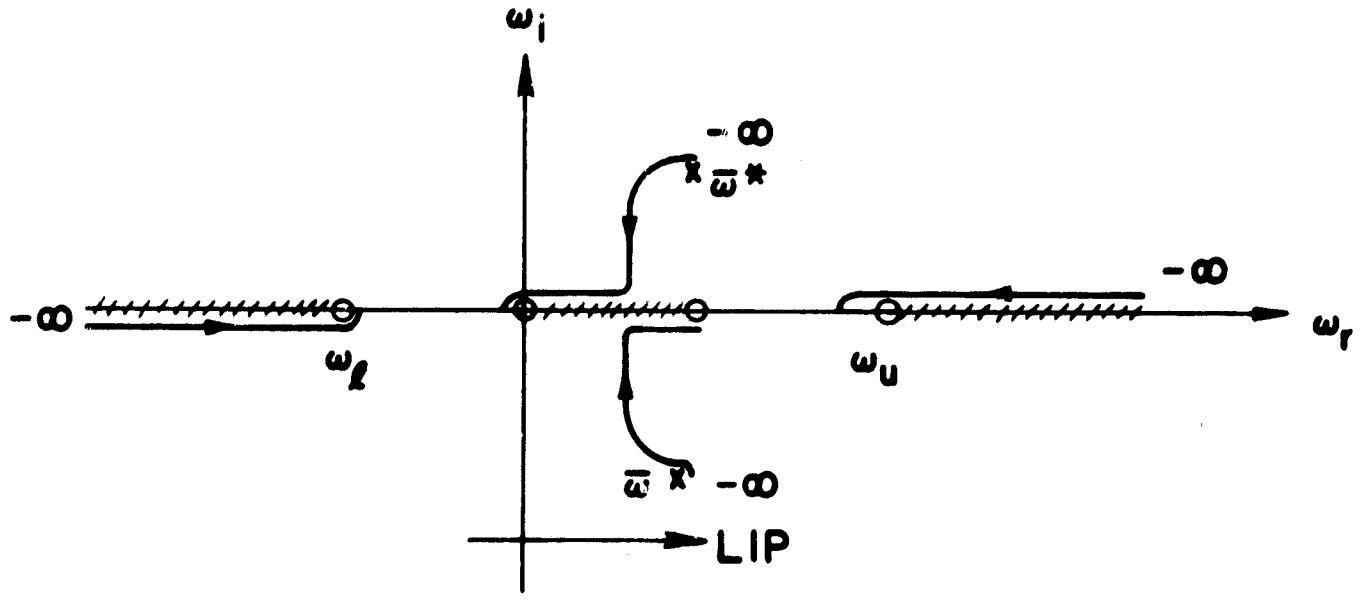

FIG. 4.13. CONTOUR MAP OF REAL k ($k_i \rightarrow 0_-$) MAPPED INTO THE FREQUENCY PLANE VIA EQ. (4.13).

This change in distribution has the effect of replacing ω by $(\omega - ikv_{r_\parallel})$ in the contribution of the "beam" to Eq. (4.13). From the analyses of Section IVB, we know that the whistler instability is largely due to the "beam" alone. To estimate the effect of the velocity spread we will omit the plasma $(\omega_p = 0)$, and drop, for $\omega_p \gg \omega_c > \omega$, the unit term to get

$$\left(\frac{kc}{\omega}\right)^2 + \left(\frac{\omega_b}{\omega}\right)^2 \left[\frac{\omega - ikv_{r_\parallel}}{\omega_c - \omega + ikv_{r_\parallel}} + \frac{k^2\langle v_\perp^2\rangle}{2(\omega_c - \omega + ikv_{r_\parallel})^2}\right] = 0 \ . \qquad (4.22)$$

The solution of Eq. (4.23) for real k can be obtained from the corresponding solution of Eq. (4.13) by the imaginary Doppler shift, $\omega - ikv_{r_\parallel} = \omega'(k)$. In this process, the real part of ω is unchanged and the imaginary part of ω is shifted linearly with k. The results displayed in Fig. 4.14 clearly show that the longitudinal temperature effectively quenches the instability at short wavelengths (k large).

2. Simple Anisotropic Resonance Distribution

For a general anisotropic distribution function, the dispersion relation $[D(\omega,k) = 0]$ is in general transcendental, with infinitely many branch $(\bar{\omega}_n)$ and saddle points $(\bar{k}_n)$. According to Derfler [72], only a few of these saddle points have a physical meaning in as far as they represent true resonances, $\exp i(\bar{\omega}t - \bar{k}z)$, of the plasma. On this basis, one can expect that a simple distribution function, yielding a low order rational dispersion function, would at least qualitatively describe the physical picture. As such, we choose the anisotropic resonance distribution,

$$f_b(v_\parallel, v_\perp) = \frac{1}{\pi^2 \alpha_r} \frac{v_r}{\left(v_\parallel^2 + \frac{1}{\alpha_r} v_\perp^2 + v_r^2\right)^2} \ , \qquad (4.23)$$

where v_r is the thermal velocity, and α_r, is a distribution anisotropy factor. When we include a cold plasma background, the whistler dispersion relation becomes

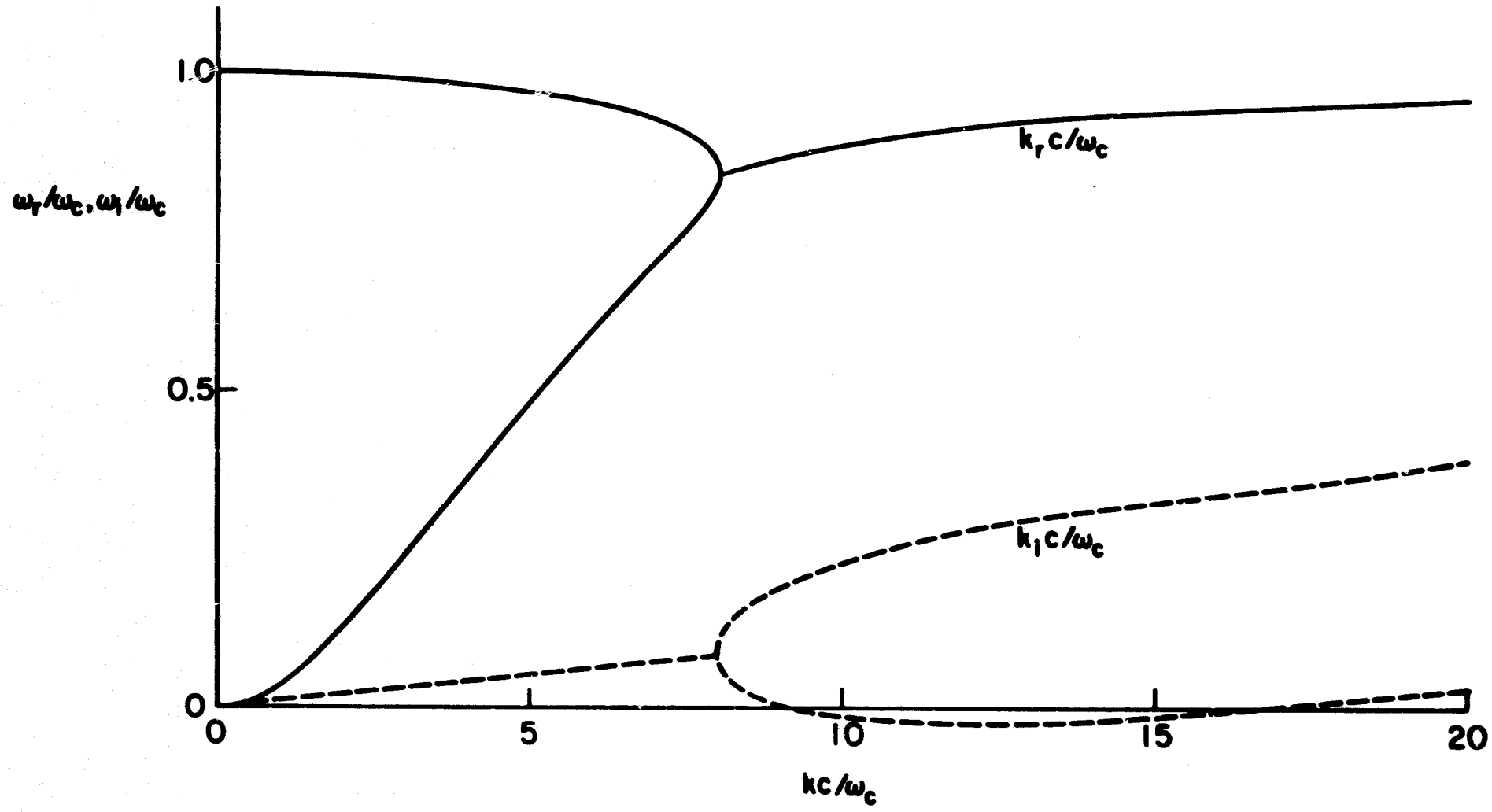

FIG. 4.14. BRILLOUIN DIAGRAM OF COMPLEX ω vs. REAL k, ILLUSTRATING THE QUENCHING OF INSTABILITY FOR A PANCAKE DISTRIBUTION BY A RESONANCE SHAPED PARALLEL VELOCITY SPREAD.

$$D(\omega,k) = 1 - \left(\frac{kc}{\omega}\right)^2 + \frac{\omega_p^2}{\omega(\omega_c - \omega)} + \left(\frac{\omega_b}{\omega}\right)^2 \frac{\omega + ikv_r(\alpha_r - 1)}{\omega_c - \omega + ikv_r} = 0 \ . \tag{4.24}$$

Note that the terms ikv_r and ω, having opposite sign, will always contribute to cyclotron damping, while the term $ikv_r(\alpha_r - 1)$ in the numerator may contribute to instability or damping, depending on the sign of $(\alpha_r - 1)$. The frequency of marginal stability is found to be

$$\omega_m/\omega_c = 1 - \alpha_r^{-1}, \quad \alpha_r > 1 \ . \tag{4.25}$$

For $\omega > \omega_m$, the wave is cyclotron damped. For $\omega < \omega_m$, there is instability due to cyclotron resonance interaction. To determine the instability character, we first look for the branch points, $\bar{\omega}$, which are solutions of the simultaneous equations $D = 0$ and $\partial D/\partial k = 0$. When k is eliminated, we obtain the algebraic equation valid for $\omega_p = 0$, i.e., the hot electron group alone,

$$a_0\Omega^6 + a_1\Omega^5 + a_2\Omega^4 + a_3\Omega^3 + a_4\Omega^2 + a_5\Omega + a_6 = 0 \tag{4.26}$$

where

$$a_0 = 4(1 + \beta^2)^2 \ , \quad a_1 = -16(1 + \beta^2) \ ,$$

$$a_2 = 4\left[3\Omega_b^2\beta^4 + 2\beta^2 - (9 + 5Q)\ \Omega_b^2\beta^2 + 6 - \Omega_b^2\right] \ ,$$

$$a_3 = 4\left[(10Q + 9)\ \Omega_b^2\beta^2 + 3\Omega_b^2 - 4\right] \ ,$$

$$a_4 = 12\Omega_b^4Q^2\beta^4 - \beta^2\Omega_b^2\left[20Q + \Omega_b^2Q^2 - 27\Omega_b^2 - 18Q\Omega_b^2\right] + 4 - 12\Omega_b^2 \ ,$$

$$a_5 = 2\Omega_b^2\left[\Omega_b^2Q\beta^2(9 - Q) - 2\right] \ , \quad a_6 = \Omega_b^2Q^2\beta^2\left(4\Omega_b^2Q\beta^2 - 1\right) \ ,$$

$$\Omega = \omega/\omega_c \ , \quad Q = \alpha_r - 1 \ , \quad \beta = v_r/c \ , \quad K = kc/\omega_c \ .$$

For $\Omega_b^2 = 25$, $Q = 10$ and $\beta = 0.04$, the following six branch and saddle points are found

$$\bar{\Omega}_1 = 0.411 - i0.167 \quad , \quad \bar{K}_1 = 2.147 + i4.281 \ ,$$

$$\bar{\Omega}_2 = 0.411 + i0.167 \quad , \quad \bar{K}_2 = -2.147 + i4.281 \ ,$$

$$\bar{\Omega}_3 = 0.426 \quad , \quad \bar{K}_3 = i12.868 \ ,$$

$$\bar{\Omega}_4 = 1.747 \quad , \quad \bar{K}_4 = -i21.222 \ ,$$

$$\bar{\Omega}_5 = 5.555 \ , \quad \bar{K}_5 = -i0.612 \ ,$$

$$\bar{\Omega}_6 = -4.553 \ , \quad \bar{K}_6 = +i0.483 \ .$$

Here $(\bar{\Omega}_5, \bar{K}_5)$ and $(\bar{\Omega}_6, \bar{K}_6)$ correspond to the cutoff frequencies of the right- and left-hand polarized fast waves, respectively. The physical meaning of the other branch points is not so obvious and must be determined by a process of analytical continuation towards real frequencies from below, as shown in Fig. 4.15. Here we see that the saddle point $\bar{k}_1$ arises from a collision of two Landau poles, k_1 and k_2, across the positive real axis, and hence the corresponding branch point, $\bar{\Omega}_1$, represents a nonconvectively unstable resonance. It has not been determined whether the remaining branch points are ignorable [72], or represent true resonances of the system. In this case, these resonances would be evanescent and, hence, of no importance due to the presence of the nonconvective instability.

By decreasing the distribution anisotropy factor, α_r, or the density of the hot electrons, Ω_b^2, or by increasing the density of the cold plasma, we can reduce the temporal growth rate, $\bar{\Omega}_{1i}$. For example, when α_r is reduced to 10, or by introducing a cold plasma with density $(\omega_p/\omega_c)^2$ greater than 8, one can make $\bar{\Omega}_{1i} > 0$, and cure the nonconvective instability. Only then does it make sense to solve the dispersion relation for real ω to find the spatial growth rates, k_i, of the now convective instability, as shown in Figs. 4.16 and 4.17.

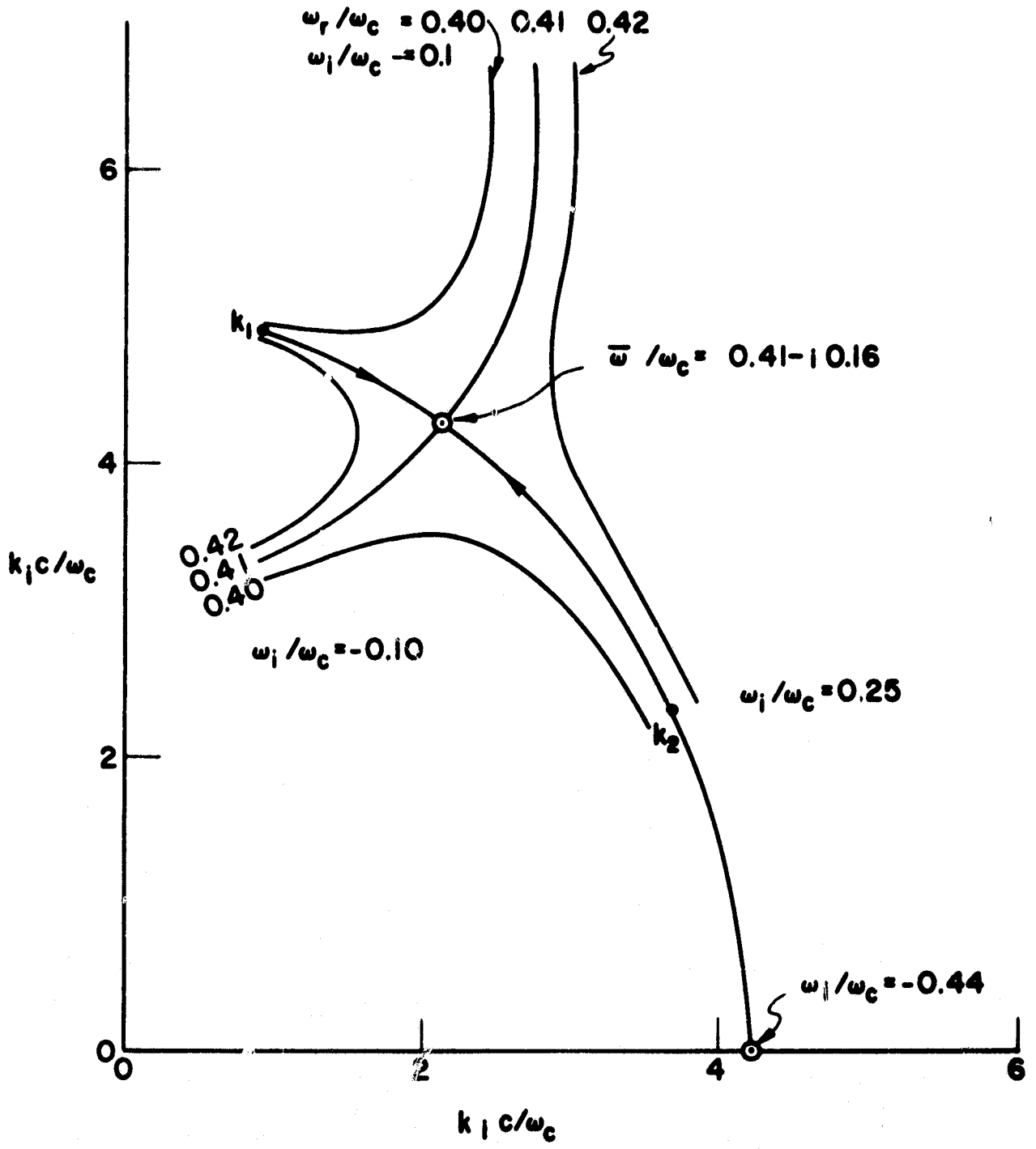

FIG. 4.15. CONTOUR MAP OF ORDINATES ω_r = const MAPPED FROM THE ω-PLANE INTO THE k-PLANE VIA EQ. (4.22) [$\omega_p^2/\omega_c^2 = 0$, $\omega_b^2/\omega_c^2 = 25$, $v_r/c = 0.04$, $\alpha_r = 11$].

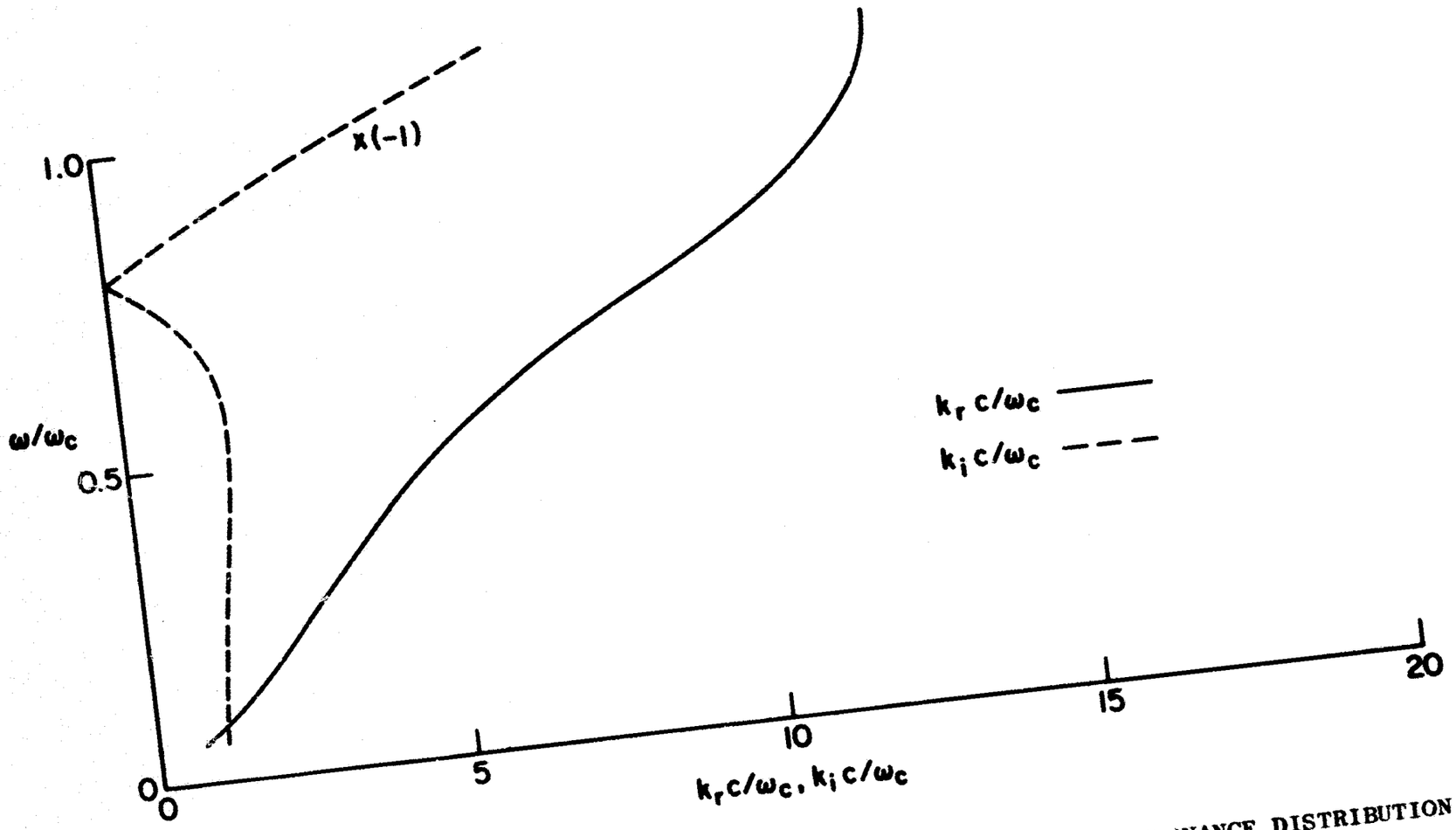

FIG. 4.16. BRILLOUIN DIAGRAM OF REAL ω vs. COMPLEX k FOR ANISOTROPIC RESONANCE DISTRIBUTION [$\omega_p^2/\omega_c^2 = 0$, $\omega_b^2/\omega_c^2 = 25$, $v_r/c = 0.04$, $\alpha_r = 5$].

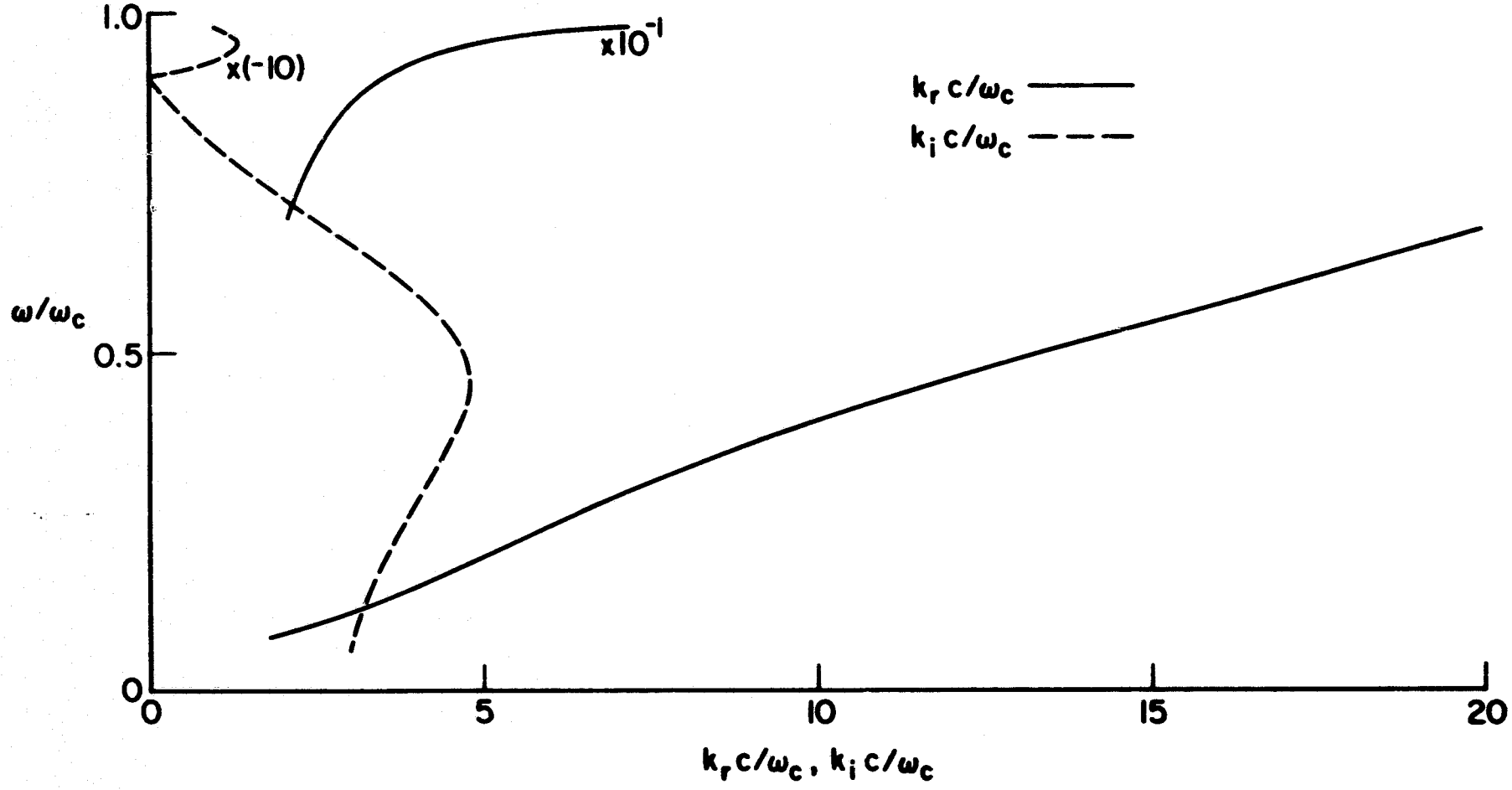

FIG. 4.17. BRILLOUIN DIAGRAM OF REAL ω vs. COMPLEX k FOR ANISOTROPIC RESONANCE DISTRIBUTION [$\omega_p^2/\omega_c^2 = 100$, $\omega_b^2/\omega_c^2 = 25$, $v_r/c = 0.04$, $\alpha_r = 11$].

Finally, we note that for a pitch angle distribution of the type considered by Liemohn [46]

$$f_b = \frac{2}{\pi^2} \frac{v_q v_\perp^2}{\left(v_\perp^2 + v_{||}^2 + v_q^2\right)^2} , \tag{4.27}$$

the dispersion relation is given by

$$1 - \left(\frac{kc}{\omega}\right)^2 + \frac{\omega_p^2}{\omega(\omega_c - \omega)} + \left(\frac{\omega_b}{\omega}\right)^2 \frac{\omega + ikv_q}{\omega_c - \omega + ikv_q} = 0 \cdot \tag{4.28}$$

By making $\alpha_r = 2$ and $v_q = v_r$, we see that Eq. (4.28) is identical to Eq. (4.24). Thus, the electron distribution function can not be uniquely identified from the whistler dispersion relation alone. The integration in velocity space effectively smoothes out details of the original distribution. Liemohn suggested that the whistler instability for this kind of velocity distribution should always be convective. However, with $\omega_p^2 \gg \omega_b^2$ and $\omega_b^2 v_q^2/\omega_c^2 c^2 \geq 0.23$, we find that it is nonconvectively unstable. A procedure to find the boundary between a convectively and nonconvectively unstable system, i.e., $\bar{\omega}_i = 0$, will be discussed in the next section for the more important case of a Maxwellian distribution with temperature anisotropy.†

3. Anisotropic Maxwellian Distribution

When the drift velocity, $v_{0||}$, of the electron beam in Eq. (4.8) is set to zero, and $Z'\,[= -2(1 + \xi Z)]$ eliminated, we obtain the right-hand polarized wave dispersion relation

$$D(\omega,k) = 1 - \left(\frac{kc}{\omega}\right)^2 + \frac{\omega_p^2}{\omega(\omega_c - \omega)} + \left(\frac{\omega_b}{\omega}\right)^2 \left\{\frac{\omega}{kv_{t||}} Z(\xi) + (\alpha-1)\left[1 + \xi Z(\xi)\right]\right\} = 0 , \tag{4.29}$$

† For an application of this procedure to the anisotropic resonance distribution, compare Appendix B.

where $\alpha = \langle v_\perp^2 \rangle / v_{t\|}^2 = T_\perp / T_\|$ is the temperature anisotropy factor, and $\xi = (\omega - \omega_c)/kv_{t\|}$. At the point of marginal stability ω, k and ξ are real. For real ξ, $Z(\xi)$ is always complex. Hence the factor multiplying Z, and the remainder in Eq. (4.29), must vanish separately. This gives the location of the point of marginal stability:

$$\omega_m = \frac{\alpha - 1}{\alpha}\,\omega_c, \quad \alpha > 1 ,$$

$$k_m^2 c^2 = (\alpha - 1)\left[\frac{(\alpha - 1)}{\alpha^2}\,\omega_c^2 + \omega_p^2 + \omega_b^2\right] . \tag{4.30}$$

Note that ω_m depends only on the temperature anisotropy of the hot electron population, while k_m depends also on the density of the cold plasma background. Previous authors neglected the effect of the cold plasma [40,47]. In Fig. 4.18, we demonstrate this shift of the point of marginal stability due to a change in temperature anisotropy. From this plot of complex ω versus real k, no conclusion whatsoever can be drawn as to the character of the instability for $k < k_m$. However, a plot of real ω versus complex k for the same parameters, in Fig. 4.19, shows a drastic change in dispersion. The reversal of the "group velocity" $(d\omega/dk_r)$ at high frequencies, $\omega/\omega_c > 0.65$, as the temperature anisotropy is increased from $\alpha = 2$ to 6.25, suggests a change in the instability character. However this argument is fallacious because, in the presence of nonconvective instabilities, it does not make sense to consider real frequencies. If, instead, we map ordinates $\omega_r = \text{const}$ from the lower ω-plane into the k-plane (Fig. 4.20), we locate a saddle point, $\bar{k}$, and find the corresponding branch point, $\bar{\omega}$. Since $\bar{\omega}_i < 0$ for $\alpha = 6.25$, this application of the colliding pole criterion (Section A2) confirms indeed that the instability character has changed from convective to nonconvective when α is increased from 2 to 6.25.

In the following, we will investigate when this instability goes from convective to nonconvective, i.e., we propose to find a relation between the parameters of Eq. (4.29) so that the branch point $\bar{\omega}$ is strictly real. For this purpose, we cast the dispersion relation Eq. (4.29) into the form

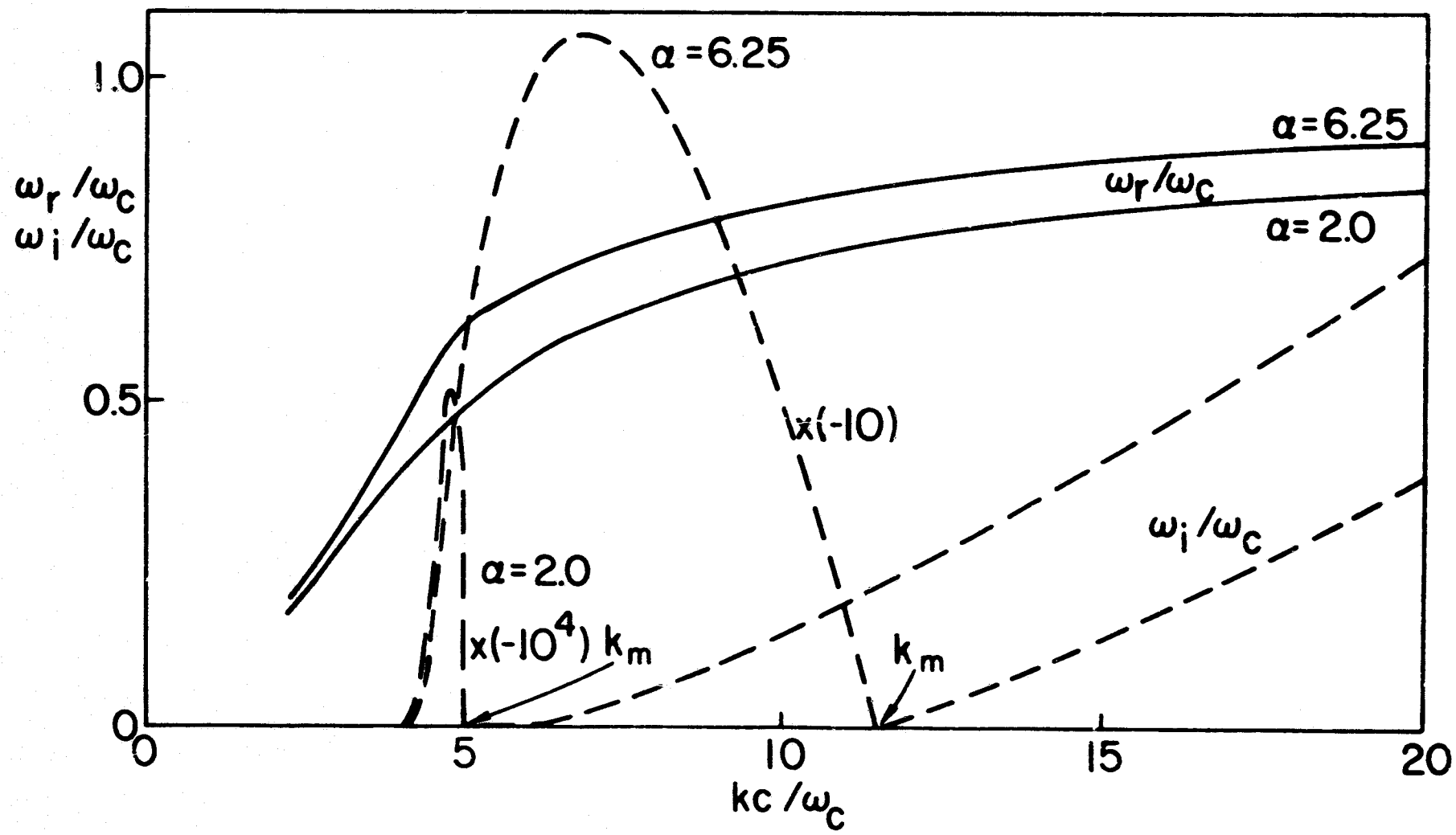

FIG. 4.18. BRILLOUIN DIAGRAM OF COMPLEX ω vs. REAL k FOR MAXWELLIAN DISTRIBUTION $[\omega_p^2/\omega_c^2 = 0,$ $\omega_b^2/\omega_c^2 = 25,$ $v_{t_\parallel}/c = 0.04]$.

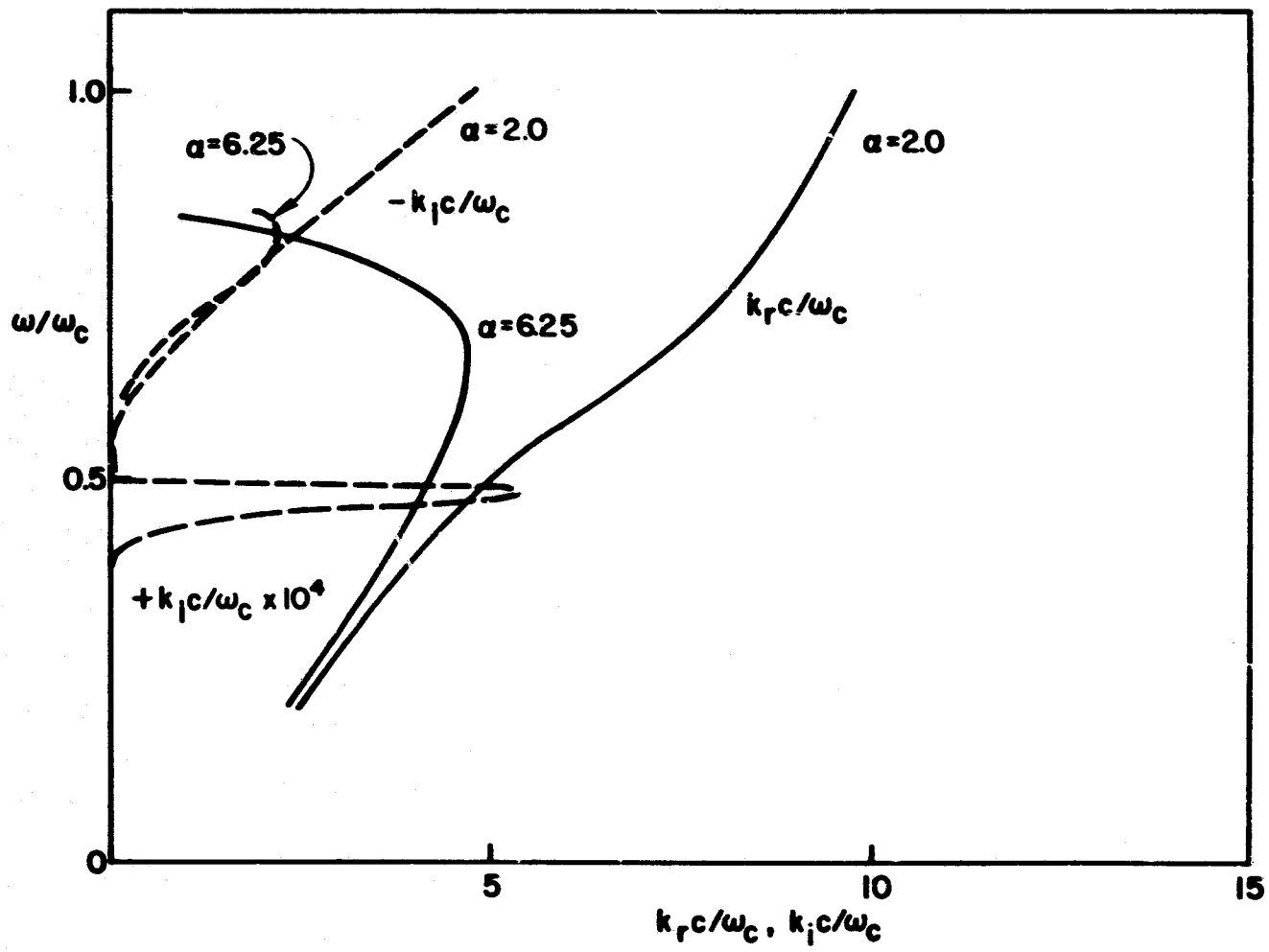

FIG. 4.19. BRILLOUIN DIAGRAM OF REAL ω vs. COMPLEX k FOR MAXWELLIAN DISTRIBUTION $[\omega_p^2/\omega_c^2 = 0,\ \omega_b^2/\omega_c^2 = 25,\ v_{tl}/c = 0.04]$.

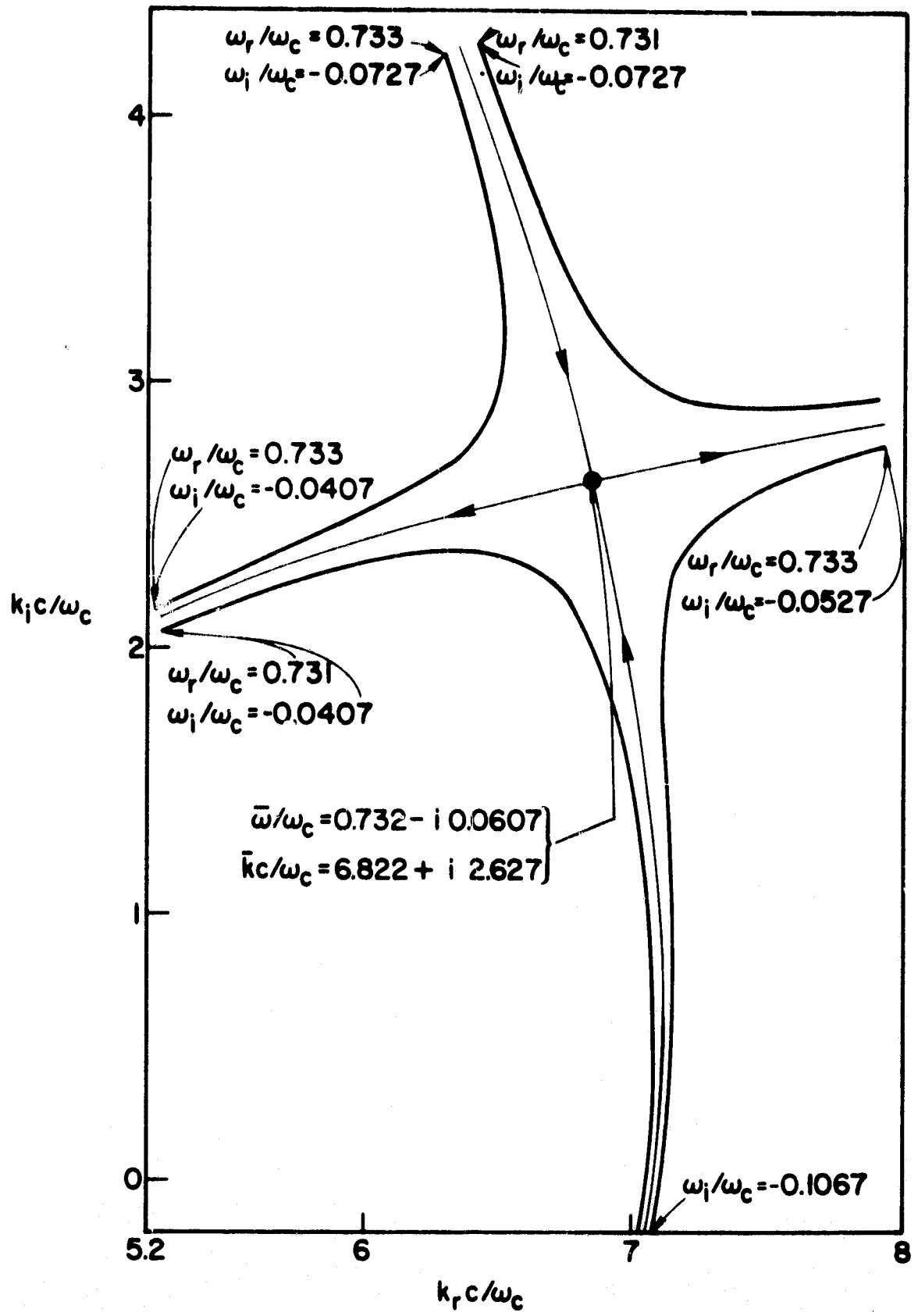

FIG. 4.20. CONTOUR MAP OF ORDINATES ω_r = const MAPPED FROM THE ω-PLANE INTO THE k-PLANE VIA EQ. (4.27) [$\omega_p^2/\omega_c^2 = 0$, $\omega_b^2/\omega_c^2 = 25$, $v_{t_{||}}/c = 0.04$, $\alpha = 6.25$].

$$f \equiv \xi^3 Z(\xi) + g\xi^2 - h = 0 \ , \tag{4.31}$$

where

$$\xi = \frac{\omega - \omega_c}{k v_{t\parallel}} \ , \tag{4.32a}$$

$$g = \left[1 - \frac{\omega_p^2}{\omega(\omega - \omega_c)} + (\alpha - 1)\frac{\omega_b^2}{\omega^2}\right]\left[\frac{\omega_b^2}{\omega(\omega - \omega_c)} + (\alpha - 1)\frac{\omega_b^2}{\omega^2}\right]^{-1} , \tag{4.32b}$$

$$h = \left(\frac{c}{v_{t\parallel}}\right)^2 \left(\frac{\omega - \omega_c}{\omega}\right)^2 \left[\frac{\omega_b^2}{\omega(\omega - \omega_c)} + (\alpha - 1)\frac{\omega_b^2}{\omega^2}\right]^{-1} . \tag{4.32c}$$

Branch points are found from the simultaneous equations $f = 0$ and $\partial f/\partial k = -(\xi/k)\,\partial f/\partial \xi = 0$, i.e.,

$$\xi^2 Z' + 3\xi Z + 2g = 0 \ . \tag{4.33}$$

Equation (4.33) can be inverted by means of a digital computer and has infinitely many complex solutions, $\xi = \xi_n(g)$. By specifying that $\bar{\omega}$ be strictly real, g and h are real, but ξ_n will be, in general, complex. We obtain another equation for g by taking the imaginary part of Eq. (4.31), i.e.,

$$\mathrm{Im} f = \mathrm{Im}\left\{\xi_n^3(g)\, Z[\xi_n(g)] + g\xi_n^2(g)\right\} = 0. \tag{4.34}$$

The lowest order solution of this equation has been obtained by Iiyoshi et al [51] in relation to the limitation of ion cyclotron heating when the cold plasma and electron motion are negligible. From Eq. (4.35), g is found to be 2.81, which in turn determines $\xi_1 = -1.045 + 0.414i$ and, by Eq. (4.31), $h_1 = 1.94$. By substituting these values into Eqs. (4.32), we have found three relations for six parameters. These may be reduced as follows.

When ω_p/ω_c, ω_b/ω_c and α are given, Eq. (4.32b) is a cubic equation in ω/ω_c with real coefficients. It necessarily has a real solution $\bar{\omega}/\omega_c$. When this branch point is substituted into Eq. (4.32b) we find the parallel thermal velocity, $v_{t\parallel}/c$, and then, from Eq. (4.32a), the complex saddle point, $\bar{k}c/\omega_c$. If we eliminate $\bar{\omega}/\omega_c$, we obtain a relation between four parameters,

$$S(\omega_p/\omega_c,\ \omega_b/\omega_c,\ T_\perp/T_\parallel,\ v_{t\parallel}/c) = 0 \ . \tag{4.35}$$

This defines an instability boundary since a variation of any one of these parameters will lead from a convectively unstable to a nonconvectively unstable situation, or vice versa. Cross-sections of this instability boundary for $(\omega_p/\omega_c)^2 = 0$, and $(\omega_b/\omega_c)^2$ varying are shown in Fig. 4.21. Note that in the calculation relativistic effects are neglected. The curves in the figures are dashed when relativistic effects become important. From these figures, it is clear that whistler instability can be convective or nonconvective depending on parameters. For the case discussed in Figs. 4.18 and 4.19, we find from Fig. 4.21 that the critical temperature anisotropy for $\omega_p/\omega_c = 0$, $\omega_b/\omega_c = 5$, and $v_{t\parallel}/c = 0.04$ is given by $\alpha = 4.5$. As another example of this kind we take the data of Scharer and Trivelpiece [47], $\omega_p/\omega_c = 0$, $\omega_b/\omega_c = 0.5$, $\alpha = 9$ and find a critical value of $v_{t\parallel}/c = 0.13$ which is smaller than the value $v_{t\parallel}/c = 0.3$ used in the publication. From that, we conclude that the system they analyzed is nonconvectively unstable.

When the condition $\omega_p \gg \omega_c > \omega$ is satisfied, one can neglect the unit term in Eq. (4.32b), which is then linear in ω/ω_c, and has the solution

$$\bar{\omega}/\omega_c = (\alpha - 1)(g - 1)[1 - \alpha + \alpha g + (\omega_p/\omega_b)^2]^{-1} \ . \tag{4.36}$$

When this branch point is substituted into Eq. (4.32c), one obtains $(v_{t\parallel}/c)(\omega_b/\omega_c)$ and, hence, a three dimensional instability boundary

$$S\left(\frac{\omega_p}{\omega_b},\ \frac{v_{t\parallel}}{c},\ \frac{\omega_b}{\omega_c},\ \alpha\right) = 0 \ . \tag{4.37}$$

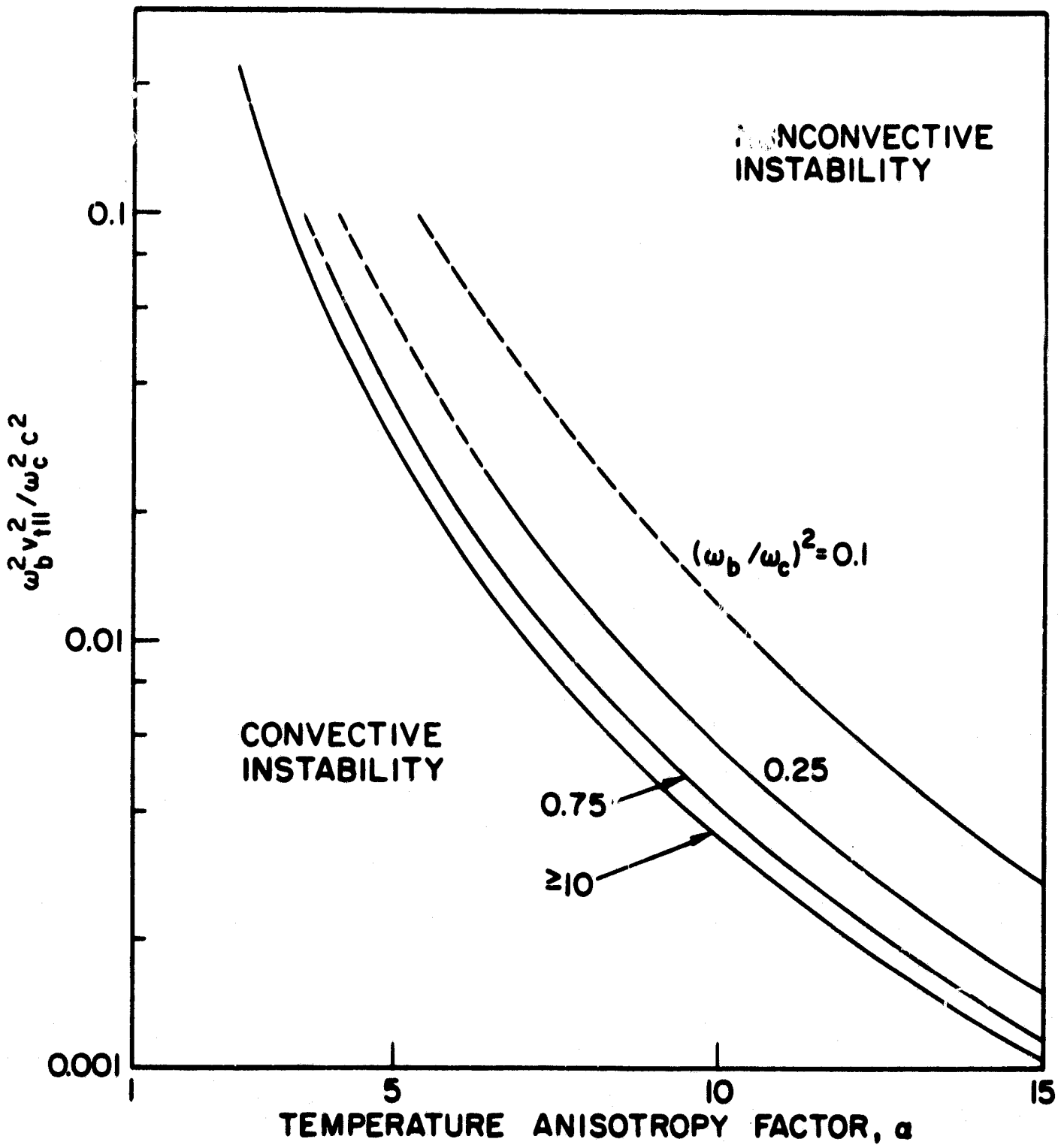

FIG. 4.21. CROSS-SECTIONS OF THE WHISTLER INSTABILITY BOUNDARY, EQ. (4.33) [$\omega_p^2/\omega_c^2 = 0$].

A few cross-sections of this surface, and their corresponding branch points for ω_p/ω_b = const, are shown in Figs. 4.22 and 4.23. By means of these graphs, it is clear that in general the instability boundary depends on parameters of both the cold plasma and hot electron group. In the magnetosphere, if $\omega_p/\omega_b \gg 10$ the instability surface is seen to depend almost on the hot electron group alone. For example, for $\alpha = 10$, if $\omega_b^2 v_{t\parallel}^2/\omega_c^2 c^2 > 0.058$ nonconvective instability will occur. Nonconvective instability may be responsible for hiss-type VLF emissions. Under "quiescent" conditions, if the hot electron group transverse energy or density is reduced below the instability surface, convective amplification is possible. It then makes sense to plot the conventional Brillouin diagram of real ω versus complex k, as shown in Fig. 4.24.

In a seemingly different area, Iiyoshi et al [51] explained the limitation found in the ion cyclotron heating at a local mirror in the "C Stellarator" as due to the reflection of RF power by the plasma. They conjectured that this happens as soon as the transverse temperature reaches a point where the "group velocity" $(d\omega/dk_r)$ reverses sign, a situation very much like the one occurring in Fig. 4.19. From our analysis of instability boundary surfaces, we confirm that the plasma becomes nonconvectively unstable there. At that point, the complex "group velocity" $(d\omega/dk)$ vanishes and $\alpha > 1$. The plasma itself becomes an RF generator which feeds energy back into the driving source. For electrostatic waves, this point has been explained by Derfler in his treatment of gap impedance in hot plasmas [56,57]. This, we believe, is the real reason why the RF heating stops. However, a more detailed discussion of this instability in a magnetic mirror is necessary, because all the electrons with nearly parallel velocity are lost in this geometry, and thereby strongly affect the distribution function and the instability. This subject will be discussed in the next section.

4. Loss Cone Distribution

A plasma in an idealized magnetic bottle, with the magnetic field B_{min} in the midplane and B_{max} at the mirror point, can contain only electrons whose velocities are outside the loss cone

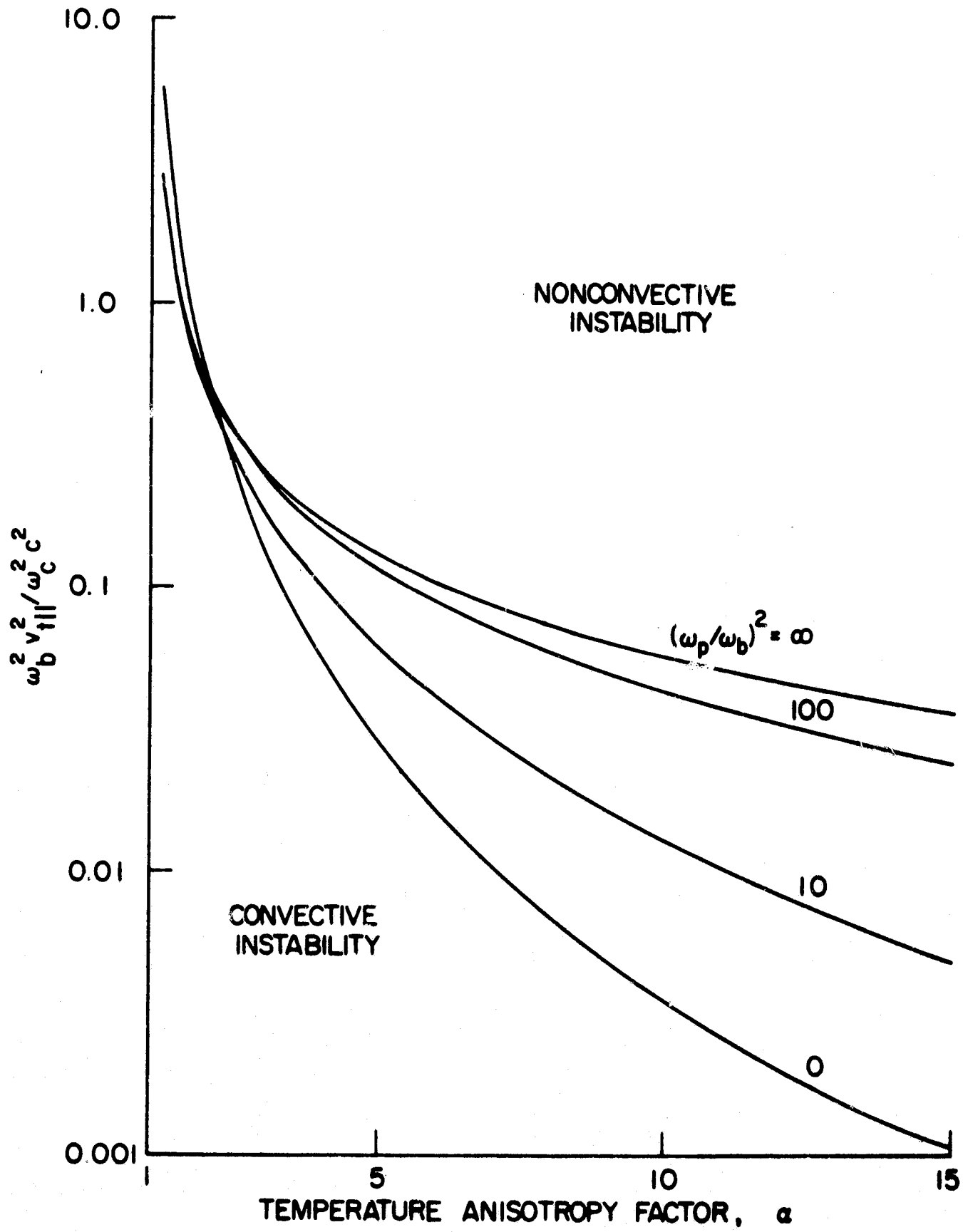

FIG. 4.22. CROSS-SECTIONS OF THE WHISTLER INSTABILITY BOUNDARY, EQ. (4.37).

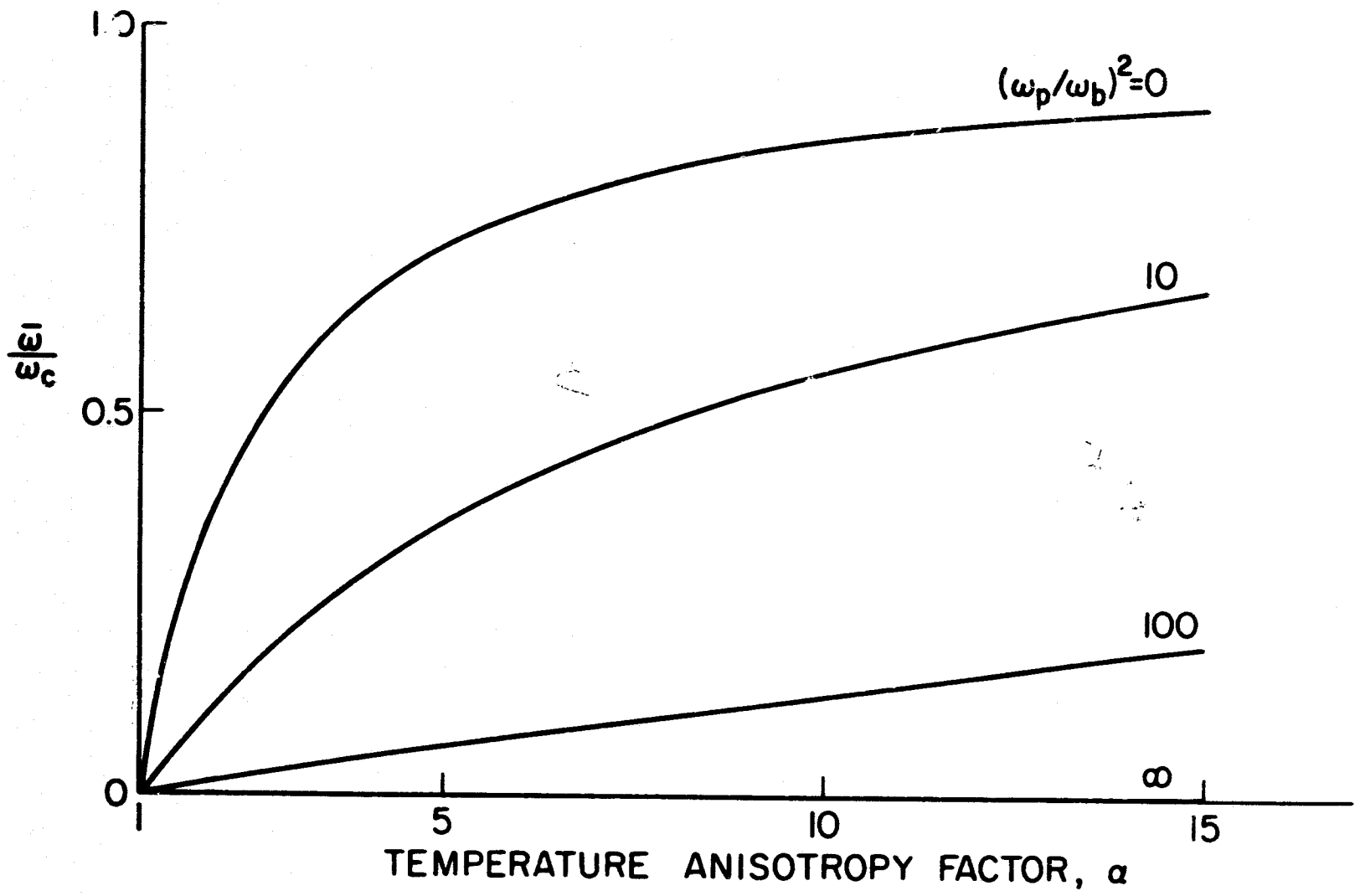

FIG. 4.23. LOCI OF BRANCH POINTS ON THE INSTABILITY BOUNDARY, EQ. (4.37).

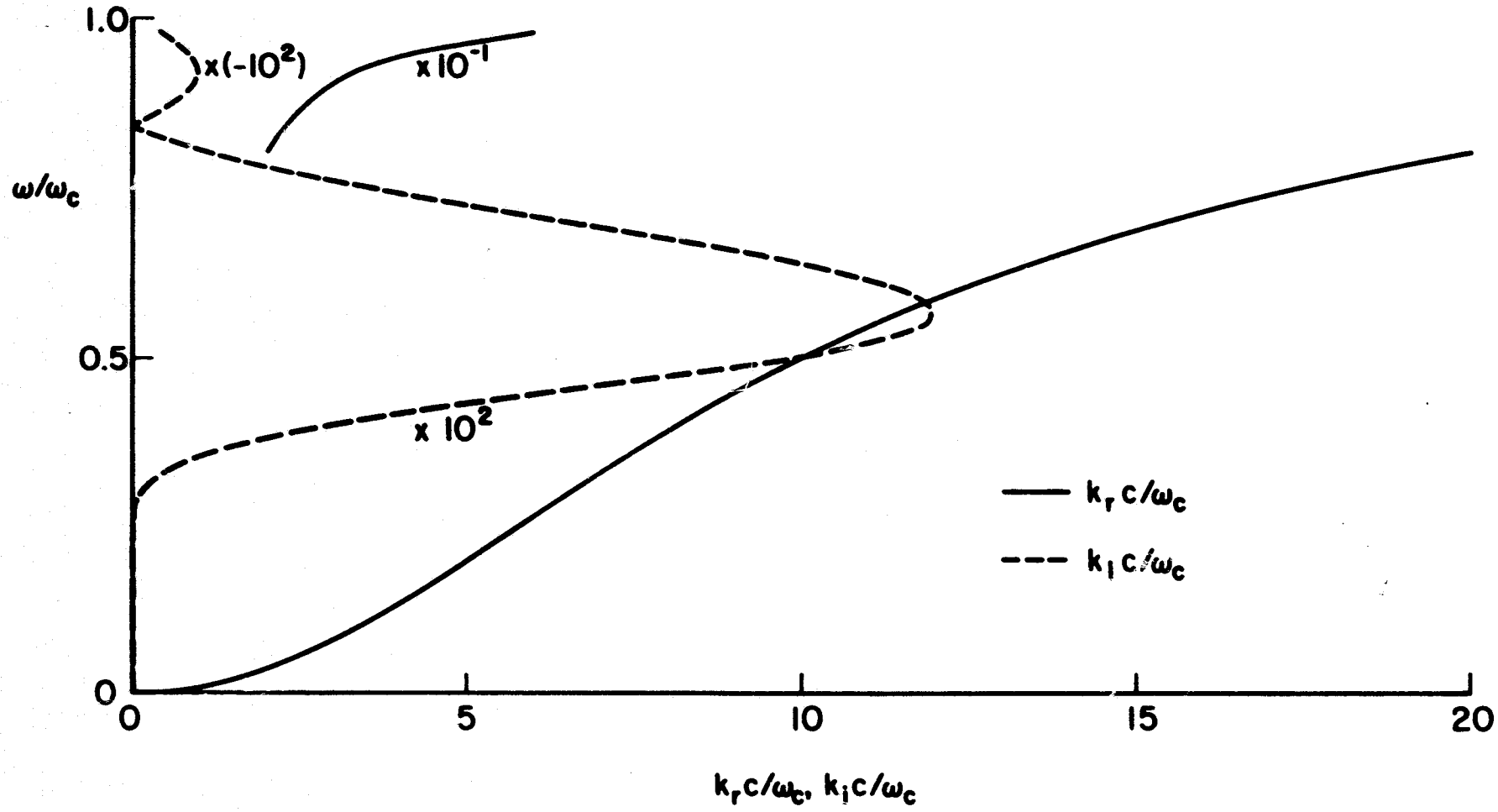

FIG. 4.24. BRILLOUIN DIAGRAM OF REAL ω vs. COMPLEX k FOR CONVECTIVELY UNSTABLE WHISTLERS [$\omega_p^2/\omega_c^2 = 100$, $\omega_b^2/\omega_c^2 = 1$, $v_{t\parallel}/c = 0.04$, $\alpha = 6.25$].

$$v_\perp / |v_\parallel| > \gamma = (R - 1)^{-1/2} \quad , \tag{4.38}$$

where $R(= B_{max}/B_{min})$ is the mirror ratio. The electron velocity distribution can be written accordingly

$$f_b(v_\parallel, v_\perp) = f(v_\parallel, v_\perp)\, H(v_\perp - \gamma |v_\parallel|) \quad , \tag{4.39}$$

where $f(v_\parallel, v_\perp)$ is an arbitrary continuous distribution function, and H is the Heaviside unit step function. The dispersion function of the right-hand polarized waves can be written in terms of the Φ and ψ functions (Eqs. (2.36) and (2.37)) as discussed in Chapter II. For an anisotropic Maxwellian distribution

$$f(v_\parallel, v_\perp) = \frac{1}{N} \left(\frac{1}{\pi v_{t\perp}}\right)\left(\frac{1}{\pi v_{t\parallel}}\right)^{1/2} \exp\left[-\left(\frac{v_\parallel}{v_{t\parallel}}\right)^2 - \left(\frac{v_\perp}{v_{t\perp}}\right)^2\right] \quad , \tag{4.40}$$

where

$$N = \frac{\alpha}{\alpha + \gamma^2}, \quad \alpha = v_{t\perp}^2 / v_{t\parallel}^2 \quad ,$$

these integrations can be carried out in a trivial way, by means of the Hilbert transform of the Gaussian (Eq. (3.23)), and give the result

$$D(\omega,k) = 1 - \left(\frac{kc}{\omega}\right)^2 - \frac{\omega_p^2}{\omega(\omega - \omega_c)}$$

$$+ \left(\frac{\omega_b}{\omega}\right)^2 \left\{\frac{\omega}{N k v_{t\parallel}} Z(\xi) - \frac{1}{2}(\alpha - 1) Z'(\xi) + \frac{1}{2}\gamma^2 [1 - \xi^2 Z'(\xi)]\right\} = 0 , \tag{4.41}$$

where

$$\xi = (\omega - \omega_c)/k v_{t\parallel} N \quad , \tag{4.42}$$

and ω_p is the plasma frequency of a cold plasma background which we have added. This formula has been obtained for $\omega_p = 0$ by Scharer [48] in a rather tedious manner. He got numerical solutions for a few cases with k real and ω complex, and one case with ω real and k complex. His calculations for $R = 2$ and $\alpha = 1$ show that the loss cone effect alone can cause whistler instability, though the nature of the instability was not determined.

Our calculations for $\omega_p/\omega_c = 0$, and two values of mirror ratio ($R = 2$ and 10) again exhibit in Fig. 4.25 the reversal of "group velocity" ($d\omega/dk_r$) which Iiyoshi *et al* have blamed for the failure of ion cyclotron heating in the local mirror of the C Stellarator. For the purpose of checking the instability character, we locate the branch point, $\bar{\omega}$, by means of the colliding pole criterion (Section A2), and track its location as a function of the mirror ratio, R, and electron thermal speed $v_{t\parallel}$, as shown in Fig. 4.26. It is seen that by increasing R, or by decreasing $v_{t\parallel}$, the nonconvective instability can be quenched.

To investigate further means of eliminating the nonconvective instability, we consider the effects of varying the densities of the cold plasma and of the hot electron population, ω_p^2 and ω_b^2. By tracking the branch point, $\bar{\omega}$, we obtain the data shown in Fig. 4.27. This result demonstrates that one can stabilize the system by reducing the hot electron population, or by adding enough cold plasma background. After the nonconvective instability is quenched, the instability will be convective, and it makes sense to plot real ω versus complex k, as in Fig. 4.28, to predict the outcome of a wave experiment.

5. Summary

In this chapter, we have studied whistler instability characteristics for a series of electron velocity distributions. In Section B, we have studied whistler interaction with a gyrating electron beam in a cold plasma with temperature effects as perturbations. In Section C, whistler instability in non-drifting anisotropic plasmas has been investigated. We found that, in each case, the instability is due to electron transverse energy. The instability can be thought of as Doppler shifted in the real and complex frequency domain by beam drift and parallel velocity spread, respectively. In the absence of cold plasma background, and under the

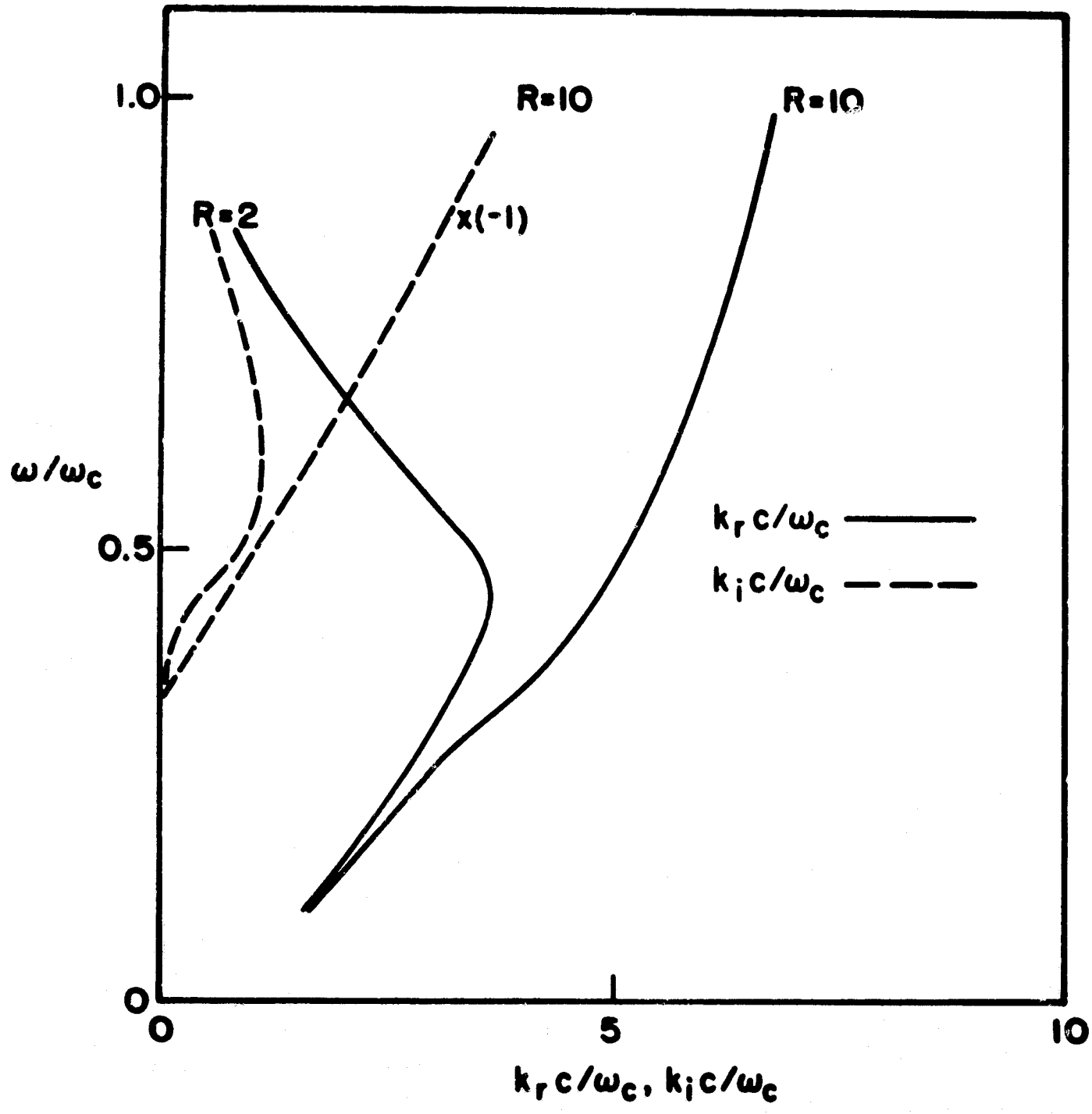

FIG. 4.25. BRILLOUIN DIAGRAM OF REAL ω vs. COMPLEX k FOR LOSS CONE DISTRIBUTION $[\omega_p^2/\omega_c^2 = 0,\ \omega_b^2/\omega_c^2 = 25,\ v_{t_{\parallel}}/c = 0.1,\ \alpha = 1]$.

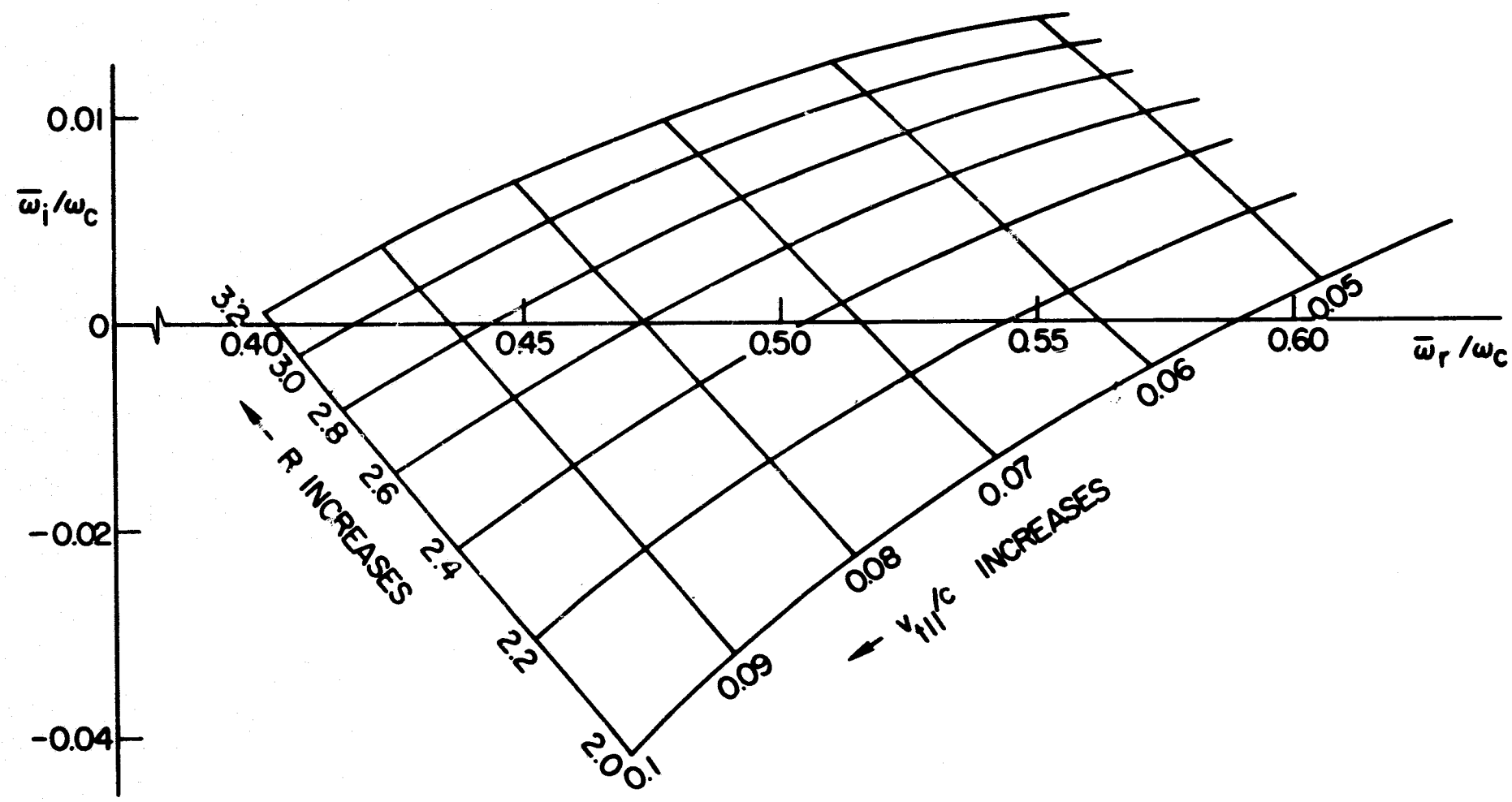

FIG. 4.26. CONTOUR MAP OF THE BRANCH POINT $\bar{\omega}$ AS A FUNCTION OF MIRROR RATIO, R, AND THERMAL SPEED, $v_{t\parallel}$ $[\omega_p^2/\omega_c^2 = 0,\ \omega_b^2/\omega_c^2 = 25,\ \alpha = 1]$.

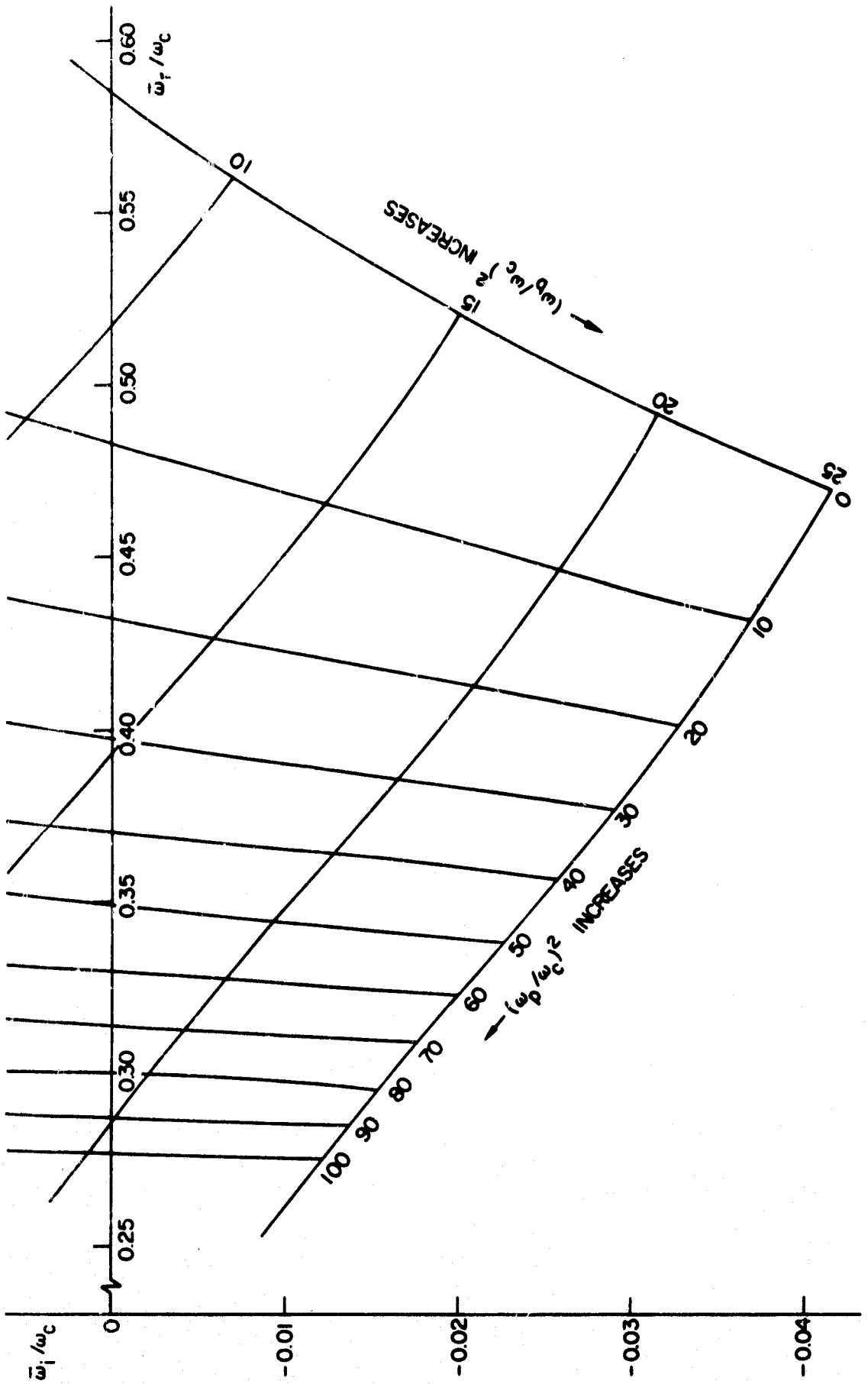

FIG. 4.27. CONTOUR MAP OF THE BRANCH POINT $\bar{\omega}$ AS A FUNCTION OF COLD PLASMA DENSITY, ω_p^2/ω_c^2, AND HOT PLASMA DENSITY ω_b^2/ω_c^2 [R = 2, $v_{ti}/c = 0.1$, $\alpha = 1$].

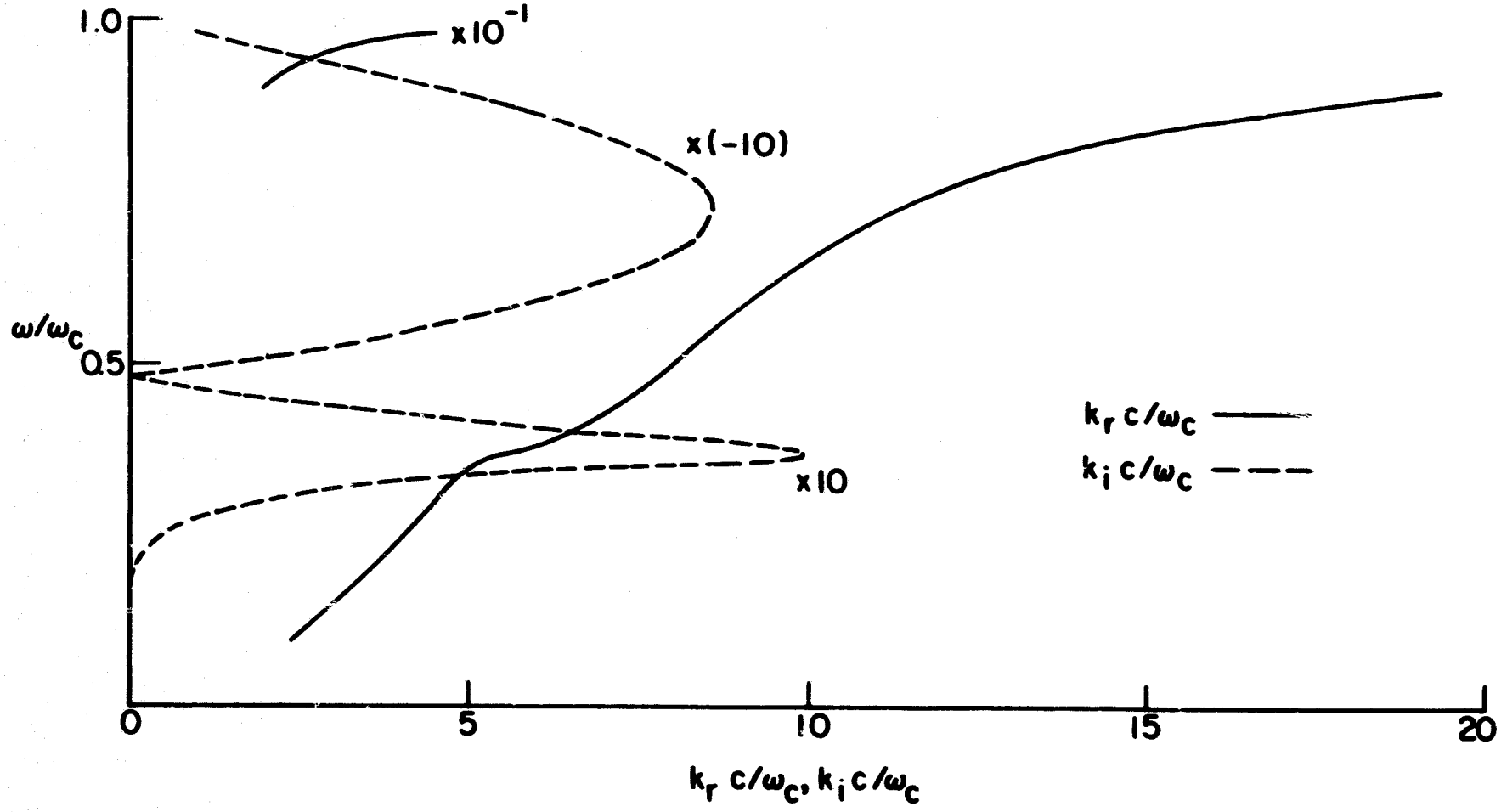

FIG. 4.28. BRILLOUIN DIAGRAM OF REAL ω vs COMPLEX k FOR A CONVECTIVELY UNSTABLE WHISTLER IN A MAGNETIC MIRROR [$R = 2$, $\omega_p^2/\omega_c^2 = 40$, $\omega_b^2/\omega_c^2 = 15$, $v_{t\parallel}/c = 0.1$, $\alpha = 1$].

condition $\omega_b \gg \omega_c > \omega$, this has been readily seen for the case of a resonance distribution for the parallel velocities. For anisotropic plasma with more energy perpendicular to the magnetic field than parallel to it, whistler instability occurs below the marginal wavenumber. The instability can be convective or nonconvective depending on the parameters. For an anisotropic Maxwellian distribution, the instability boundary has been found. For other distributions, we have demonstrated that the instability boundaries should be similar to the anisotropic Maxwellian case, i.e., for fixed hot electron population and energy, convective instability can be made nonconvective by increasing the energy anisotropy. For fixed energy anisotropy, nonconvective instability can be quenched by reducing the hot electron population, or their kinetic energy.

Quantitative differences for different distributions can be seen by comparing Section C3 and Appendix B. Under the conditions of convective instability, we see that the growth rate for a Maxwellian distribution (Fig. 4.24) at $\omega/\omega_c < 0.1$ is extremely small, while for a resonance distribution (Fig. 4.16) the growth rate is quite large. This is because the resonance distribution has more electrons in the high energy tail than the Maxwellian distribution. For whistlers at very low frequencies $\omega/\omega_c \to 0$, the wavenumbers become small. The synchronism condition $v_{\parallel} = W = (\omega - \omega_c)/k$ requires the interacting electrons to have extremely high velocity, and the nonrelativistic treatment breaks down.

With a nonrelativistic formulation of the whistler dispersion for all the distributions considered, we found that only one saddle point is important in each case for determining the instability character. We also find that this saddle point can be tracked from the beam/plasma interaction to an anisotropic Maxwellian, and to the loss cone distribution, by continuously varying the parameters. Moreover, in the limit of $v_{t_{\parallel}} \to 0$, this saddle point approaches the unstable saddle point of the ring distribution, which can be solved analytically.

In connection with the instabilities predicted in this work, it should be noted that nonlinear processes must eventually take over. It has been pointed out by Stix, however, that the range of validity of linear theory for whistler waves may be broader than that for electrostatic waves [74].

V. LABORATORY WHISTLER EXPERIMENTS

A. INTRODUCTION

Magnetospheric whistlers propagate in a magnetoplasma of very high refractive index, i.e., their propagation velocities are slow compared with the speed of light. Such propagation can be simulated in laboratory plasmas by scaling to higher frequencies, higher plasma densities, and stronger magnetic fields. As the signal frequency and magnetic field strength are raised to gigahertz and kilogauss levels, the plasma dimensions required for approximately plane whistler propagation reduce to practical limits for high density laboratory plasmas. The main advantages of studying simulated magnetospheric whistlers in laboratory plasma are that the equipment is accessible, that the discharge parameters can be controlled, and that measurements should be easily repeatable.

1. Historical Review

Whistlers were first observed in the laboratory by Gallet et al [14], in 1960, using the large thermonuclear fusion study machine "Zeta", at Harwell, England. In the experiment, probe-like dipole antennas were inserted into the middle of the discharge. The maximum plasma frequency was 100 GHz. With the cyclotron frequency varying from 3 to 40 GHz, a good approximation to infinite medium geometry was obtained. With the antennas separated by about 20 cm, a transmitted signal at 3 GHz was observed when the cyclotron frequency was raised above the signal frequency.

Since then, several whistler experiments in the laboratory have been reported. In 1961, Consol' and Dagai [15] worked in the millimeter wave range and checked the cutoff conditions for the right- and left-hand polarized waves. In 1963, Mahaffey [16] reported experiments at 10 GHz in a pulsed P.I.G. discharge. By comparing the experimental time observed for transmission, and the cutoffs for wave propagation, the various modes described by the CMA diagram were qualitatively identified. In the same year, Dushin et al [17] worked on a similar problem, in the same frequency range, but also considered the influence of collisions on whistler propagation.

Most of the results reported in the early experiments were brief and of a semiquantitative nature. They were followed by some more detailed studies. In 1964, Dellis and Weaver [18] again used 10 GHz microwaves in a whistler propagation study in the laboratory. Their mode identification was accomplished by comparing with Langmuir probe measurements. Sharp and Hooker [19] reported laboratory whistler measurements near the cyclotron frequency with 15 GHz microwaves. Bachynski and Gibbs [20] measured the collisional damping effect on whistlers at 10 GHz. Recently, Brand and Hooker [21] reported a whistler experiment at 33 GHz in a large volume (10 cm in length and 10 cm in radius) of hydrogen and helium plasma produced by crossed-field breakdown. Their plasma was not dense enough to cut off the left-hand polarized fast waves for the high signal frequency they used.

The overall conclusions to be drawn from the results of these experiments are that the waves can be described by plane wave theory when their wavelengths are small compared with the dimensions of the plasma, and that under these circumstances their propagation characterisitcs can be used as a diagnostic tool for the determination of electron density.

Because of the stringent requirement of large columns of high density plasma for approximately plane wave whistler propagation in the laboratory, the plasmas used in the experiments referred to above were all pulsed. The magnetic field needed for supporting the whistler mode helps to confine a high density plasma. For this reason, P.I.G.-type discharges are often used in laboratory whistler experiments, despite their well-known tendencies towards instability. Interferometry techniques were universally used in the later experiments [16-21]. All antennas were fixed. Most of them were outside the plasma column.

2. The Present Experiments

The distinguishing feature of the present experiments is that whistler measurements have been made by means of small movable loop antennas immersed in the plasma. By changing the separation between the antennas, whistler spatial wave patterns have been measured for the first time with interferometer techniques. Since the measurement is straightforward, the data can be readily interpreted. The complications of antenna near field effects, or of sheath regions near the plasma boundaries

are avoided by such a technique, and extraneous wave effects due to reflection or additional surface wave propagation can be detected whenever they are appreciable. By eliminating or avoiding these effects, very good wave patterns and exponential damping curves have been obtained. Whistler dispersion curves have been obtained over a wide parameter range, and compared with theoretical curves. Very good agreement has been obtained for wavenumbers, and reasonably good agreement for attenuation rates due to collisions.

B. APPARATUS

Whistler propagation was measured in the apparatus shown in Fig. 5.1. The vacuum system consists principally of sections of commercial glass pipe, 7.5 cm inside diameter, joined with neoprene "O"-ring seals. The system is pumped with a 10 cm oil diffusion pump with water-cooled baffle. The base pressure of the system is approximately 2×10^{-6} Torr.

1. Magnetic Field

Sixteen magnetic coils connected in series create a static magnetic field along the axis of the discharge tube. Each coil is made of 57 turns of square hollow copper wire impregnated with epoxy. Cooling is provided by running water through the wires. Each coil has a width of 3 cm and an inner diameter of 18 cm. Silicon controlled rectifiers are used in the power supply for the magnetic coils. With an RC ripple filtering circuit, these coils can produce a steady, continuously adjustable magnetic field from almost zero up to 1.5 kilogauss. The nonuniformity is 0.6 percent over a length of 40 cm. There is a 360 Hz ripple of less than 0.3 percent over the normal working range. The axial variation of the magnetic field is depicted in Fig. 5.2.

The purpose of the magnetic field is twofold: First, for plasma generation, it guides the primary (ionizing) electrons produced by the electron gun assembly along the tube axis, and allows most of them to pass through the anode hole. Second, it opens a propagation window in the overdense plasma ($\omega_p > \omega$) for whistler propagation.

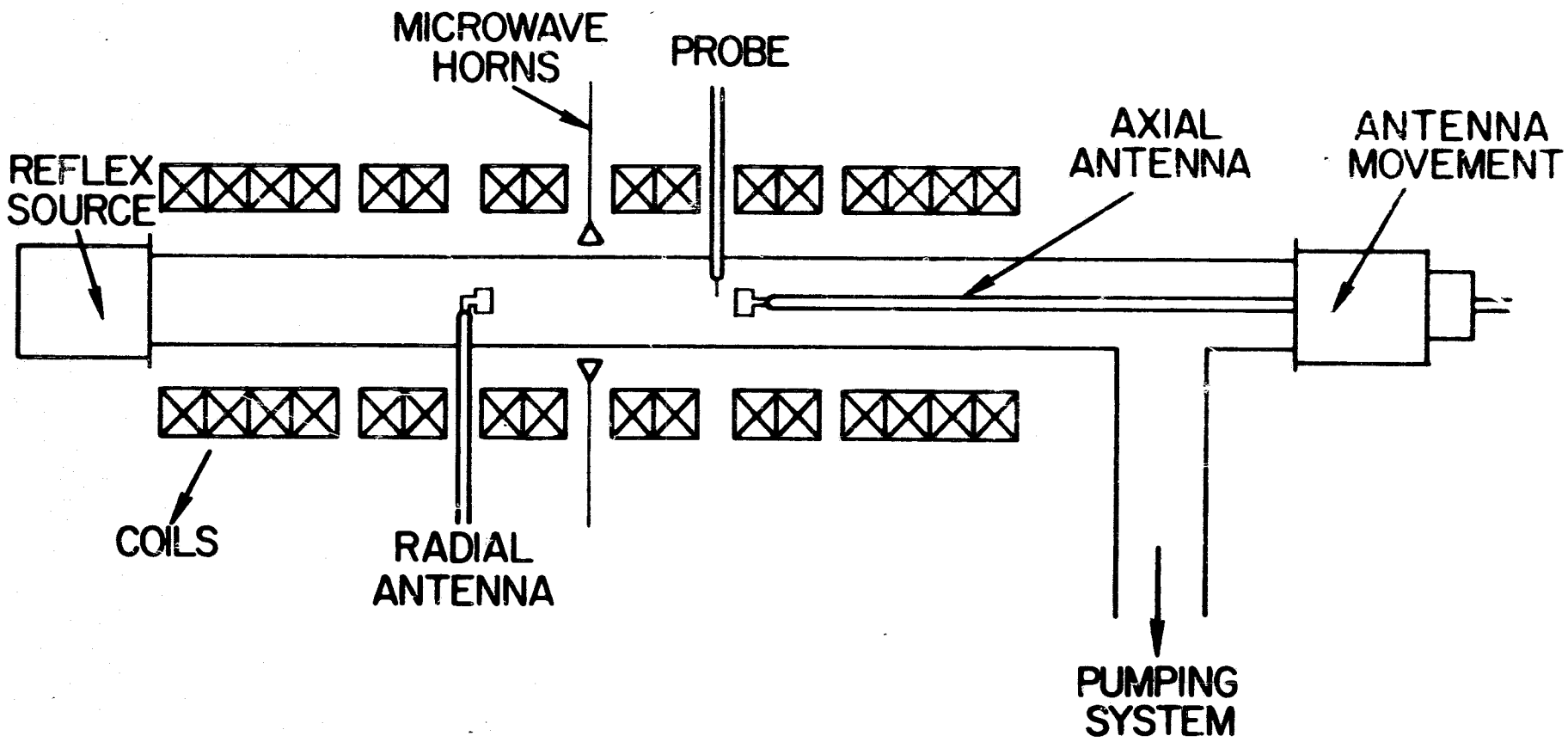

FIG. 5.1. SCHEMATIC OF SET-UP FOR WHISTLER EXPERIMENTS.

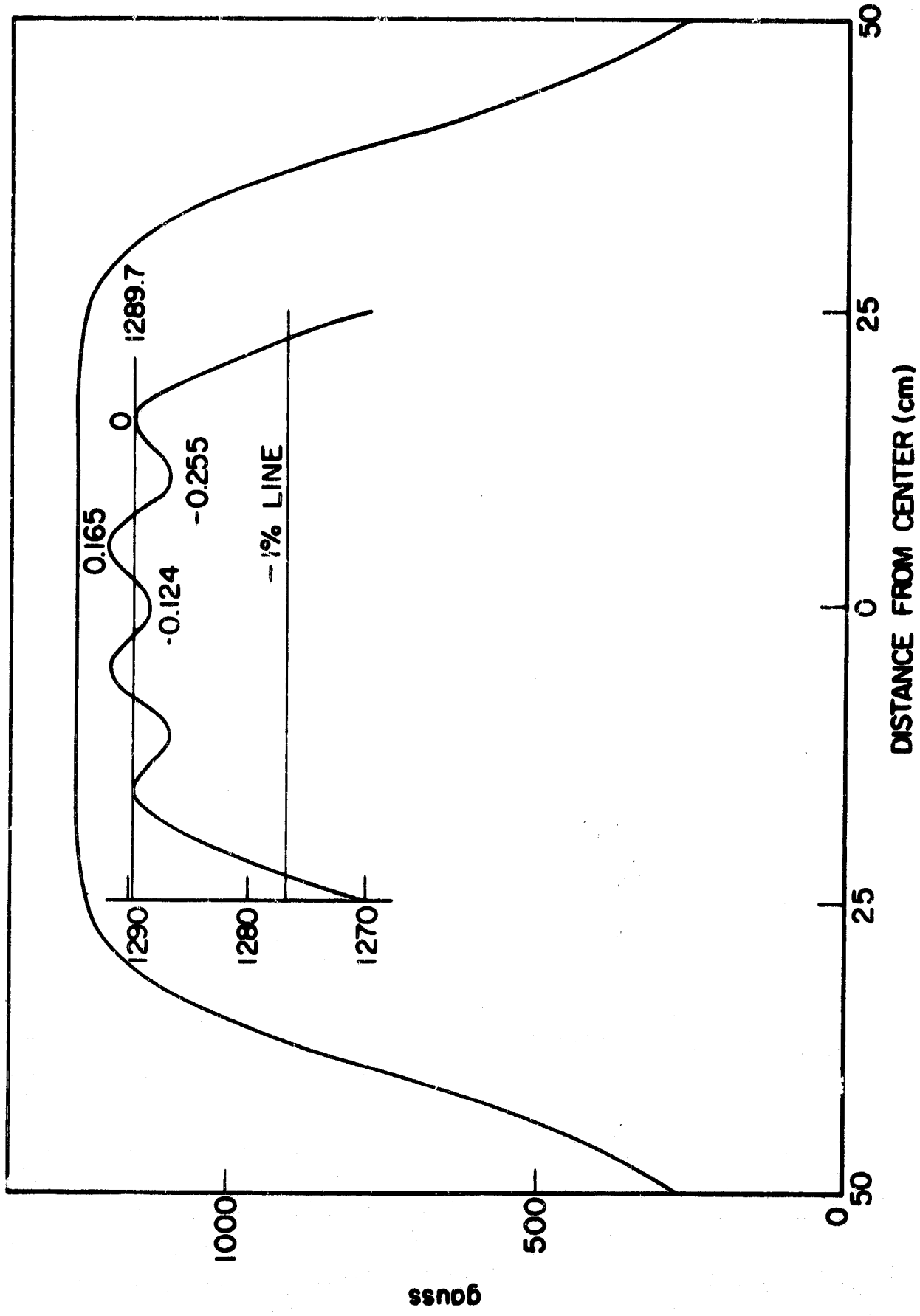

FIG. 5.2. AXIAL MAGNETIC FIELD VARIATIONS AT 100 AMPERES MAGNETIC FIELD CURRENT.

2. The Plasma

The plasma is produced by a pulsed hot cathode reflex discharge (P.I.G.) developed by Geller [76]. The hollow cylindrical anode is 4.0 cm long with tapered orifices from 5.5 cm to 4.5 cm in diameter. The dc heated cylindrical cathode, constructed from nickel mesh, is 3.2 cm long. A coating, composed of a mixture of nickel powder and oxides of barium and strontium, is deposited on the mesh.

While operating the experiment, argon is admitted through a needle valve to the region where plasma is to be produced, and continuously pumped through the system. Stable plasma can be produced in the range of 1 to 10 mTorr, so all our whistler experiments were carried out at a few mTorr, pressure.

With the anode grounded, a discharge is produced by application of a negative voltage pulse to the cathode. A capacitor bank, fired by a vacuum tube switch, provides the voltage pulses. The pulse repetition rate is synchronized to the ac power line and can be 30 or 60 pps. The pulse width can be varied continuously from zero to 400 μs for stable performance. Synchronizing the pulse to the ac power line helps to eliminate problems with ripple in the system. The peak voltage of the pulse can be varied continuously from 0 to 500 V with peak current of about 40 A. During the pulse, a primary electron beam with energy up to 500 eV makes electron-neutral collisions and generates the plasma. At the end of each pulse, the plasma reaches a maximum density of about $6 \times 10^{13}/cm^3$, and then decays essentially to zero before the start of the following pulse. The whistler experiments to be reported here were performed in the afterglow of the decaying plasma.

3. Probes and Interferometer

The plasma density was measured using radially movable Langmuir probes in conjunction with a microwave interferometer operating at 25 GHz in the ordinary mode, i.e., with the electric field parallel to the static magnetic field lines. The probe is made of 1 mm ground tungsten rod. The rod is first shielded completely with a thin layer of glass, with one side of the tip ground off as shown in Fig. 5.3. The exposed flat surface area is 1.03×10^{-3} cm^2. The probe location in the system is near the whistler propagation path, as shown in Fig. 5.1. The probe is

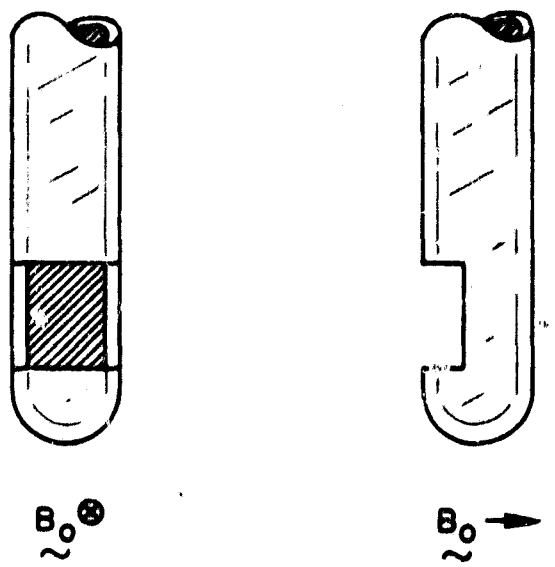

FIG. 5.3. LANGMUIR PROBE.

radially movable so that the local plasma density profile across the plasma column can be measured. The probe is installed in the system with its exposed surface facing the reflex plasma source, and perpendicular to the axial magnetic field. This arrangement should reduce the effect of magnetic field on the conventional Langmuir probe theory. Furthermore, the probe was biased at -22.5 V and, consequently, drew ion-saturated current. This current is proportional to the local plasma electron density, if the density is large enough to maintain charge neutrality.

The transmission microwave interferometer used in this study is illustrated in Fig. 5.4. The microwave signal, supplied by a klystron, propagates along two paths, the probing path and the reference path. The signal in the probing path penetrates the plasma region, whereas the reference path by-passes the plasma. Probing and reference signals are compared to determine the plasma effect on the amplitude and phase of the probing signal. A magic tee is used to compare these two signals. Two ports of the magic tee serve as imputs for the probing and reference signals. The other two ports are terminated in balanced crystals.

A magic tee possesses the important property that the two input signals add at one port and subtract at the other. For balanced bridge detection, the probing and reference signal are summed, and detected by a square-law detector. Let V_p be the probing signal and V_r be the reference signal at the detector, we have

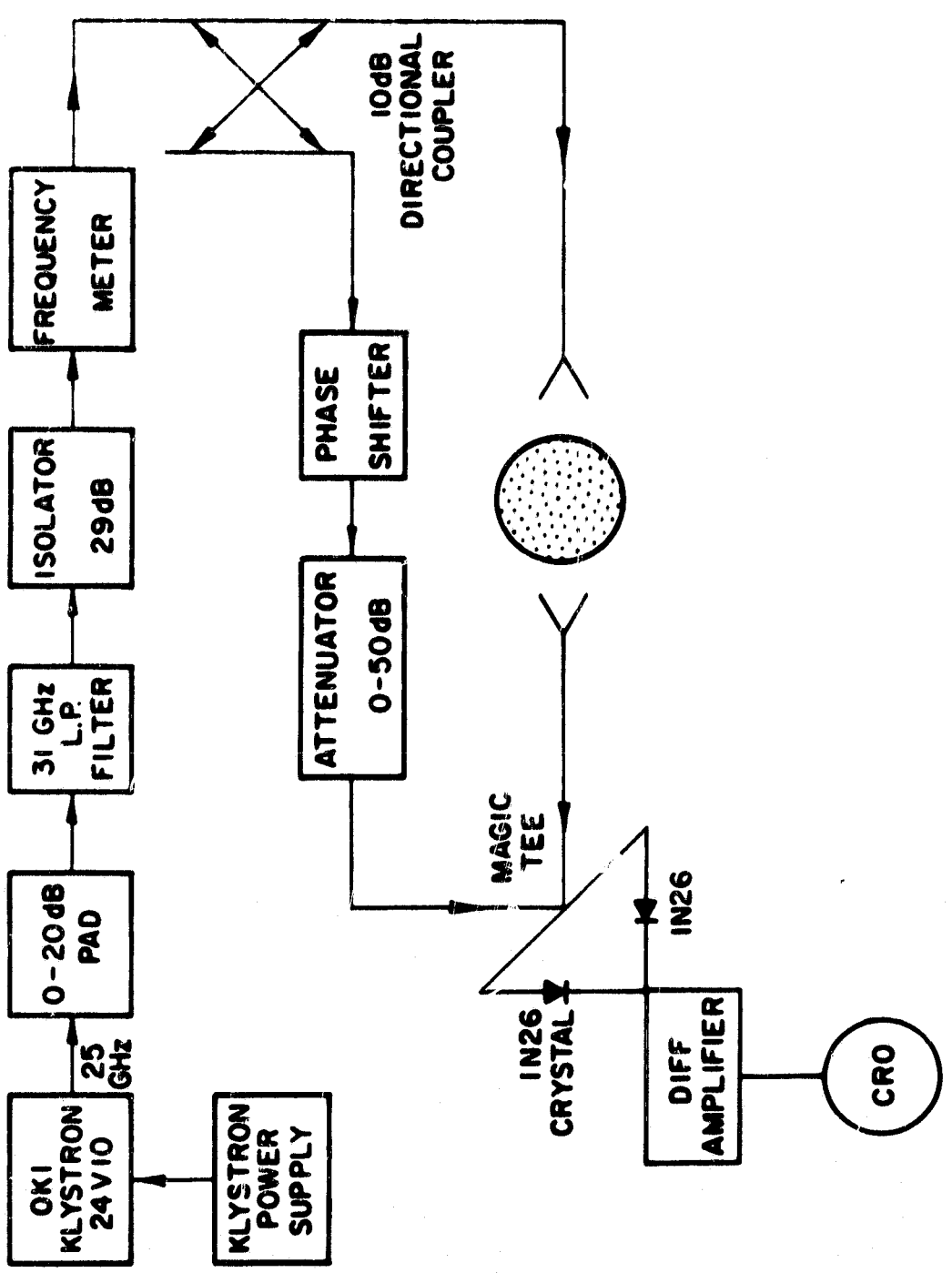

FIG. 5.4. K-BAND MICROWAVE INTERFEROMETER.

$$V_p = - A \sin \omega t, \quad V_r = B \sin (\omega t + \delta) \quad . \tag{5.1}$$

The amplitude and phase of V_p are adjusted so that, with no plasma in the probing signal path, the sum, $V_p + V_r = 0$, i.e.

$$\delta = 0 \quad , \quad A = B \quad . \tag{5.2}$$

For arbitrary V_p and V_r, the output of the square-law detector at Output Port 1 is

$$V_{01} = G[-A \sin \omega t + B \sin (\omega t + \delta)] \quad , \tag{5.3}$$

where G is the gain of the detector. Keeping only the dc components, we have

$$\overline{V}_{01} = \frac{G}{2} (A^2 + B^2) - GAB \cos \delta \quad . \tag{5.4}$$

For Output Port 2,

$$\overline{V}_{01} = \frac{G}{2} (A^2 + B^2) + GAB \cos \delta \quad . \tag{5.5}$$

Subtracting Eq. (5.4) from Eq. (5.5), the detected voltage, V_{det}, applied to the CRO by the differential amplifier is given by

$$V_{det} = 2GAB \cos \delta \quad . \tag{5.6}$$

Thus the dc components of the reference and probing components, as well as any correlated noise, are discriminated against in the final detection output. A zero reference line can be obtained by letting $\cos \delta = C$, or $A = 0$, or $B = 0$.

4. <u>The Whistler Antennas and Sampling Circuit</u>

Helices, small electric dipoles, and small loops were all studied as possible antennas for whistler launching and receiving. It was found that loop antennas are the most efficient for the range of experimental parameters used. A radially movable antenna is inserted into the system

and placed at the axis of the system. An axially movable antenna is inserted along the axis of the system from the end opposite to the reflex source. The loops are made from 0.75 mm stainless steel wire, with a rectangular area of about 1 cm^2. The loops are at the end of 6 mm diameter glass tube. The normals to the loop planes of the antennas are made perpendicular to the axial static magnetic field lines, and to each other. This geometry has the following advantages:

(1) The main RF magnetic field component of the loop is perpendicular to the static magnetic field lines, and is readily coupled to whistlers.

(2) Direct coupling between the antennas is reduced. The coupling to electrostatic modes is also reduced.

(3) During the plasma pulse, the motions of primary electrons follow very closely the magnetic field lines. Any obstacle in their way will consequently block the electrons, and form a shadow. The shadow effect for the plasma is minimized by the loop antenna arrangement.

Since the loops are exposed to the plasma, RF coupling capacitors are used to block any DC path via the antennas. The axially movable antenna is motor driven with a variable speed of about 4 cm/min.

Because of the pulsed plasma decay with time, the wave properties of the medium change rapidly as a function of time. A sampling circuit was used to sample the rapidly varying signals at a particular time with reference to the pulse, or at a selected probe current. A schematic of this circuit is given in Fig. 5.5. The synchronous trigger driven by the 60 Hz power line is used as the "clock" for the system. A Tektronix Type 555 Dual Beam Oscilloscope is used for monitoring. The power pulse shape, ion-saturation current, and RF transmission evolve as time passes. The delay feature of the Type 22 time-base for the oscilloscope is used for selecting the sampling time; the delayed pulse is used to gate an operational amplifier (Type 0 plug-in). The output of the operational amplifier is connected to a peak reading circuit, which in turn is connected to the Y-input of an X-Y recorder. The X-input is connected to the axial antenna movement. The time sequence of the various "waveforms" is sketched in Fig. 5.5.

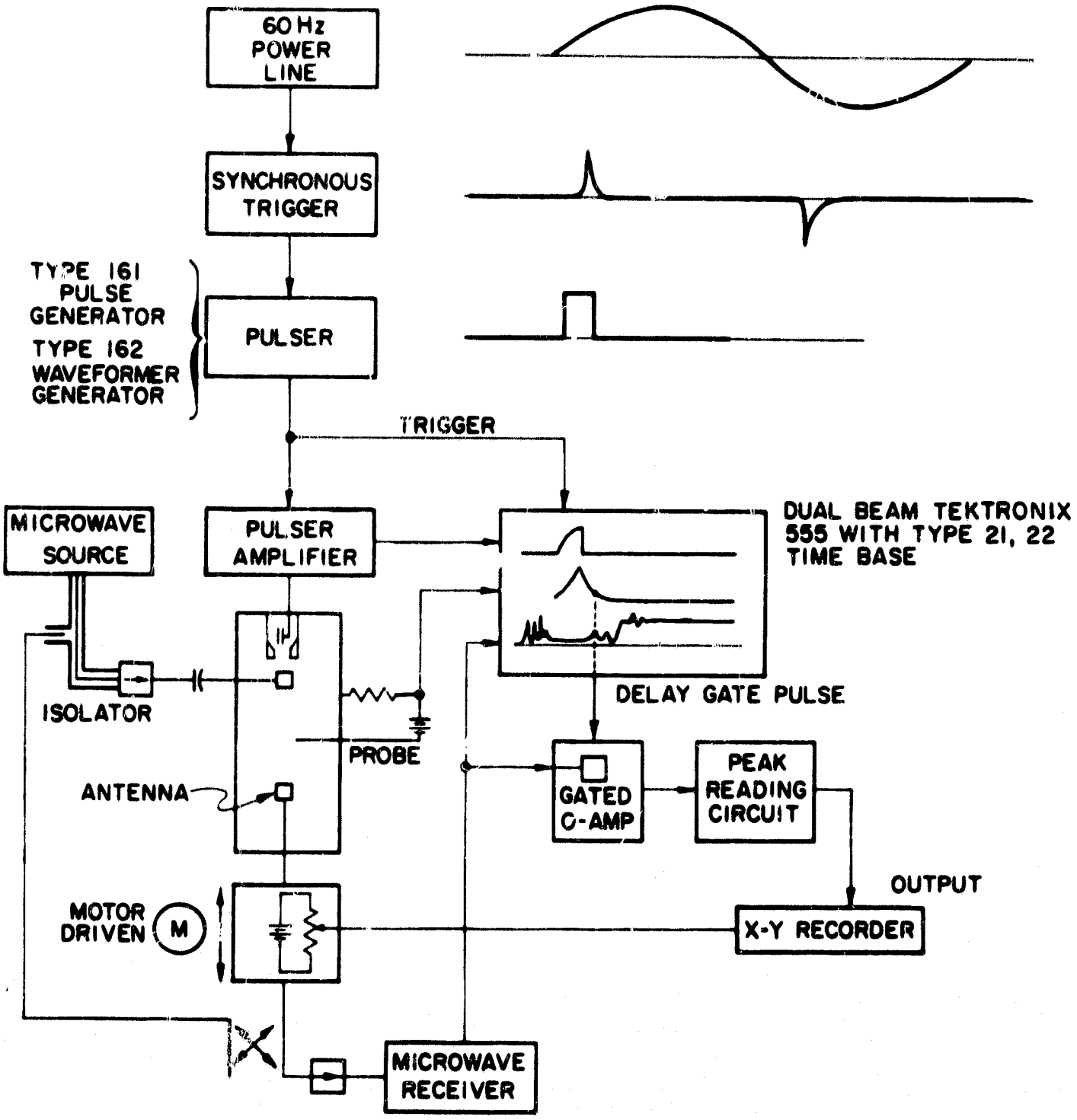

FIG. 5.5. SCHEMATIC OF THE SAMPLING CIRCUIT FOR WHISTLER MEASUREMENTS.

C. Plasma Diagnostics

1. Plasma Density Measurements

Microwave interferometry provides a valuable method of plasma density measurement. No new boundary is introduced into the plasma, and no appreciable disturbance is caused by the probing signal, provided reasonable amplitudes are used, and operation is well away from resonances. Since the ordinary mode is used, as the probing wave, interferometer data are dependent on electron density and collisions. Since there is no Landau damping for fast waves, the interferometer data may be related to electron temperature through collision frequencies. Fortunately, collisions are relatively infrequent compared to the interferometer frequency in the plasma under study, so that interferometry provides a straightforward method of electron density measurement.

In our experiments, the plasma electron density was measured with the aid of the 25 GHz microwave interferometer and the Langmuir probe. The ion saturation current to the probe was compared with density calibrations obtained from the interferometer measurements. This procedure gave an absolute calibration of the probe current in terms of the average density of the plasma column at the position of the interferometer. Over our experimental range, it was found that the probe current was linearly related to density.

From experimental electron density measurements showing an initial decay as t^{-1}, it was deduced that volume recombination was dominant. As the density falls, the diffusion process becomes more important, and in the late afterglow the plasma density falls exponentially. Measurements of the radial density profile of the discharge indicate that the plasma is highly nonuniform immediately after the pulse. This is illustrated in Fig. 5.6 and is due to the geometry of the reflex source, which has a cylindrical cathode of radius 1.7 cm. At the end of the pulse, the maximum plasma density occurs at the radius of the cathode, with a density minimum occurring along the axis of the system. As the plasma decays, the plasma density profile changes. From Fig. 5.6 it is seen that after 400 μs the plasma column become reasonably uniform.

For calibration purposes, the probe is placed 2 cm from the wall. At this position, and at times beyond 400 μs, the probe will measure the

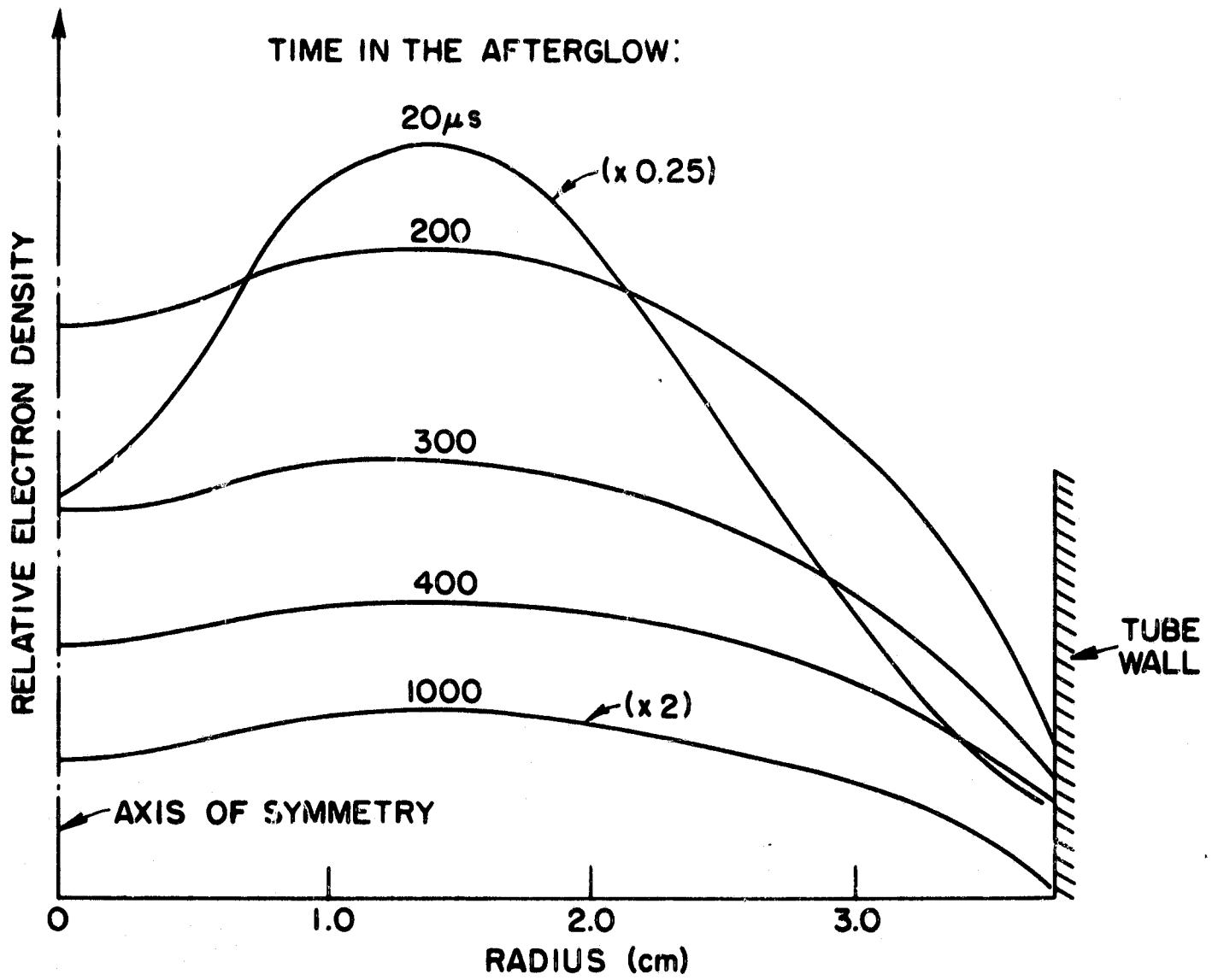

FIG. 5.6. PLASMA DENSITY PROFILE IN THE AFTERGLOW.

average ion saturation current for the cross-section in the afterglow plasma. The 25 GHz interferometer shows cutoff at high plasma densities, close to the end of the plasma generating pulse ($\omega_p > \omega$). Since, close to plasma resonance, the probing wavelengths become very long, and since close to the maximum pulsed density the plasma profile shows strong radial inhomogeneity, we choose the first three 180° phase-shift points for density calibration. At these densities, the plasma column is quiescent with very good repetition in density and profile from pulse to pulse. The plasma density is quite uniform in the central region of system, and the plasma density at the calibration points is not so high that reflection and diffraction effects are important. Our whistler measurements were taken close to these calibration points.

Figure 5.7 contains oscillograms showing a typical plasma decay, with the associated interference fringes. From these data, the density calibration is 4×10^{12} electrons/cm^3/mA of ion-saturated current.

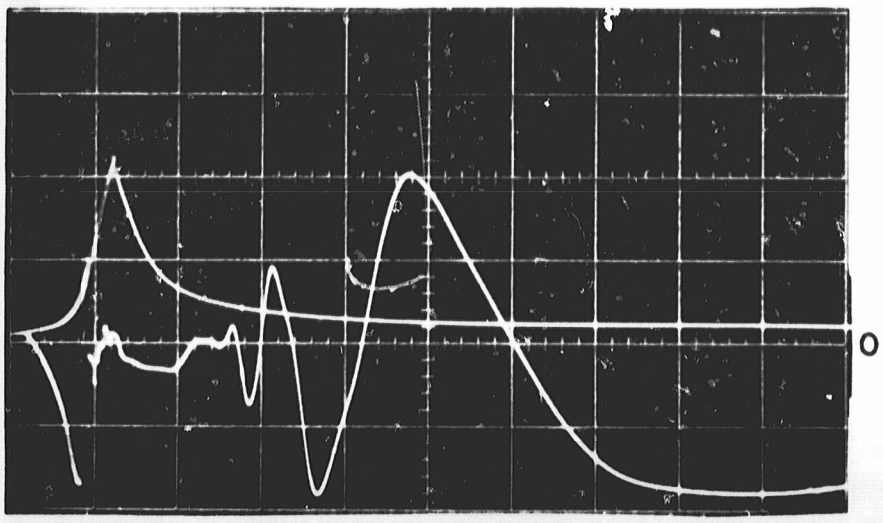

Fig. 5.7. OSCILLOGRAM OF PROBE CURRENT DECAY AND INTERFFRENCE FRINGES OF THE INTERFEROMETER.

2. Electron Temperature Measurements

From the electron density measurements, it is established that a fairly uniform, dense, quiescent, plasma column is obtained in the late afterglow. We have chosen that period for whistler experiments. In the

afterglow, the high energy primary electrons are no longer present, and the resulting electron velocity distribution is expected to be Maxwellian. Negatively biased Langmuir probe measurements of plasma electron temperature, in the absence of energetic injected electrons, have been shown experimentally by Wada and Knechtli [75], and by Hosea [76], to be reliable in the presence of magnetic fields from a few hundred to 1.5 kilogauss. The high energy tail of the Maxwellian distribution is not much influenced by the presence of the magnetic field, and is collected preferentially by the negatively biased probe. The recent theory due to San Martin [77] indicates that this method should give a reliable indication of plasma temperature, even in the presence of a magnetic field. When the magnetic field effect can be neglected, for negative bias voltage, we have

$$I = JA_p \exp\left(-\frac{eV}{KT}\right) , \qquad (5.7)$$

where I is the probe current component due to electrons retarded by the probe potential, V (measured with respect to "space" or "plasma" potential); J is the random current density directed towards the probe, and A_p is the probe area. For a Maxwellian distribution

$$J = n_0 e\left(\frac{KT}{2\pi m}\right)^{1/2} , \qquad (5.8)$$

where T, n_0, e, and m are the electron temperature, density, charge, and mass respectively and K is Boltzmann's constant. From Eq. (5.7) for fixed electron temperature, the $\ell n\ I/V$ curve is seen to be a straight line. Electron temperature is determined by the slope of the line.

For the afterglow plasma, the time-sampling [78] technique is used for the probe V-I characteristics. A complete curve is produced by assembling individual points taken from successive discharge pulses. This is executed by intensity-modulation of the TEK 555 oscilloscope. The CRO beam is turned on for a short period (1 to 2 μs) at a pre-selected time with respect to the start or end of each primary discharge pulse. The delayed gate signal from the Type 22A Time Unit is connected to the Z-modulation through an operational amplifier (Type 0 plug-in) for polarity inversion.

Typical probe characteristic curves close to the floating potential in the afterglow are given in Fig. 5.8(a). Semi-log plots of the probe high energy electron collection are shown in Fig. 5.8(b). Many such plots were used to construct the electron temperature evolution curves in the afterglow shown in Fig. 5.9. Typical values of electron temperature obtained for the period in the afterglow in which whistlers were studied were about 0.1 eV.

3. Collision Frequencies

We shall now use the electron temperature measurements in the afterglow to show that, for the low-pressure argon discharge (2 - 10 mTorr), electron-ion Coulomb collisions dominate over electron-neutral collisions for the entire range of parameters relevant to our whistler measurements. The electron-neutral collision frequencies used for comparison are calculated from data on momentum-transfer cross-sections for slow electrons published by Frost and Phelps [78].

The electron-ion collision frequency given by the Spitzer formula (Eq. (3.11)), is a function of the electron energy. An approximation to the exact calculation is obtained if the Spitzer formula is averaged over a Maxwellian distribution. The result of carrying out this averaging is quoted by Heald and Wharton [60] as

$$\nu_{ei} = 2.9 \times 10^{-6} \frac{n_0 \ \ell n \ \Lambda}{V_e^{3/2}} \qquad \text{collisions/sec} \quad . \qquad (5.9)$$

where n_0 is per cm^3; the electron temperature, V_e, is in volts, and Λ is 9 $\times$ (number of electrons in a Debye sphere). The quantity $\ell n \ \Lambda$ varies only very slowly over our parameter range and lies between 5 and 10. For argon, the two kinds of collision frequencies have been calculated for our parameter range and are shown in Fig. 5.10. It is clear that, for electron temperatures below 3 eV, electron-ion collisions always dominate.

Because of the rapid and inversely related dependence of cyclotron and collisional damping on plasma electron temperature, one damping mechanism or the other will almost always dominate. The damping due to Coulomb collisions increases very rapidly as the electron temperature becomes small. Conversely, cyclotron damping decreases even more rapidly

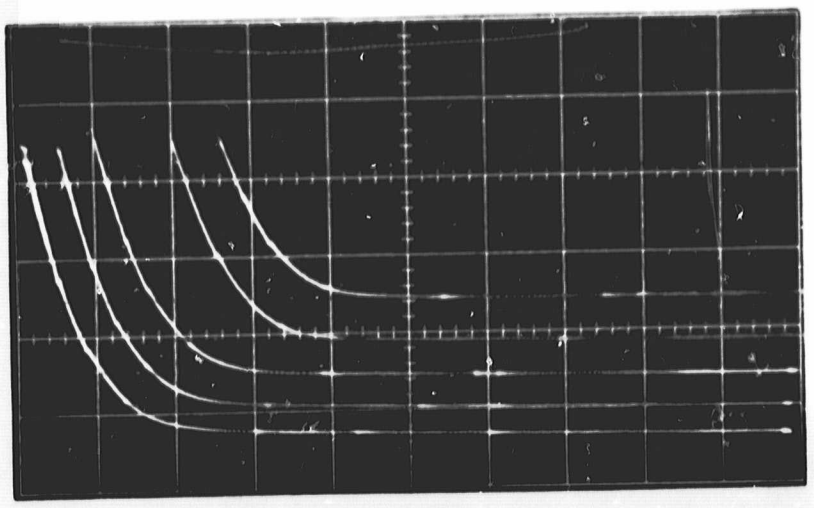

(a) Typical time sampled probe curves near floating potential at various times, τ, in the afterglow [From top to bottom τ = 1000, 900, 800, 700, 600 μs; horizontal scale 0.1V/cm, f_c = 2 GHz].

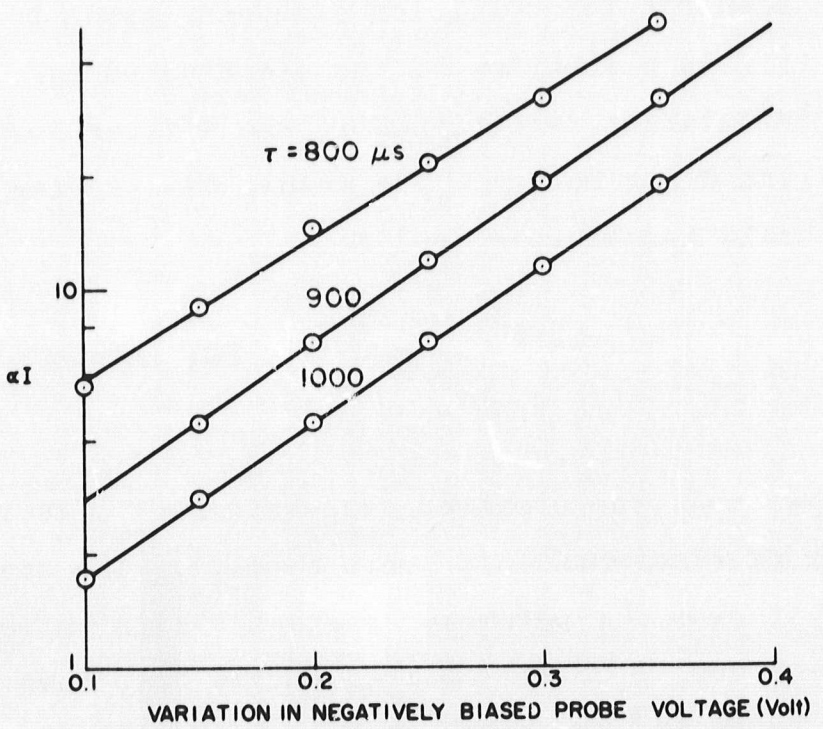

(b) Semilog plot of the probe electron collection.

FIG. 5.8. ELECTRON TEMPERATURE MEASUREMENTS WITH LANGMUIR PROBE.

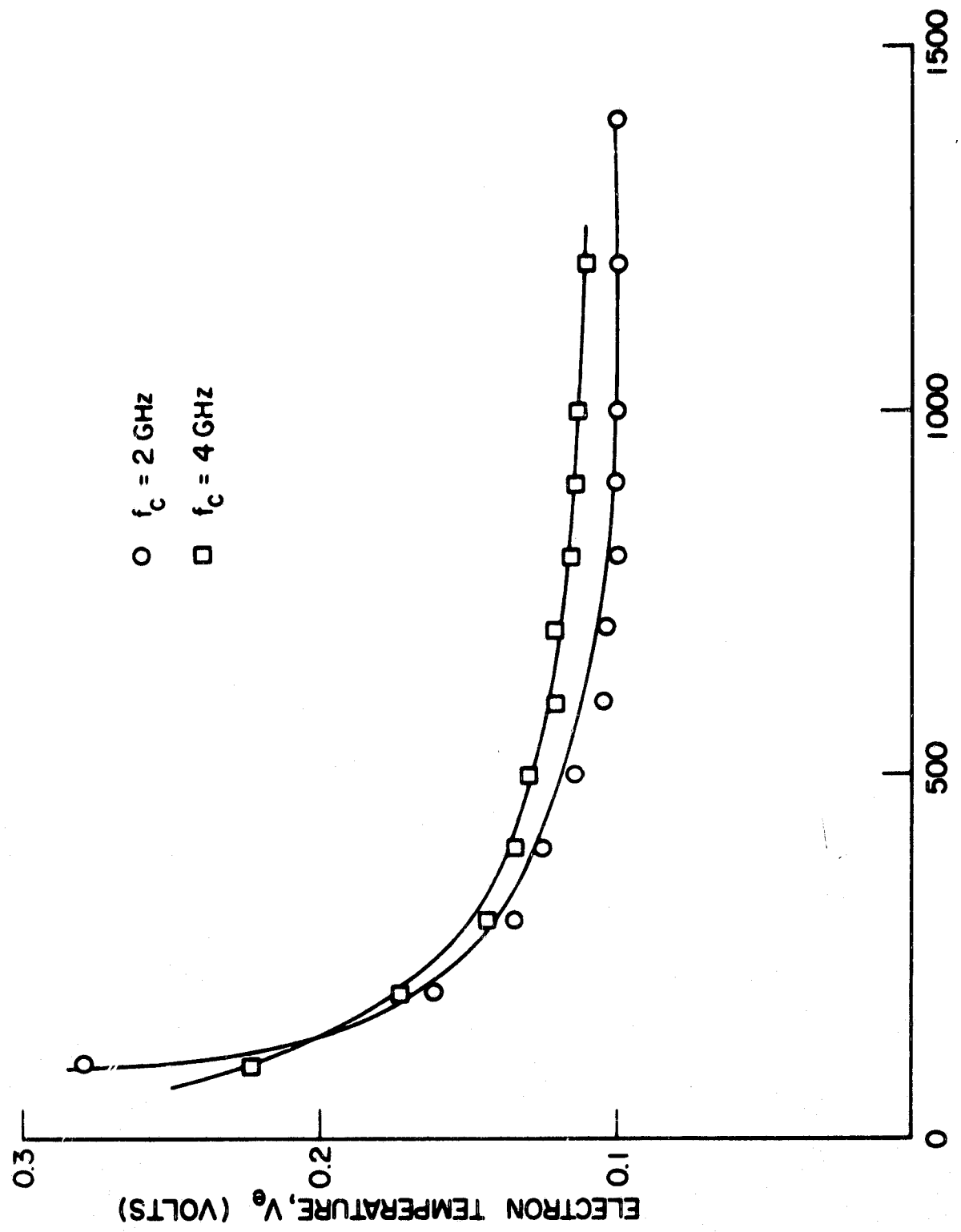

FIG. 5.9. PLASMA ELECTRON TEMPERATURES IN THE AFTERGLOW.

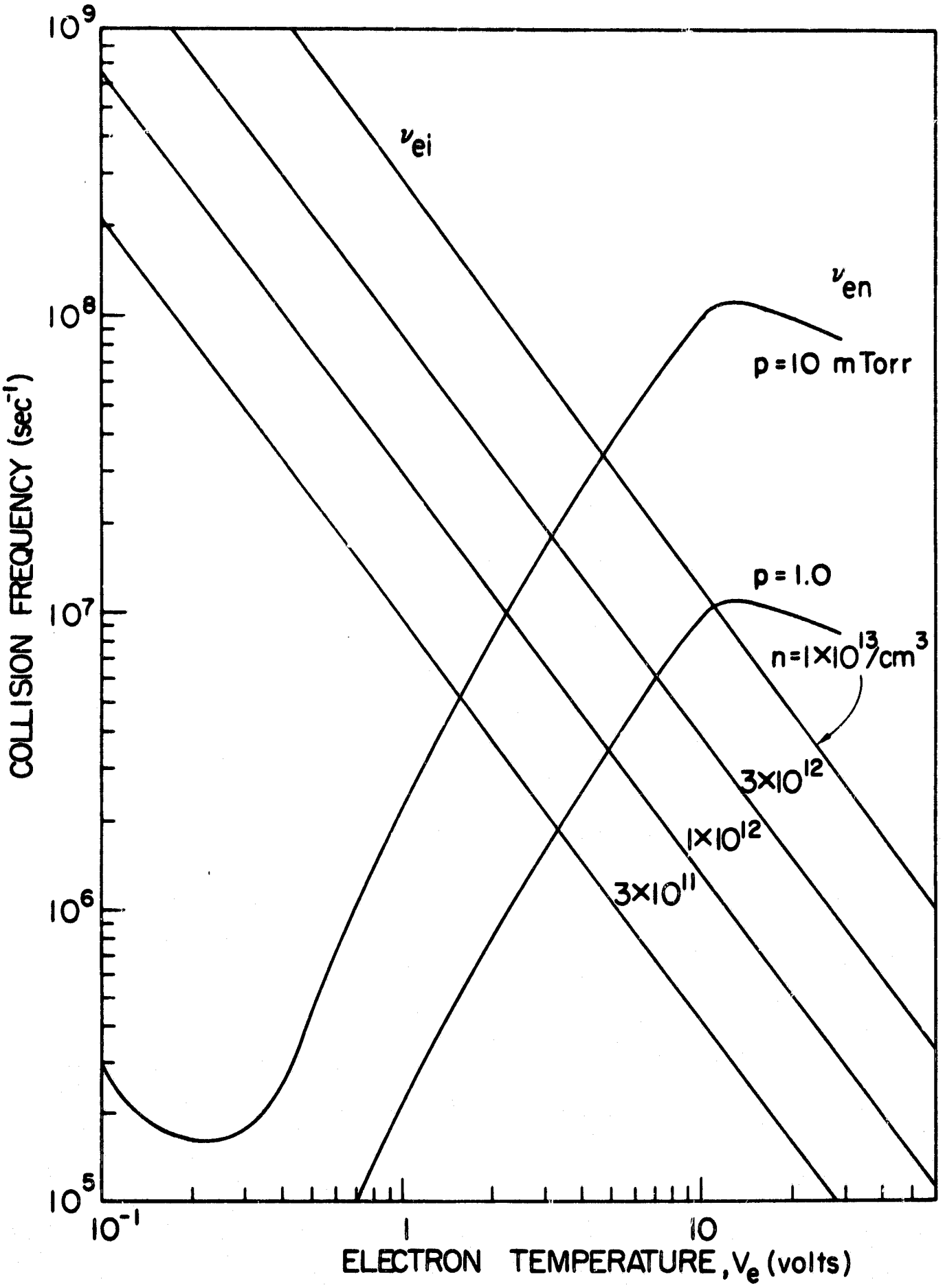

FIG. 5.10. COMPARISON OF ELECTRON-NEUTRAL WITH ELECTRON-ION COLLISION FREQUENCIES IN LOW PRESSURE ARGON PLASMAS.

as V_e becomes small. The locus of points where the cold plasma collisional damping is equal to the hot plasma cyclotron damping are shown as a function of ω/ω_c in Fig. 5.11. Here a normalized density of $\omega_p^2/\omega_c^2 = 20$ has been chosen as a typical experimental value. The curves have been computed by equating the imaginary part of k, calculated from Eqs. (3.5) and (5.9), with that computed from Eq. (3.22). It is clear that, unless the experimental parameters fall near this curve, any experimental phenomena observed can be explained by one of the two theories alone. Furthermore, in order to measure cyclotron damping of whistlers experimentally, it is necessary that the experiment be operated above the curve. For the present studies, the experimental parameters lie below the bounding curves. Thus, our experimental damping should be electron-ion collision dominated.

D. VERIFCATION OF THE WHISTLER DISPERSION RELATION

1. Qualitative Tests for Whistler Propagation

Initially, helices were used as antennas, and were designed to launch a right-hand polarized wave in the axial mode (n = -1), with a phase velocity of (c/10) at a frequency of 2 GHz. Figure 5.12 shows oscillograms of waves coupled between the two helices at 1.8 GHz. The plasma was produced by the plasma source operated in the pulsed mode. In the afterglow, the density decay indicated by ion saturation current is also shown in the figure (time increases and density decreases from right to left). Three photographs were taken for each situation. This reveals the stability of the pulsed plasma.

Figure 5.12(a) shows the complete time behavior of the waves coupled between the helices, with the probe current as an indicator of plasma density. This figure shows three groups of waves corresponding to different helix mode coupling between the helices. Figure 5.12(b) is an expansion of the first 500 μs of the waves of Fig. 5.12(a). Notice that, as the current used to produce the magnetic field is reversed, these waves disappear. This demonstrates that the initial waves are launched by the axial helix mode, since reversing the magnetic field in effect reverses the pitch of the helices, and cause them not to couple to the right-hand polarized whistler wave. At later times, the transmissions

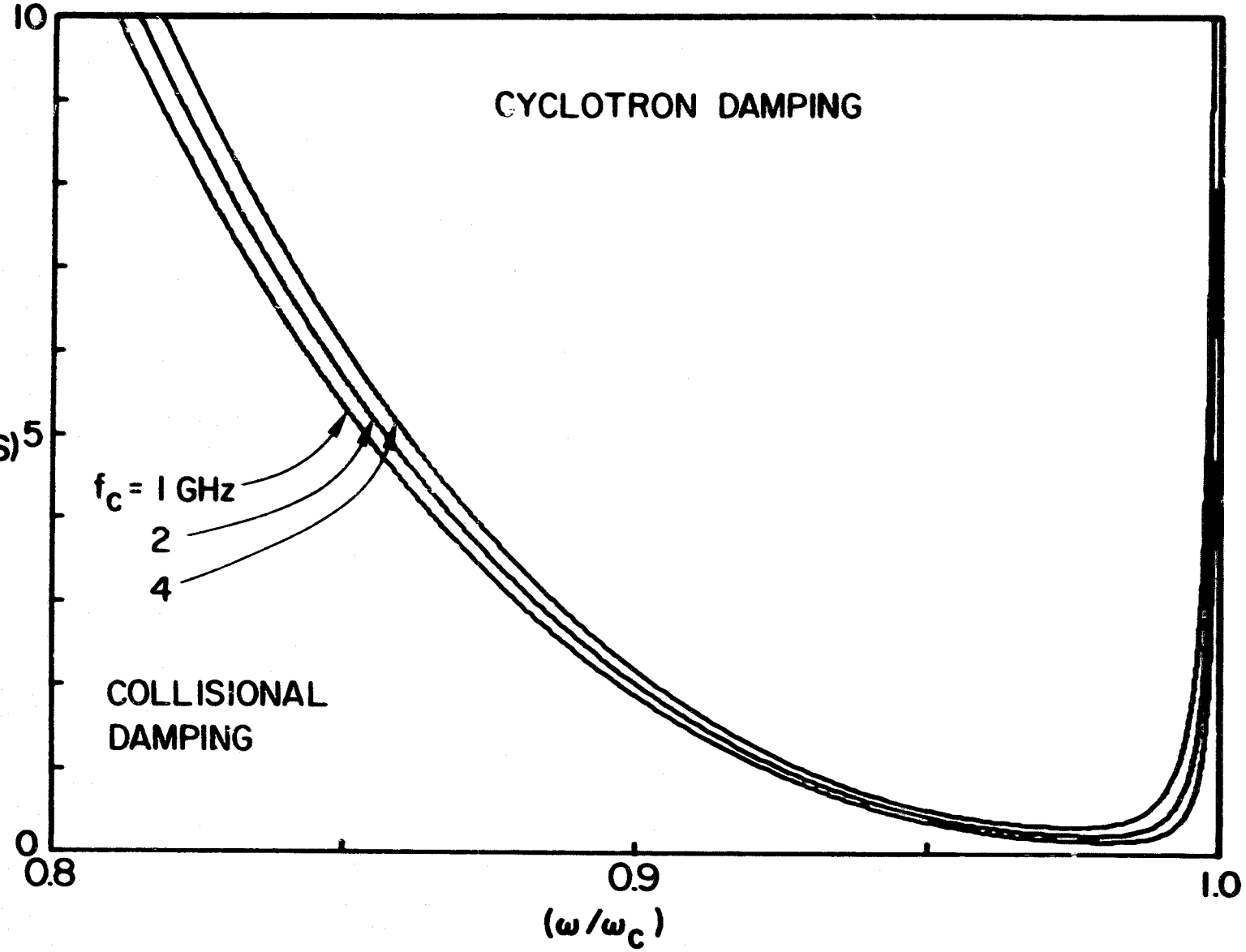

FIG. 5.11. CONDITIONS FOR EQUALITY OF CYCLOTRON AND COLLISIONAL DAMPING $[\omega_p^2/\nu_c^2 = 20]$.

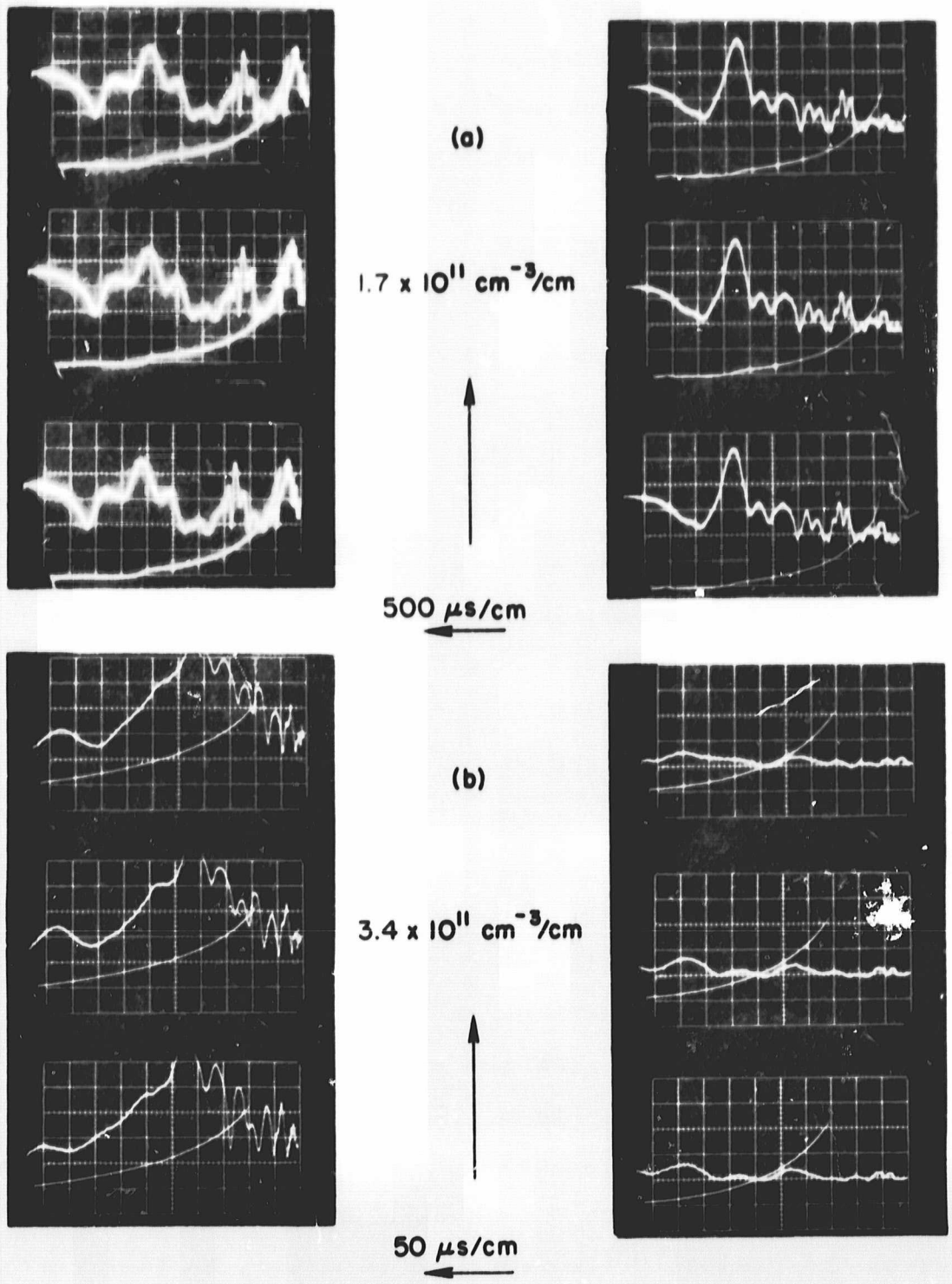

FIG. 5.12. TRANSMISSION BETWEEN HELICES AS A FUNCTION OF ELECTRON DENSITY. Left-hand set is for $\underset{\sim}{B}_0$ in correct direction for strong coupling to whistler mode. Right-hand set is with $\underset{\sim}{B}_0$ reversed.

do not disappear as the magnetic field is reversed, indicating that these signals are launched and received by helix modes that do not launch strictly right-hand polarized waves.

Figure 5.13 shows the magnitude of the waves coupled between the helices as a function of the magnetic field. At low magnetic fields the plasma densities are low ($\omega_p << \omega$). Consequently, there is a transmission caused by the fast E-M waves. As the field increases, the plasma begins to fill the region between the helices. These waves are cut off when the electron plasma frequency exceeds the applied frequency. There is no transmission until the electron cyclotron frequency exceeds the applied frequency, at which point the whistler mode begins to propagate.

2. Surface Waves

From the data on the measured plasma density profiles, it is clear that there exists a very low density region close to the wall of the plasma container. The "finiteness" of the plasma cross-section can allow surface waves to propagate [4]. In order to check the possible parasitic role played by surface waves in our whistler measurements, the RF field intensity profiles were measured as a function of radius under whistler wave measurement conditions. This was achieved by varying the position of the radially movable loop antenna between the axis of the system and the container wall. It was found that, except at relatively low plasma densities ($\sim 10^{11}$ electrons/cm^3), the RF field intensity was always monotonically decreasing from the axis to the wall. Typical RF intensity profiles are shown in Fig. 5.14. These RF intensity profile measurements show that surface waves are not strongly excited or coupled for the conditions under which our whistler measurements were obtained. Surface waves are basically electrostatic in nature, so that their coupling to the loop antenna should be small.

3. Whistler Dispersion Measurements

The setup described in Section B.4, was used with fixed magnetic field and fixed sampling time (or fixed electron density), and the coupling between the two antennas was measured as a function of antenna separation for frequencies between 1 and 4 GHz. The sampling pulse was chosen between 400 and 1400 μs, for which the plasma density profile was reasonably uniform.

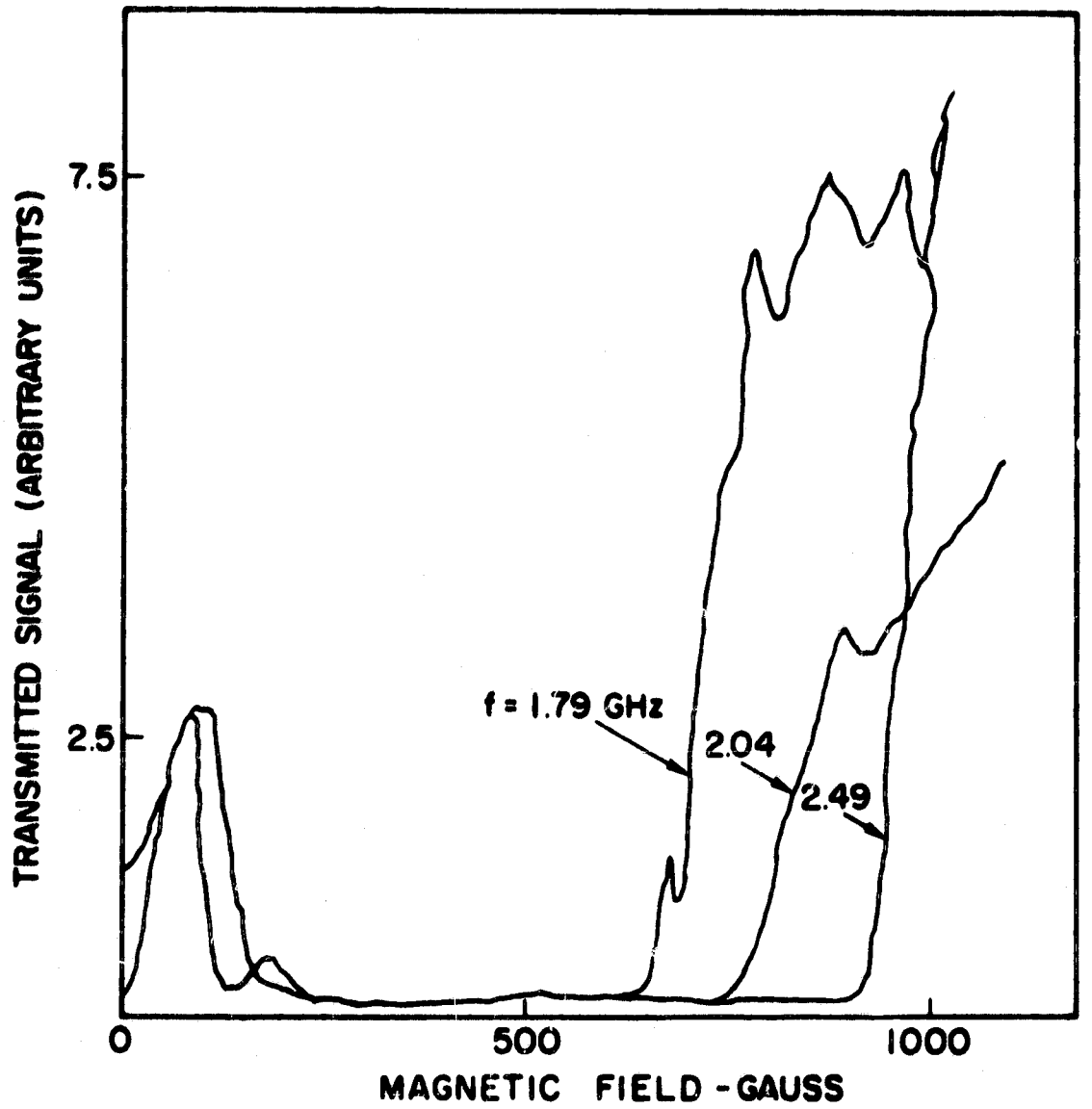

FIG. 5.13. TRANSMISSION BETWEEN HELICES AS A FUNCTION OF MAGNETIC FIELD AND FREQUENCY.

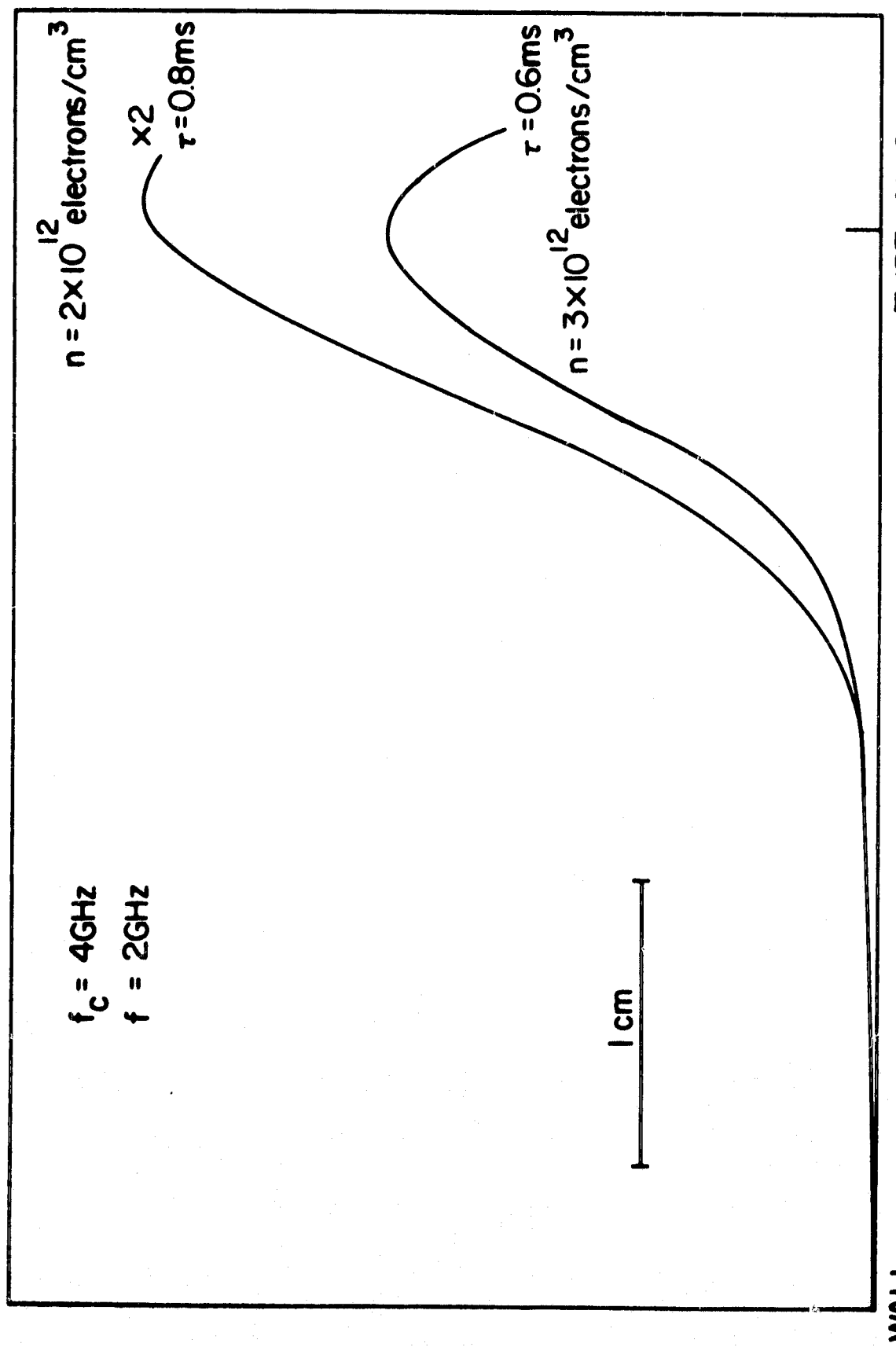

FIG. 5.14. RF FIELD STRENGTH PROFILE.

The tapering magnetic field strength near the two ends of the plasma column provides a magnetic beach to absorb whistlers. Thus, whistler reflections in the plasma are generally negligible. In the external circuit, isolators and attenuators are used to suppress reflections. Thus, by making use of a reference signal, the wavelength could be measured easily and directly from the whistler interferograms such as that shown in Fig. 5.15. The reference signal was always chosen to be stronger than the transmitted signal.

Without the reference signal, the transmitted signal varies exponentially with antenna separation, as shown in Fig. 5.15. This is so only if the wavelengths are small compared with the plasma column cross-section, and if the attenuation rate is not to small. Under these conditions, the boundary conditions and reflection effects are not important. Here a logarithmic converter has been used to convert the exponential decay curve into a straight line.

Results obtained from many interferograms are plotted in Fig. 5.16. The points are experimental results, while the curves represent the real and imaginary parts of the wavenumber for the cold whistler dispersion relation of Eq. (3.5), with collisions given by Eq. (5.9).

Figure 5.17 shows a measure of the axial antenna shadow effect caused by the Langmuir probe at 1 ms after the pulse. When the probe was aligned with the axial antenna, notice that the shadow effect produced less than 20 percent density variation over a length of 10 cm with a minimum separation of 1.2 cm. When the probe was 2 cm from the axis, no appreciable density variation can be found. With the K-band interferometer measuring across the plasma column, again no shadow effect can be detected in the afterglow. In the whistler measurement, the minimum and maximum antenna separations possible were 5 and 15 cm, respectively. Data were only taken, however, for separations between 10 and 15 cm. Thus the effective density of the measurement was in some cases approximately 25 percent lower than the measured density. This caused an error of 12.5 percent in the measured value of $k_r c/\omega_c$, but an error greater than 40 percent in the measurement of $k_i c/\omega_c$. The error bars of Fig. (5.16) were computed assuming an error of 20 percent in the measurement of plasma density.

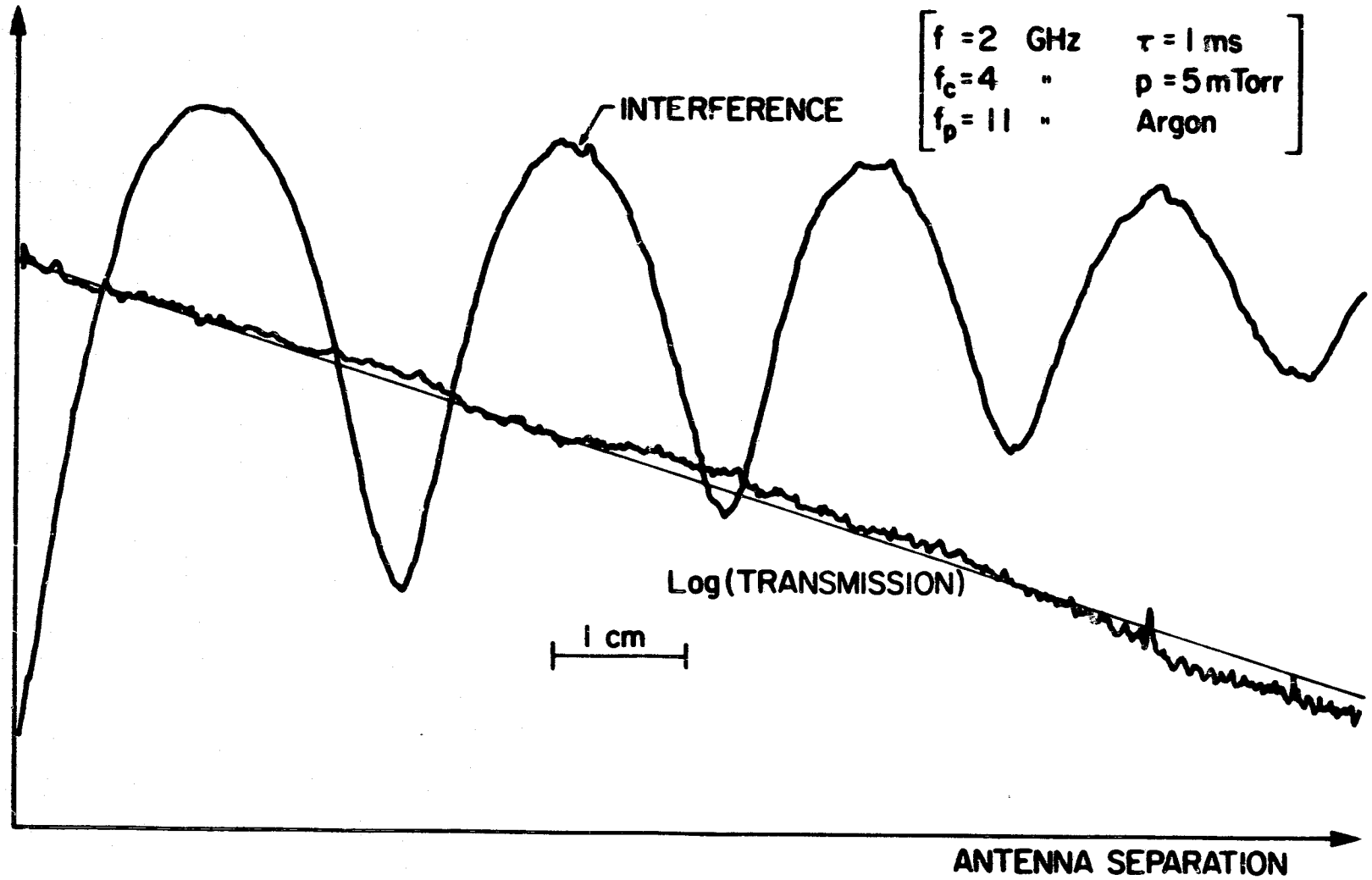

FIG. 5.15. TYPICAL WHISTLER TRANSMISSION AND INTERFERENCE RECORDS.

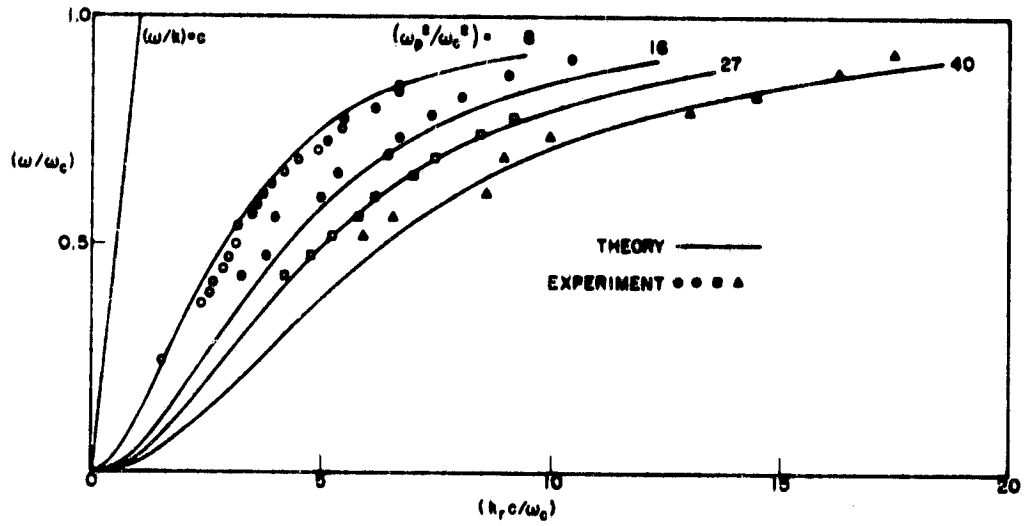

(a) ω/ω_c **vs** $k_r c/\omega_c$

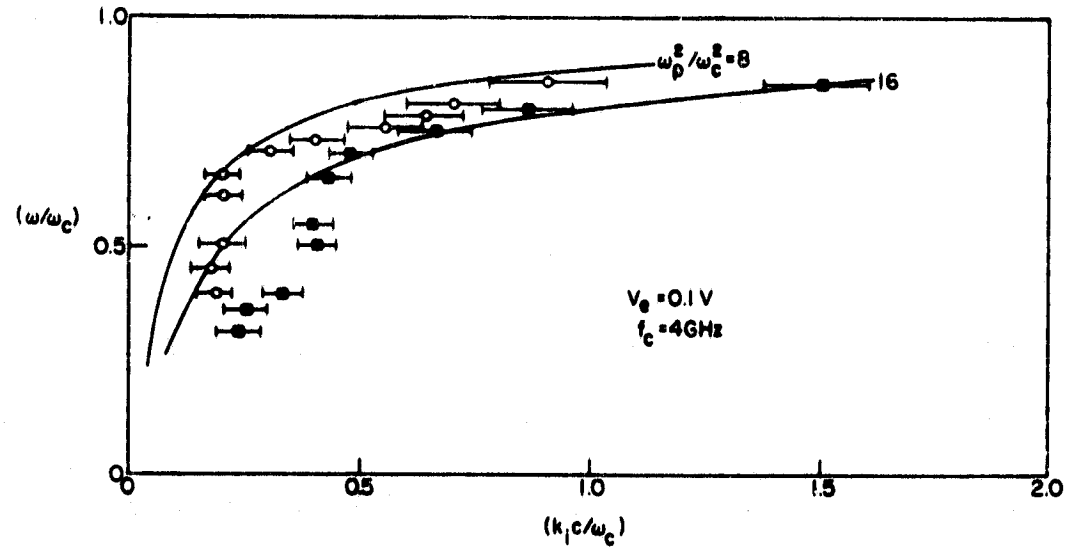

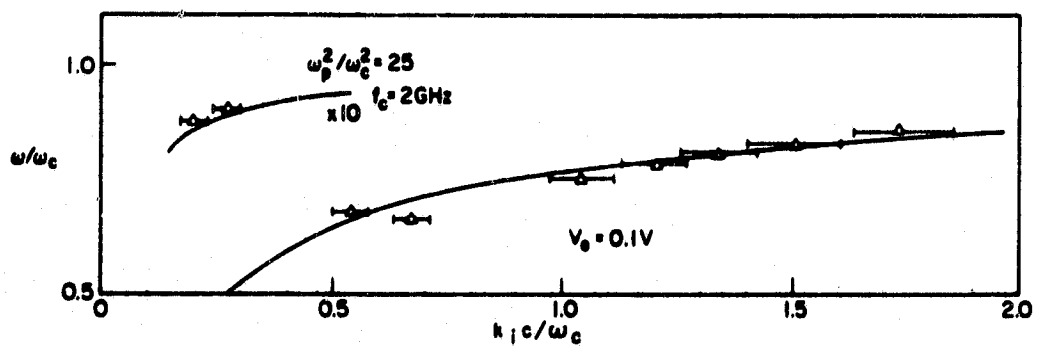

(b) ω/ω_c **vs** $k_i c/\omega_c$

FIG. 5.16. WHISTLER DISPERSION AND DAMPING RATE MEASUREMENTS.

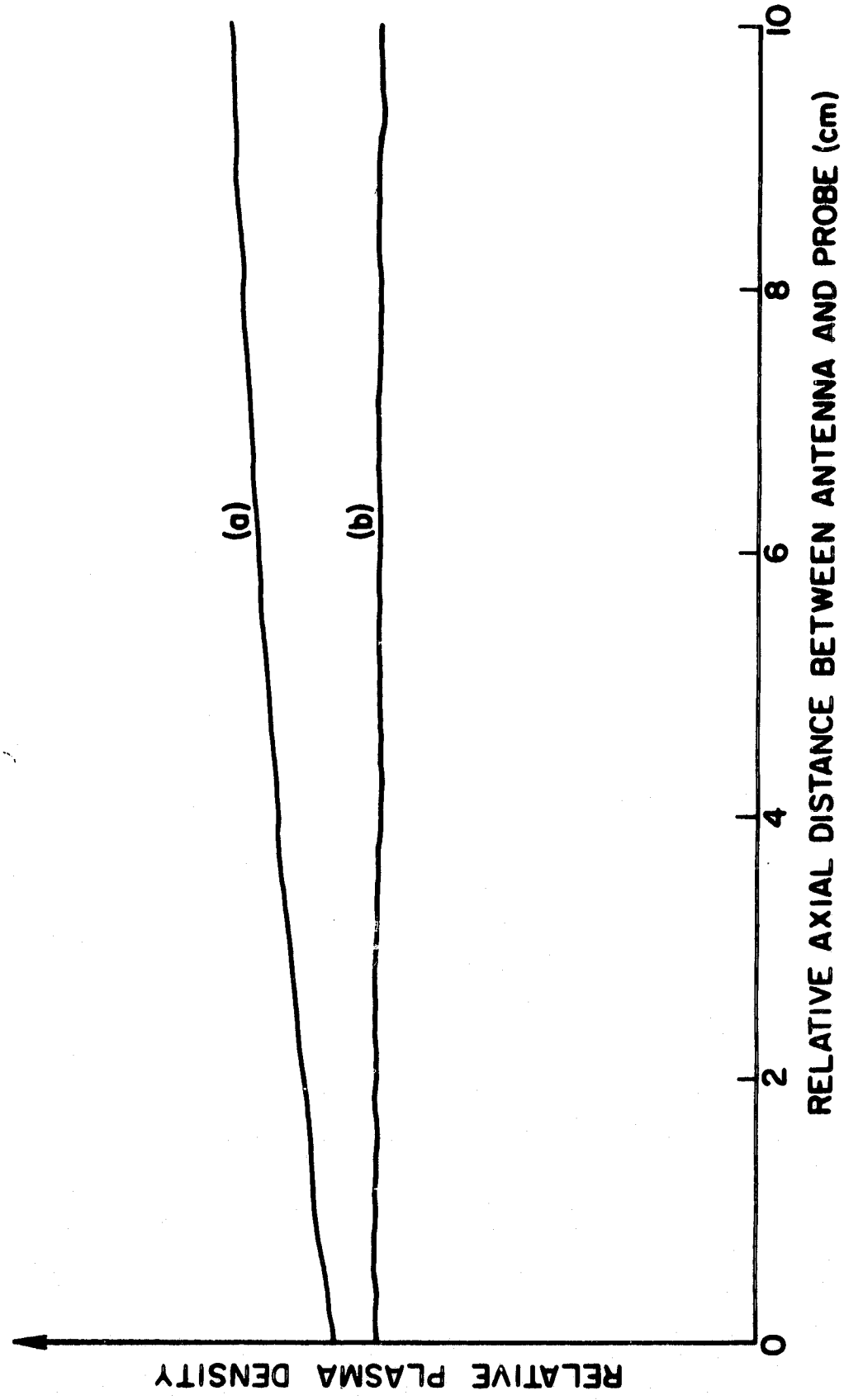

FIG. 5.17. ANTENNA SHADOW EFFECTS. [(a) Probe located at 2 cm from the plasma tube axis;
(b) Probe located at the plasma tube axis].

E. DISCUSSION

1. Limitations of the Measurements

It was found to be possible to obtain experimental dispersion characteristics for comparison with theory only over a limited range of parameters: At low plasma densities and low magnetic fields, the wavelength in the plasma was too long, so that reflections and boundary effects became important. At frequencies too close to the electron cyclotron frequency, the effects of very strong damping prevented us from obtaining meaningful data well above noise level. Thus the highest value of the parameter (ω/ω_c) was limited to about 0.9. The maximum plasma densities that could be used were limited to $8 \times 10^{12}/cm^3$ because it was necessary to wait in the afterglow for the density minimum at the plasma center to disappear before the propagation experiments could be performed on a reasonably homogeneous plasma. The highest cyclotron frequency was limited to about 4 GHz by onset of instability. For (ω/ω_c) less than 0.25, the wavelengths were too long compared to the plasma column cross-section dimension.

2. Sources of Discrepancies

The principal source of experimental error is associated with the determination of plasma density. As mentioned previously, the plasma density was measured using an interferometer to calibrate a Langmuir probe fixed in the plasma. Thus the probe measured the plasma density at the cross-section tranversed by the interferometer signal. However, even though the radial density profile was accounted for when calibrating the probe, it is unlikely that experimental error was less than 25 percent in the density determination.

The measurement of plasma temperature using a Langmuir probe is perhaps more questionable than the density determination. The final value of electron temperature of about 0.1 eV may indicate that the temperature of the background gas was 0.1 eV, and that the final electron temperature was consequently relatively independent of initial plasma parameters. Since the characteristic length of the Langmuir probe was approximately 250 Larmor radii at an electron energy of 0.1 eV and a magnetic field strength of 1000 Gauss, the "temperature" actually measured

might have resulted from a failure of the method. The probe theory of San Martin [78] shows no saturation effects at low temperature, however, even for the case of ion Larmor radius smaller than the probe dimensions. An independent measurement of plasma temperature would be required to fully resolve this question, but it is reassuring that, if the whistler propagation experiment itself is considered as a means of measuring electron temperature, the electron temperature is very close to that obtained by the probe measurement.

It will be noted from the experimental result of Fig. 5.16 that agreement is reasonably good for both wavelength and damping rate when the wavenumbers are not too small. At lower frequencies, corresponding to longer wavelengths, the agreement is not as good, expecially for the damping measurement. This last result is to be expected because of the finite size of the experimental system. It was found experimentally that for wavelengths in the plasma greater than 3.75 cm (= the plasma column radius), finite geometry effects became important, and that the plane wave dispersion relation was no longer valid for wavelength measurements. For damping measurements made at wavelengths longer than 2 cm, the damping measurement deviated from the calculated value.

For $(\omega/\omega_c) < 0.5$, the secondary reflected waves described in Section C of Chapter III are heavily damped due to electron-ion collision effects. No appreciable interference was observed due to these waves during our whistler measurements.

VI. CONCLUSIONS AND SUGGESTIONS FOR FUTURE WORK

A. CONCLUSIONS

The main purposes of this work have been to carry out a comprehensive investigation of the characteristics of whistler propagation and instabilities, and an experimental study of whistler propagation in a laboratory plasma. There are two damping mechanisms, collisional and collisionless, associated with whistler propagation. The collisionless (cyclotron) damping and whistler instabilities are due to wave-particle cyclotron resonance interaction. In such interaction, a significant amount of energy can be exchanged between the particle kinetic energy and the wave electromagnetic energy. For an isotropic charged particle velocity distribution, the wave gives energy to the particles. Thus, cyclotron damping of the wave is accompanied by plasma heating. For an anisotropic particle velocity distribution, the wave may take energy from the particles and exhibit a microinstability. To illustrate the basic features of the propagation, a series of electron velocity distributions have been considered. The dispersion relation has been solved for each case numerically, and where possible analytically.

For a general distribution function, we have derived the dispersion function and discussed the positive and negative frequency parts of the dispersion function in Chapter II. For an isotropic distribution, we have considered in Chapter III both collisional and cyclotron damping of whistlers, with particular emphasis on the region of cyclotron resonance. The relative importance of the two damping mechanisms has been analyzed. The results show that at frequencies far below cyclotron resonance, collisional damping always dominates, whereas close to ω_c cyclotron damping becomes important. Collisional effects are found to reduce the damping below that of cyclotron damping alone at resonance.

For whistlers in bounded magnetoplasma, the paradox raised by Wieder has been resolved from the point of view of double reflection of plane waves. As a by-product, the criterion for the validity of quasistatic approximation has been established for the body waves.

In Chapter IV, the instability character has been studied for a gyrating electron beam interacting with a whistler. We find that the

instability is in general nonconvective. This nonconvective instability can be quenched by collisions in the plasma, or more effectively by parallel velocity spread in the beam.

For an anisotropic plasma, we found that for $T_\perp < T_\parallel$ the cyclotron damping is enhanced, and that for $T_\perp > T_\parallel$ the cyclotron damping is reduced. In addition, for $T_\perp > T_\parallel$ we have found that for wavenumbers and frequencies below certain marginal stability values, instabilities can be excited. The region for this transition has been studied.

In addition to the usual marginal instability conditions, we have studied the conditions for the onset of absolute instability. A general criterion for the onset of absolute instability for an anisotropic energetic electron group with a Maxwellian velocity spread parallel to the magnetic field has been established, including the effect of a cold background plasma. The work suggests that the onset of absolute instability may impose a limitation on cyclotron heating of magnetically confined plasma. The instability criterion has also been applied to parameters pertaining to conditions in the magnetosphere. For example, for the cold plasma in the equatorial plane at about six earth's radii, 1 percent of high energy electrons of 50 keV having a temperature anisotropy of $\alpha = 7$ would be enough to drive the whistler instability nonconvectively unstable.

In the situation where nonconvective instability is excited, the amplitude of an arbitrary distrubance grows indefinitely with time at any point in space until saturation is reached. Nonconvective instability is likely to contribute to the continuous spectrum of VLF emission of the "hiss" type. For situations where the temperature anisotropy for the high energy particle distribution relaxes to a lower value, the whistler instability character would be convective. With a symmetric (nondrifting) anisotropic distribution, there would then be convective growth in both directions along the magnetic field lines. The convective instability suggests itself for amplification of whistlers in long whistler echo trains [6,45]. The constant amplitude sometimes observed, may represent a nonlinear saturation effect. In connection with the instabilities predicted in this research, it should be noted that nonlinear processes must eventually take over. The analysis of the nature of the

instability reported here should provide important initial conditions for further extensions to the nonlinear regime.

In our laboratory experiments, plane wave propagation conditions were approached by working at plasma densities of $\sim 10^{12}/cm^3$, magnetic field strengths of several kilogauss, and at a signal frequency $\gtrsim$ 1 GHz. By obtaining spatial whistler interferograms, plasma boundary effects near the antennas were avoided, as well as antenna near field effects. Whistler dispersion curves and damping rates found from spatial whistler interferograms were in good agreement with theory. Since the experiment was carried out in a low pressure afterglow discharge with low electron temperature (~0.1 eV), the dominant damping mechanism was found to be electron-ion Coulomb collisions rather than cyclotron damping.

B. Suggestions for Future Work

1. Both the cyclotron damping and instability analyses were carried out with the assumption of propagation along the magnetic field. The analysis and numerical calculation should be extended to propagation at an arbitrary angle.
2. Nonlinear whistler interaction studies are needed to determine the whistler amplification saturation level, and to account for unexplained phenomena such as VLF triggered emissions.
3. Further experiments should be carried out to check the warm plasma theory of cyclotron damping, and the instability predictions due to temperature anisotropy in the laboratory.

Appendix A

WHISTLER PROPAGATION IN PLASMA WITH AN ISOTROPIC VELOCITY DISTRIBUTION

For isotropic (spherically symmetric) velocity distributions, the general non-relativistic and collisionless whistler dispersion relation (Eq. (3.1)) reduces to,

$$\omega^2 D(\omega,k) = \omega^2 - k^2c^2 - \omega_p^2\omega \int \frac{f_0 d\underset{\sim}{v}}{(\omega - kv_{\parallel} - \omega_c)} = 0 \ . \qquad (A.1)$$

With exp $i(\omega t - kz)$ variation, for instability we will assume $\omega_i < 0$ and $k_i = 0$. Following Jackson [79] we separate the real and imaginary parts of $\omega^2 D(\omega,k)$. This yields

$$Re(\omega^2 D) = \left(\omega_r^2 - \omega_i^2\right) - k^2c^2 - \omega_p^2 \int \frac{\left(\omega_r^2 - kv_{\parallel}\omega_r - \omega_c\omega_r + \omega_i^2\right) f_0 d\underset{\sim}{v}}{(\omega_r - kv_{\parallel} - \omega_c)^2 + \omega_i^2} \ , \qquad (A.2)$$

$$Im(\omega^2 D) = 2\omega_r\omega_i + \omega_i\omega_p^2 \int \frac{(kv_{\parallel} + \omega_c)\, f_0 d\underset{\sim}{v}}{(\omega_r - kv_{\parallel} - \omega_c)^2 + \omega_i^2} \ . \qquad (A.3)$$

Suppose $D(\omega,k) = 0$ for a pair of such (ω,k). Then both its real and imaginary parts must be zeros. However, the linear combination

$$\frac{\omega_r}{\omega_i} Im(\omega^2 D) - Re(\omega^2 D) = k^2c^2 + \omega_r^2 + \omega_i^2 + \omega_p^2\left(\omega_r^2 + \omega_i^2\right) \int \frac{f_o d\underset{\sim}{v}}{(\omega_r - kv_{\parallel} - \omega_c)^2 + \omega_i^2} \qquad (A.4)$$

can not be zero for finite values of ω_r, ω_i and k real. This proves that the assumption of complex ω and real k can not be a solution of Eq. (A.1), and therefore the system is stable. Note that the additional condition

$$\frac{\partial f_0(v)}{\partial v} < 0 \qquad (A.5)$$

needed to guarantee stability for longitudinal plasma oscillations [79] and cyclotron harmonic waves [80], is not required for whistlers. Thus for whistlers, as long as $f_0(v)$ is isotropic it is stable. There is no limitation to single hump for the distribution. For example, a spherical shell distribution is always stable to whistlers, but not to cyclotron harmonic waves. The above argument can be extended to include relativistic effects, and velocity-independent collisional effects.

Appendix B

GENERAL ONSET CONDITIONS OF NONCONVECTIVE INSTABILITY FOR ANISOTROPIC RESONANCE DISTRIBUTION

For a hot electron group of plasma frequency ω_b, with anisotropic resonance distribution, and a cold plasma of plasma frequency ω_p, the dispersion relation is given by Eq. (4.24). Equation (4.24) can be put into the form of Eq. (4.31)

$$\xi_r^3 Z_r(\xi_r) + g_r \xi_r^2 - h_r = 0 \ , \tag{B.1}$$

where

$$Z_r(\xi_r) = \frac{1}{i - \xi_r}, \quad \xi_r = \frac{\omega - \omega_c}{k v_r} \ , \tag{B.2}$$

$$g_r = \frac{A + \sigma + \omega(\omega_c - \omega)/\omega_h^2}{A - 1}, \quad h_r = \frac{c^2 \left(\omega_c - \omega\right)^3}{\omega \omega_b^2 v_r^2 (A - 1)} \ ,$$

$$A_r = \frac{(\alpha_r - 1)(\omega_c - \omega)}{\omega}, \quad \sigma = \frac{\omega_p^2}{\omega_b^2} \ . \tag{B.3}$$

When the displacement current term can be neglected, g_r reduces to $(A_r + \sigma)/(A_r - 1)$. Following the argument and procedure of Section C3 of Chapter IV, the conditions for onset of nonconvective instability are found numerically to be $g_r = 1.07$ and $h_r = 4.50$. These general results may be used as follows. Since g_r is known, specification of σ yields A_r. If α_r is specified, then substitution in the expression for A_r yields ω. Now h_r is known, so that $\omega_b^2 v_r^2 / \omega_c^2 c^2$ can be determined. Specification of either ω_b^2/ω_c^2 or v_r^2/c^2 gives the other.

REFERENCES

1. L. Landau, "On the Vibrations of the Electronic Plasma," J. Phys. (U.S.S.R.) 10, 25 (1946).

2. H. Derfler, "Landau Waves," A Survey of Phenomena in Ionized Gases (International Atomic Energy Agency, Vienna, 1968), p. 173.

3. F. W. Crawford, "A Review of Cyclotron Harmonic Phenomena in Plasmas," Nucl. Fusion 5, 73 (1965).

4. A. W. Trivelpiece, and R. W. Gould, "Space Charge Waves in Cylindrical Plasma Columns," J. Appl. Phys. 30, 1784 (1959).

5. W. P. Allis, S. J. Buchsbaum and A. Bers, Waves in Anisotropic Plasmas (MIT Press, Cambridge, Mass., 1963).

6. R. A. Helliwell, Whistlers and Related Ionospheric Phenomena (Stanford Univ. Press, Stanford, Calif., 1965).

7. H. Barkhausen, "Whistling Tones from the Earth," Proc. IRE 18, 1155 (1930).

8. R. Bowers and M. C. Steele, "Plasma Effects in Solids," Proc. IEEE 52, 1105 (1964).

9. R. L. Smith, "Properties of the Outer Ionosphere Deduced from Nose Whistlers," J. Geophys. Res., 66, 3709 (1961).

10. D. L. Carpenter, "Whistler Evidence of a 'Knee' in the Magnetospheric Ionization Density Profile," J. Geophys. Res. 68, 1675 (1963).

11. L. R. O. Storey, "An Investigation of Whistling Atmospherics" Phil. Trans. Roy Soc. A (London), 246, 113 (1953).

12. R. A. Helliwell, J. H. Crary, J. H. Pope, and R. L. Smith, "The 'Nose' Whistler--A New High Latitude Phenomenon" J. Geophys Res., 61, 139 (1965).

13. K. G. Budden, Radio Waves in the Ionosphere, (Cambridge Univ. Press, London, 1961).

14. R. H. Gallet, J. M. Richardson, B. Wieder, G. D. Ward, and G. N. Harding, "Microwave Whistler Mode Propagation in a Dense Laboratory Plasma," Phys. Rev. Letters 4, 347 (1960).

15. T. Consoli, and M. Dagai, " Polarisation Rotatoire Magnetique dans les Plasmas--Application à la Mesure de la Densité Electronique," J. Nucl. En. Pt.C. 3, 115(1961).

16. D. W. Mahaffey, "Microwave Propagation through a Plasma in a Magnetic Field," Phys. Rev. 129, 1481 (1963).

17. L. A. Dushin, V. I. Privezentsev, and A. I. Skibendo, "Microwave Plasma Diagnostics Utilizing Longitudinal Propagation of Radio Waves," Kiev Izdatel'stvo An UKSSR, 2 450 (1961).

18. A. N. Dellis and J. M. Weaver, "Whistler-mode Propagation in a Laboratory Plasma," Proc. Phys. Soc. 83, 473 (1964).

19. L. E. Sharp, and C. A. Hooker, "Longitudinal Propagation of a Microwave Beam in a Laboratory Plasma Near the Cyclotron Resonance," Nuclear Fusion 5, 121 (1965).

20. M. P. Bachynski and B. W. Gibbs, "Propagation in Plasma along the Magnetic Field I. Circular Polarization," Phys. Fluids 9, 520 (1966).

21. G. F. Brand and C. A. Hooker, "Interactions of Characteristic Waves in Plasmas," J. Appl. Phys. 38, 3118 (1968).

22. "Study of Electromagnetic Interactions in Plasmas," Contract DA36-039-SC-85317, Final Rept., Electron Tube and Microwave Laboratory, California Institute of Technology, Pasadena, Calif. (November 1961).

23. D. Formato and A. Gilardini, "Propagation Characteristics of Magnetoionic Plasma Columns," J. Res. NBS 66D, 543 (1962).

24. B. Wieder, "Microwave Propagation in an Overdense Bounded Magnetoplasma," Phys. Fluids 7, 964 (1964).

25. P. Hedvall, and L. Sjögren, "The Influence of Collisions on Whistler Propagation," Elect. Letters 1, 54 (1965).

26. T. Pradhan, "Plasma Oscillations in a Steady Magnetic Field: Circularly Polarized Electromagnetic Modes," Phys. Rev. 107, 1222 (1957).

27. V. D. Shafranov, "Propagation of an Electromagnetic Field in a Medium with Spatial Dispersion," Soviet Phys. JETP 6, 545 (1958).

28. J. E. Drummond, "A Microwave Thermometer for Millions of Degrees," Conference on Extremely High Temperatures, Boston, Mass. 1958, (Edited by H. Fischer and L. C. Mansur, John Wiley and Sons, Inc. New York, 1958), p. 97.

29. F. L. Scarf, "Landau Damping and the Attenuation of Whistlers," Phys. Fluids 5, 6 (1962).

30. D. A. Tidman and R. K. Jaggi, "Landau Damping of Transverse Waves in the Exosphere by Fast-Particle Fluxes," J. Geophys. Res., 67, 2215 (1962).

31. P. M. Platzman and S. J. Buchsbaum, "Wave Propagation along a Magnetic Field in a Warm Plasma," Phys. Rev. 128, 1004 (1962).

32. J. E. Willett, "Effects of Electron Random Motion on Microwave Propagation through a Plasma Parallel to a Magnetic Field," J. Appl. Phys. 33, 898 (1962).

33. H. B. Liemohn, and F. L. Scarf, "Dispersion Function for a Plasma with a Cauchy Equilibrium Distribution," Phys. Fluids 6, 388 (1963).

34. H. Motz, "Solutions of the Dispersion Equation and Landau Damping Near the Cyclotron Frequency," Proc. International Colloquium on the Interaction of HF Fields with Plasma in a Static Magnetic Field, Saclay, France, 1964 (Presses Universitaires de France, 1964) p. 26.

35. H. Guthart, "Whistlers in a Thermal Magnetosphere," Stanford Research Institute, Menlo Park, California (Oct 1964).

36. J. Neufeld and H. Wright, "Instabilities in a Plasma-Beam System Immersed in a Magnetic Field," Phys. Rev. 129, 1489 (1963).

37. J. Neufeld and H. Wright, "Interaction of a Plasma with a 'Helical' Electron Beam," Phys. Rev. 135, A1175 (1964).

38. D. B. Chang, "Amplified Whistlers as the Source of Jupiter's Sporadic Decameter Radiation," Astrophys. J. 138, 1231 (1963).

39. T. F. Bell and O. Buneman, "Plasma Instability in the Whistler Mode Caused by a Gyrating Electron Stream," Phys. Rev. 113, A1300 (1964).

40. R. N. Sudan, "Plasma Electromagnetic Instabilities," Phys. Fluids 6, 57 (1963).

41. R. N. Sudan, "Electromagnetic Instabilities in the Nonthermal Relativistic Plasma," Phys. Fluids 8, 153 (1965).

42. R. N. Sudan, "Whistler Instability in Plasmas with Electron Beams," Phys. Rev. 139, A78 (1965).

43. A. Bers, J. K. Hoag, and E. A. Robertson, MIT Research Laboratory of Electronics, QSR 77, 149; 78, 105; 79, 107 (1965).

44. P. C. W. Fung, "Excitation of Backward Doppler-Shifted Cyclotron Radiation in a Magneto-active Plasma by an Electron Stream," Planet. Space Sci. 14, 335 (1966).

45. I. Kimura, "On Observations and Theories of the VLF Emissions," Planet, Space Sci., 15, 1427 (1967).

46. H. B. Liemohn, "The Cyclotron Resonance Interaction in the Magnetosphere," Proc. NATO Advanced Study Institute on Plasma Waves in Space and in the Laboratory, Røros, Norway. April 1968 (in press).

47. J. E. Scharer and A. W. Trivelpiece, "Cyclotron Wave Instabilities in a Plasma," Phys. Fluids 10, 591 (1967).

48. J. E. Scharer, "Plasma Electromagnetic Instabilities in a Magnetic Mirror Configuration," Phys. Fluids 10, 652 (1967).

49. A. C. Das, "Dispersion of the Whistler Mode for a Velocity Distribution with a Loss Cone," J. Plasma Phys. 1, 29 (1967).

50. F. W. Crawford, J. C. Lee, and J. A. Tataronis, "Some Studies of Whistler Instability, Proc. NATO Advanced Study Institute on Plasma Waves in Space and in the Laboratory, Røros, Norway, April 1968 (in press).

51. A. Iiyoshi, H. Yamato, and S. Yoshikawa, "Limitation on Ion Cyclotron Heating in the Local Mirrors of the C Stellarator," Phys. Fluids 10, 749 (1967).

52. H. Derfler, "Electrostatic Relaxation Waves in an Isotropic Lorentz Gas," Phys. Fluids 10, 1936 (1967).

53. V. V. Zheleznyaskov, "The Instability of a Magnetoactive Plasma Relative to High Frequency Electromagnetic Excitation," English Transl: News of Higher Educational Inst., Ministry of Higher Education, USSR. Radio Physics Series 3, No. 139 (1961)

54. E. G. Harris, "Plasma Instabilities Associated with Anisotropic Velocity Distributions," J. Nucl. Energy, Pt. C, 2, 138 (1961).

55. N. G. Van Kampen, "The Dispersion Equation for Plasma Waves," Physica 23, 641 (1957).

56. H. Derfler, Electron Device Research Laboratory QSR No. 18, Stanford Electronics Laboratories, Stanford University, Stanford, Calif., p. 17, 1961 (unpublished).

57. H. Derfler, "Theory of RF Probe Measurements in a Fully Ionized Plasma," Proc Fifth International Conference on Ionization Phenomena in Gases, Munich 1961 (North-Holland Publishing Co., Amsterdam, 1962) 2, p. 1432.

58. V. Ferraro, "General Theory of Plasma," Nuovo Cimento, Suppl. No. 1, 13, (1959).

59. D. J. Rose, and M. Clark, Plasmas and Controlled Fusion (MIT Press, Cambridge, Mass., 1961)

60. M. A. Heald, and C. B. Wharton, Plasma Diagnostics with Microwaves (John Wiley and Sons, Inc., New York, 1965).

61. B. D. Fried and S. D. Conte, The Plasma Dispersion Function (Academic Press, New York, 1961).

62. P. C. Clemmow and P. F. Mullaly, "The Dependence of Refractive Index in the Magneto-Ionic Theory on the Direction of the Wave Normal," The Physics of the Ionosphere (Physical Society, London 1955), p. 340

63. W. C. Hahn, "Small Signal Theory of Velocity-Modulated Electron Beams," General Electric Rev. 42, 258 (1939).

64. J. A. Stratton, Electromagnetic Theory (McGraw-Hill Book Company, New York, 1941).

65. L. D. Smullin, and P. Chorney, "Propagation in Ion-Loaded Wave-Guides," Proc Symposium on Electronic Waveguides (Brooklyn Polytechnic Press, Brooklyn, N.Y., 1958), p. 229.

66. J. E. Scharer, and A. W. Trivelpiece, "Quasistatic Analysis of Waves in a Plasma-Filled Waveguide," J. Appl. Phys. 36, 318 (1965).

67. V. Bevc, "Power Flow in Plasma-Filled Waveguides," J. Appl. Phys. 37, 3128 (1966).

68. V. Bevc, "Dynamic Potentials in Gyrotropic Plasmas," Proc. Eighth International Conference on Phenomena in Ionized Gases, Vienna, Austria, 1967 (International Atomic Energy Agency, Vienna, 1967) p. 333.

69. O. Penrose, "Electrostatic Instabilities of a Uniform Non-Maxwellian Plasma," Phys. Fluids 3, 258 (1960).

70. R. J. Briggs, Electron-Stream Interaction with Plasmas (M.I.T. Press, Cambridge, Mass., 1964).

71. P. A. Sturrock, "Kinematics of Growing Waves," Phys. Rev. 112, 1488 (1958).

72. H. Derfler, "Growing Wave and Instability Criteria for Hot Plasma," Phys. Letters 24A, 763 (1967).

73. H. Derfler, "The Frequency Cusp, a New Means for Discriminating Between Growing Waves and Instabilities in Hot Plasma," Proc. Ninth International Conference on Phenomena in Ionized Gases, Bucharest, 1969 (to be published).

74. T. H. Stix, The Theory of Plasma Waves (McGraw-Hill Book Company, New York, 1962), Chap.8.

75. J. Y. Wada and R. C. Knechtli, "Generation and Application of Highly Ionized Quiescent Cesium Plasma in Steady State," Proc. IRE 49, 1926 (1961).

76. J. C. Hosea, "Probe Measurement in a Pulsed Plasma--Experimental Verification of the BBM Analysis for Ion Saturation Current," J. Appl. Phys. 37, 2695 (1966).

77. J. R. L. San Martin, "The Theory of Electrostatic Probes in Strong Magnetic Fields," Tech. Rept. AFFDL-TR-67-190, Air Force Flight Dynamics Lab., Wright-Patterson Air Force Base, Ohio (1968).

78. L. S. Frost and A. V. Phelps, "Momentum-Transfer Cross Sections for Slow Electrons in He, Ar, Kr, and Xe from Transport Coefficients," Phys. Rev. 136A, 1538 (1964).

79. J. D. Jackson, "Longitudinal Plasma Oscillations," J. Nucl. Energy, Pt.C, 1, 171 (1960).

80. J. A. Tataronis, "Cyclotron Harmonic Wave Propagation and Instabilities," Institute for Plasma Research, Rept. No. 205, Stanford University, Stanford, Calif. (December 1967).